Temperatures and Heat Production in the Slave Craton Lower Crust: Evidence from Xenoliths in the Diavik A-154 Kimberlite

by

Benjamin Hess Gruber

A thesis submitted in partial fulfillment of the requirements for the degree of

Master of Science

Department of Earth and Atmospheric Sciences
University of Alberta

Abstract

Lower crustal heat production is poorly constrained due to the relative inaccessibility of lower crustal samples and their inherent complexity. To obtain the requisite information, the current project conducts spatially resolved geochemical analyses on minerals in 15 lower crustal xenoliths erupted via the Diavik A-154 kimberlite of the Northwest Territories, Canada. The aims are to: 1) conduct geothermometric measurements on lower crustal minerals, 2) construct a heat-producing element budget of the lower crust of the Slave craton, and 3) test the validity of these measurements in a parameter space relevant to geodynamic modeling and diamond exploration.

The Diavik lower crustal xenolith suite comprises two main lithologies, mafic granulite (garnet-plagioclase-clinopyroxene ± orthopyroxene) and metasedimentary granulite (garnet-plagioclase-orthopyroxene ± quartz ± K-feldspar ± kyanite), which are present in proportions of approximately 80:20, respectively. Application of mineral-pair, iron-magnesium exchange geothermometers (garnet-biotite, garnet-amphibole, and garnet-clinopyroxene) to these xenoliths indicates that the lower crust was at a maximum temperature of roughly 500 °C at the time of kimberlite eruption (~ 55 Ma). The actual temperature of the lower crust is likely lower than 500 °C as the geothermometers probably record the closure temperature of diffusional Fe^{2+}-Mg exchange between touching mineral pairs rather than the ambient temperature of the rocks prior to their entrainment in the kimberlite magma.

Heat-producing element (HPE) concentration measurements show that the lower crustal heat production of the Slave craton is likely 0.14 ± 0.02 $\mu W/m^3$, which is lower than most values in the literature but broadly comparable to some geophysical estimates. This estimate is the result of (20:80) bimodal mixing of idealized lower crustal endmembers: a metasedimentary lower crust (0.37 ± 0.06 $\mu W/m^3$) and a mafic lower crust (0.08 ± 0.01 $\mu W/m^3$). These endmembers were

calculated via a reconstructed bulk rock calculation utilizing trace element concentrations of constituent lower crustal minerals and idealized lithologies from the lower crustal xenoliths.

Using these heat production estimates and other crustal parameters such as continental heat flux, mantle heat flux, crustal thickness, and crustal thermal conductivity, I modeled a Moho temperature for the Slave craton of 425 °C, which is consistent with maximum lower crustal temperature estimate given by geothermometry. Adjusting the lower crustal heat production in the geotherm modeling program FITPLOT changes the temperature of the Moho in a similar fashion to the calculated models; however, the diamond propensity of the mantle lithosphere (partially a function of Moho temperature and heat production) does not appear to be strongly affected by a changing Moho temperature and is more strongly controlled by the conditions of the mantle P-T array.

Acknowledgements

I would like to acknowledge my supervisors Thomas Chacko and Graham Pearson for being the inspiration of this project and the DERTS program for giving me the opportunity to study at the University of Alberta. Coming out of my undergraduate, not many people were willing to give me a chance, I'm forever grateful for the opportunity they gave me. Another thank you to Claire Currie for being on my committee and giving me constructive feedback on the manuscript and to Anetta Banas for helping get DERTS off the ground during my first years here and for the getting me an internship at the Alberta Geological Survey. I would also like to thank Yan Luo and Andrew Locock for their assistance in getting the high-quality data needed to make this project possible. Thank you to Andrew Menzies of the Universidad Católica del Norte CISEM for providing the QEMSCAN ® data that was essential to the project. This project also could not have happened without the generous sample donation from the Diavik Mine and all of those who worked on these samples before me. I hope I didn't leave too many holes…

I could not have done this project without the countless friends and labmates I have made during this project and in all of my side ventures. In particular I would like to thank Carson Glodek, Natasha Barrett, Matthew Hardman, Margo Regier, Pamela Twerdy, Elaine Lord, Forrest Wells, Ryan James, Nicole Meyer, Hanna Brooks, and Tim McIntyre for all of their assistance with the science and for their help in distracting me when the going got tough, I could not have done this without you guys! Lastly, I would like to thank my parents and family for instilling a love for nature and geology in me at a young age and for giving me support during this adventure to Canada.

Table of Contents

List of Tables

List of Figures

List of Symbols

%	Percent
±	Uncertainty
°C	degrees Celsius
A	Heat Production
DI	Differentiation Index
EDS	Energy Dispersive Spectrometry
EPMA	Electron Probe Micro Analyzer
Fe^{2+}-Mg	Iron and Magnesium Exchange
Ga	Billion Years Ago
HP	Heat Production
HPE(s)	Heat Producing Element(s)
kbar	kilobar
kg/m^3	kilograms per meter cubed (density)
km	kilometer
LA-ICP-MS	Laser Ablation Intercoupled Plasm Mass Spectrometry
Ma	Million Years Ago
Mg#	Magnesium Number
µm	Micrometer
Moho	Mohorovičić discontinuity
$\mu W/m^3$	Microwatts per meter cubed
ppm	Parts Per Million

REE	Rare Earth Element
SCLM	Subcontinental Lithospheric Mantle
SEM	Scanning Electron Microscope
TIMS	Thermal Ionization Mass Spectrometer
U-Pb	Uranium Lead Dating
Vol. %	Volume Percent
WDS	Wavelength Dispersive Spectrometry
Wt %	Weight Percent

Chapter 1: Introduction

The thermochemical conditions of Earth's lower continental crust are poorly understood partially due to the relative inaccessibility of sample materials compounded by additional factors that complicate the interpretation of an already limited sample set. An understanding of the lower crustal chemical composition and thermal parameters is crucial to unraveling the details of continent formation and stabilization, high-grade metamorphism, and the role of crustal heat production in defining lithospheric geotherms. This study attempts to understand the thermal character of the cratonic lower crust through applying new geochemical techniques on granulite-grade crustal xenoliths hosted in kimberlite. The aims are to:

1) Estimate an ambient temperature of the lower crust at the time of kimberlite magmatism through the application of iron-magnesium (Fe^{2+}-Mg) exchange geothermometry on touching minerals pairs in lower-crustal xenoliths.
2) Estimate heat production values for representative lower crustal rocks through a combination of trace-element analysis of constituent minerals and reconstructed whole-rock compositions.
3) Calculate the effects of these new elemental concentration measurements on a variety of crustal parameters, including: the evolution of Mohorovičić discontinuity (Moho) temperatures over time, the historic heat production of a craton, and the effects of varying crustal thermal parameters on lithospheric geotherms.

Radiogenic heat production and the concentrations of heat producing elements were first investigated indirectly in some of the early assessments of the composition of the continental crust. In particular, Weaver and Tarney (1984), Taylor and McLennan (1985) and Shaw (1986) reported estimates of bulk continental crust composition and radiogenic heat production. Rudnick and

Fountain (1995) later assessed the effects of a stratified, three-layer crust on heat production. The recent work of Hasterok and Chapman (2011) stresses the importance of having well-constrained crustal heat production models in the propagation of geotherms into the mantle lithosphere. The review by Jaupart et al. (2016) emphasizes the significance of identifying compositional characteristics of individual locales when attempting to constrain the measured continental heat flow. Other studies of heat production and heat flow in the lower crust include those of Kramers et al. (2001), Gao and Rudnick (2003), and Hacker et al. (2011); they each provide different estimates of lower crustal heat production, highlighting the likely inhomogeneity of heat production worldwide and its dependence on tectonic setting.

The present study builds on the previous work and aims to provide accurate heat production data and ambient temperature estimates for the lower crust beneath the A-154 kimberlite of northwestern Canada. The study of crustal xenoliths at this locality benefits from the associated mantle xenolith suite available, which permits the examination of the potential effect of varying crustal heat production on mantle geotherm parameters.

To accomplish the aims of this project, spatially resolved, in-situ geochemical analyses were performed on granulite xenoliths hosted in the A-154 kimberlite pipe of the Diavik mine, in the Slave craton, Northwest Territories, Canada. This kimberlite is part of the greater Lac de Gras kimberlite field, which hosts diamond deposits and various mantle and crustal xenoliths. Davis (1997), Davis et al. (2003), Krauss et al. (2007), Aulbach et al. 2007, and Förster et al. (2017) previously studied lower crustal xenoliths from this location in the context of their geochronology, geothermobarometry, and tectonic implications; the present study takes a thermochemical approach to answering questions about the evolution of the crust and lithospheric mantle. Using updated geochemical analyses of lower crustal samples, this study calculates the crustal heat flux over time and the modeled temperature of the Moho, and compares these model estimates with direct geothermometric estimates of ambient lower crustal temperature. Through improved and expanded geochemical data on this lower crustal xenolith suite and creating realistic crustal models from these data, this study adds to the earlier body of work on the Lac de Gras lower crust and makes comparisons to granulite terranes, granulite xenoliths, and the lower crust worldwide.

Chapter 2: Background and Geological Setting

2.1 Sampling the Lower Crust

The samples studied in this project are granulite-facies xenoliths erupted from the A-154 kimberlite pipe of the Diavik mine, located at the Lac de Gras kimberlite field in the Northwest Territories, Canada. The Lac de Gras field is situated in the central portion of the Slave craton, an Archean craton with a geologic history extending back to > 4.0 Ga (see Bleeker and Hall, 2007 for review). The craton is underlain by a subcontinental lithospheric mantle (SCLM) of late Archean age (Heaman and Pearson, 2010), which potentially formed as a result of melting related to plume activity (Aulbach et al., 2007) and/or subduction/imbrication of oceanic lithosphere (Helmstaedt, 2009; Heaman and Pearson, 2010). The present study utilizes a representative set of lower crustal xenoliths from the A-154 kimberlite originally described by Krauss et al. (2007). This kimberlite hosts a set of xenoliths with a diverse mineralogy representing the various lithologies of the lower crust. The A-154 pipe was emplaced at 55 Ma (Creaser et al., 2003; Heaman et al., 2003; Sarkar et al., 2015) and contains abundant mantle and crustal xenoliths.

As the lower continental crust in most locales exists at depths typically inaccessible for direct sampling (> 25 km depth in the Slave craton; Krauss et al., 2007), other methods must be applied to obtain representative samples of deep crust material. Direct investigation of lower crustal samples, as opposed to remote sensing by geophysical methods (e.g. Shankland and Ander, 1983), can be performed through two different methods: 1) studies on exposed granulite terranes that have been tectonically uplifted to the surface (see Rudnick and Fountain, 1995 for review) and 2) studies on lower crustal fragments that are entrained as xenoliths in rising magmas such as kimberlites and alkali basalts (see Rudnick, 1992 for review).

Exhumed granulite terranes are beneficial in that they allow for collection of large samples that reduce sampling errors induced by modal variability. These outcropping rocks also allow the documentation of field relationships. However, as noted by Rudnick and Fountain (1995), the fact that tectonically-exposed granulite terranes are no longer present in the lower crust along with their various methods of un-roofing raises the question of whether uplifted terranes are completely representative of the continental lower crust. Rudnick and Fountain (1995) argue that exposed granulite terranes may incorporate different compositional biases compared to similar studies involving xenoliths as terranes that have undergone isothermal decompression are generally more felsic than those that underwent isobaric cooling. These questions cast doubt on whether exhumed granulite terrane sections are truly representative of the lower crust.

Xenoliths entrained in deep-seated magmas can, in principle, also provide samples of the lower crust but these too have limitations. Xenoliths carried by alkali basalts may potentially represent the crystallization products of earlier episodes of host basaltic magmatism and thus may not be truly representative of the ambient lower crust at the time of basaltic eruption (Rudnick and Fountain, 1995). This is less of a problem with kimberlite-hosted xenoliths, as entrained kimberlite crystallized at depth would not resemble granulite-facies mafic and intermediate rocks. Part of the greater problem is that due to their limited size and fragmental nature, xenoliths lack the geological context present in granulite terranes. There is also a geologic setting limitation to the global dataset as xenoliths are found on every continent, though kimberlite-hosted granulite xenolith suites are mostly from Archean cratons (Rudnick, 1992). As kimberlites are carriers of mixed mantle and crustal material, their xenoliths can provide useful information regarding the deep crust and underlying lithospheric mantle. However, as can be seen in petrographic sections, kimberlite magma more commonly interacts with and contaminates its xenoliths than do alkali basalts (Rudnick, 1992), probably due to the low viscosity of silica-poor, carbonate-rich melts. Barth et al. (2001) showed that interaction with kimberlite magma can enrich xenoliths in large ion lithophile (LILE) and light rare earth elements (LREE). As such, any study of kimberlite-hosted xenoliths would necessitate an evaluation of the degree of kimberlite contamination.

Lower crustal xenoliths from the Diavik mine and the greater Lac de Gras area have been dated through geochronological methods. Davis (1997) reported some of the first U-Pb ages for zircon and rutile hosted in mafic granulite-facies xenoliths from Lac de Gras; generally, they found two populations of ages, one around 1200 Ma and another around 2300 Ma. These ages can be roughly correlated to igneous events possibly related to early mafic underplating of the Slave Craton (Davis, 1997). Davis et al. (2003) were able to expand on these ages by showing through TIMS U-Pb dating that the Slave Craton lower crust and lithosphere had almost completely formed by 2.9 Ga, with some nuclei of it being present at 3.2 Ga. Through analyzing growth zones within these zircons, Davis et al. (2003) also found that after lower crust formation that there were at least four more periods of zircon growth probably partially related to plutonism and high-grade metamorphism between 2.6 Ga and 2.5 Ga.

Most studies of both granulite terranes and xenolith samples suites suggest the lowermost crust is predominately mafic, though some high-grade sedimentary rocks and felsic igneous rocks are also present (Rudnick and Fountain, 1995; Gao and Rudnick, 2003; Condie et al., 1999). Other studies, such as Hacker et al. (2011), argue for a more felsic/intermediate lower crust, whereby the re-lamination of felsic materials to the base of a continent during subduction greatly increases the bulk heat production of the lower crust. The study of Rudnick and Taylor (1987) is one of the first to propose the origin of the lower crust on a chemical basis, suggesting essentially three different possibilities: 1) lower crustal xenoliths are restites left over from previous melting events, 2) lower crustal xenoliths are the result of mafic underplating at the Moho (advocated at Lac de Gras by Davis, 1997), and 3) lower crustal xenoliths originally formed as supracrustal units that were then tectonically brought to depth or buried. Lower crustal xenoliths are generally at granulite-grade and dominated by anhydrous phases such as garnet, plagioclase, and pyroxenes (Rudnick and Fountain, 1995), although some xenoliths can host up to 5% hydrous phases such as amphibole and biotite (Rudnick and Taylor, 1987).

2.2 Ambient Temperatures

Metamorphic temperatures are commonly calculated through the application of Fe^{2+}-Mg exchange geothermometers to rocks with coexisting ferromagnesian minerals. These mineral phases (e.g. biotite, clinopyroxene, orthopyroxene, amphibole, garnet) undergo Fe^{2+}-Mg exchange as the metamorphic grade is increased (prograde) or decreased (retrograde). One of the most widely used of these thermometers is the garnet-biotite geothermometer (e.g., Ferry and Spear, 1978). Other examples of this type of geothermometer applicable to granulites are the garnet-clinopyroxene, and garnet-amphibole geothermometers (e.g., Krogh Ravna 2000a, 2000b)

Normally, the goal in metamorphic petrology is to retrieve the peak (or maximum) metamorphic temperature experienced by a sample (e.g., Frost and Chacko, 1989). In contrast, the goal in the present study is to estimate the temperature experienced by the xenolith samples immediately prior to their entrainment in the kimberlite magma. In other words, the goal is to determine the ambient temperature of the Slave craton lower crust at the time of kimberlite eruption. It should be noted that peak metamorphism of the Slave lower crust occurred at ca. 2500 Ma (Davis et al., 2003; Krauss et al., 2007), long before the time of kimberlite magmatism (ca. 55 Ma; Creaser et al., 2003; Heaman et al., 2003; Sarkar et al., 2015). By 55 Ma, the Slave lower crust had cooled to a temperature hundreds of degrees below its peak metamorphic temperatures.

The relationship between mineral grains that maximizes the potential for retrograde Fe^{2+}-Mg exchange between grains and in turn the accurate recording of ambient lower crustal temperatures is the use of rim compositions of touching mineral grains in the thermometric calculations. In the best-case scenario, the resulting temperature would be the actual temperature of the lower crust at the time of kimberlite magmatism. Alternatively, if the blocking temperature of Fe^{2+}-Mg exchange in the minerals used for temperature calculation is higher than the ambient temperature then the Fe^{2+}-Mg exchange geothermometer would provide a *maximum* estimate of the ambient lower crust temperature. In either case, Fe^{2+}-Mg exchange geothermometry provides a completely independent lower crustal temperature estimate that can be compared to those derived from surface heat flow calculations. Koreshkova et al. (2011) indirectly employed a similar process on xenoliths from the Siberian craton in which calculated garnet core temperatures are generally several hundred degrees higher than rim temperatures, likely due to retrograde re-equilibration.

2.3 Heat Production

Surface heat flow measurements have commonly been used as an argument as to why the crust must be stratified with respect to concentrations of heat producing elements. If the surficial concentrations of heat producing elements (HPEs; K, U, Th) were homogenous throughout the crust, the surface heat flow would be far greater than is measured today and no mantle heat flux component to heat flow would be required (Rudnick and Fountain, 1995). Despite the decrease in HPE concentrations with depth, crustal heat production is still responsible for roughly 50 to 85 %

of the measured surface heat flow in cratonic regions (Rudnick and Fountain, 1995). Different heat production models for the crust have a strong impact on its thermal architecture. Owing to its high metamorphic grade and predominately mafic character, the lower crust tends to be depleted in incompatible elements, especially in the lithophile HPEs (U and Th) and other lithophile incompatible elements (Rb, Cs), relative to mid- and upper crustal rocks (Heier, 1973). The mechanism for the depletion of these elements in the granulite facies is contentious but is thought to be due either to the extraction of partial melts or to the percolation of fluids with low water activity through the rock units during high-grade metamorphism (Harlov, 2012). Alternatively, the lower crust may be lower in HPEs because it is dominantly comprise mafic rocks, which intrinsically have lower concentrations of these elements. Whatever the mechanism, the deep crust is expected to have a lower heat-producing capacity than the upper crust unless it has been refertilized with added felsic material (e.g., Hacker et al., 2011).

Having a well-constrained lower crustal heat production model is valuable as it allows for conclusions to be made about the overall thermal architecture of both modern and ancient crust. Heat production estimates combined with estimates of crustal thickness, mantle heat flux, and surface heat flux can be utilized to calculate Moho temperatures (Kramers et al., 2001). The effects of varying crustal stratification ratios and total crustal thickness on Moho temperatures and heat flux can also be explored through these methods. When used in conjunction with radiogenic decay rates, the heat flux through geological time and Moho temperatures can be calculated assuming a steady-state model.

Because of its lower HPE concentrations, the lower crust has either been ignored or viewed as being less important than other variables (such as mantle heat flow or lithospheric depth) for the determination of mantle geotherms for the purpose of diamond exploration. Having a well-constrained heat production value for a given locale is also important in having confidence in propagating conductive geotherms into the mantle as crustal heat production is a primary variable in understanding the temperature at the crust-mantle interface (Moho) and in turn a minimum potential temperature for the mantle assuming a standard conductive geotherm. Hasterok and Chapman (2011) refined the reference geotherms of Chapman and Pollack (1977) mainly through the way in which they include heat production variables. Reference geotherms such as these use constant heat production variables for every locale, making implementation easy but commonly also resulting in an oversimplification as they do not reflect site-specific anomalies. Through the use of measurements on an uplifted granulite terrane (as opposed to xenoliths), Hasterok and Chapman (2011) report a lower crust heat production value of 0.4 $\mu W/m^3$. As the reference geotherms of Hasterok and Chapman (2011) allow for simple comparative evaluation of geotherms based on surface heat flow, propagated uncertainties in this heat production value could cause pervasive oversimplifications of lithospheric thermal architecture. Other approaches such as the FITPLOT program (Mather et al., 2011) place more emphasis on the fit of mantle xenolith thermobarometric data to model geotherms. Finally, numerous other studies have calculated their own value of lower crustal heat production through various methods and these are summarized in Table 1.

The present study calculates a range of lower crustal heat production values based on high-quality measurements of K, Th, and U in lower crustal xenoliths erupted by kimberlite and compares this range to the estimates in Table 1. These heat production values are then applied to various crustal thermal models and lithospheric geotherms of the Slave craton crust and mantle.

Table 1. Previous Estimates of Lower Crustal Heat Production

Study	*K2O (wt %)*	*Th (ppm)*	*U (ppm)*	*Heat Production (μW/m^3)*	*Sample*
Hasterok and Chapman (2011)	N/A	N/A	N/A	0.40	Terrane
Pollack and Chapman (1977)	N/A	N/A	N/A	0.25	Terrane
Rudnick and Fountain (1995)	0.6	1.2	0.2	0.18	Terrane
Weaver and Tamey (1984)	1.0	0.42	0.05	0.16	Terrane
Hacker et al. (2011)	1.5	5.6	0.7	0.70	Model
Shaw et al. (1986)	1.6	7.7	1.1	1.17*	Terrane
Taylor and McLennan (1995)	0.34	1.06	0.28	0.19	Model
Dupuy et al. (1979)	1.42	5.8	0.6	0.83*	Xenolith
Rudnick and Taylor (1987)	0.45	0.5	0.2	0.15*	Xenolith
Rudnick and Presper (1989)	0.79	1.6	0.4	0.40	Xenolith
Gao and Rudnick (2003)	0.61	1.2	0.2	0.19	Model
Huang et al. (2013)	-	-	-	0.17	Model
Average	**1.20 ± 0.74**	**2.79 ± 2.77**	**0.42 ± 0.33**	**0.40 ± 0.33**	**-**

Compilation updated from Rudnick (1992). Note that heat production calculation methods vary from study to study and oftentimes rock density is unreported. If not directly provided, heat production is calculated (*) using equation 2 with a density of 3200 kg/m^3 (Gao et al. 2003). Uncertainties in average heat production values are reported at the 1σ level.

Chapter 3: Methods

The present study utilizes Scanning Electron Microscopy (SEM) and Electron Probe Microanalysis (EPMA) to obtain mineral modes on selected lower crustal xenoliths from the Diavik A-154 pipe. Laser ablation inductively-coupled plasma mass spectrometery (LA-ICP-MS) was used for trace-element analyses of the constituent minerals. Along with this, 11 of the 15 selected lower crustal xenoliths were large enough to do powdered whole-rock geochemistry, which was accomplished at the Peter Hooper GeoAnalytical Lab at Washington State University (Johnson et al. 1999). All other analyses were performed on standard polished thin sections from fifteen (15) different xenoliths that were selected on a basis of being relatively free from secondary alteration, having mineral grains large enough to accommodate analyses, having the mineral relations suitable for thermometric measurements, and being representative of the overall xenolith set available (n=46). Mineral modes were determined for several complex xenoliths (n= 5) using energy dispersive X-ray mapping (EDS) on the SEM using QEMSCAN® software (Gottleib et al. 2000) at the Universidad Católica del Norte CISEM. In all other cases this was done with wavelength dispersive (WDS) X-ray mapping on the EPMA for the purpose of measuring the abundance of trace phases. Major phases were collected via manual point counting or with QEMSCAN® software (Gottleib et al. 2000) while trace phases were measured with WDS maps utilized in conjunction with the image processing software ImageJ.

3.1 Thermometry

The thermometric estimates were obtained through determining the major-element compositions of ferromagnesian minerals with the CAMECA SX-100 and JEOL JXA-8900R EPMA instruments at the University of Alberta. The same standards and data reduction procedures were maintained between instruments for analytical consistency. Ferromagnesian minerals (biotite/amphibole/clinopyroxene) included in, or in contact with, garnet were first identified in thin section and then later confirmed through EDS on the EPMA. To perform these analyses, representative analytical spots in biotite, amphibole or clinopyroxene and traverses across the immediately adjacent garnet were performed to identify regions of retrograde chemical zonation called the "retrograde diffusion halo" (see Loomis, 1983 for review). These analyses were made on carbon coated polished thin sections using Wavelength Dispersive Spectrometry (WDS). The experimental conditions for the WDS analyses involved a 20 kV accelerating voltage, a 15 nA beam current, and a beam diameter of 5 μm for biotite and amphibole and a fully focused beam (~ 1 μm) for the clinopyroxene and garnet. The elements Si, Ti, Al, Cr, Fe, Mn, Mg, Ca, and Na were analyzed for garnet and clinopyroxene. The same elements were analyzed in biotite and amphibole with the addition of K, F, and Cl. A combination of natural and synthetic mineral standards were used to convert measured X-ray counts to elemental concentrations. A full description of spectrometer assignments, standards, and probe settings can be found in Appendix B1.

Detailed analytical traverses were conducted across the Fe^{2+}-Mg exchange mineral pairs of interest (garnet-biotite, garnet-amphibole and garnet-clinopyroxene) to obtain mineral compositions reflecting the greatest amount of down-temperature Fe^{2+}-Mg exchange between the minerals. In all cases, garnet acts as host to the other exchange mineral, the latter occurring either as small inclusions within garnet, or as small grains touching the rims of large garnet grains. Given that garnet was of larger grain size than the additional exchanging mineral in all cases, analyses were obtained at a ~ 6 μm spacing from the garnet rim immediately adjacent to touching grains of biotite, amphibole or clinopyroxene to ~ 50 μm into the garnet core. In general, the Mg-number (molar Mg/[Mg+Fe]) of the garnet decreased toward the garnet rim and the analysis with the lowest Mg number (i.e., the most low temperature-re-equilibrated garnet composition) was used in the temperature calculations. Systematic core-to-rim compositional variations were not observed in the analyzed grains of biotite, amphibole or clinopyroxene and therefore an average composition, derived from multiple analyses of each of those grains, was used in the temperature calculations.

3.2 Modal Abundances

Modal abundances on the selected thin sections were performed through two different methods, the first being analysis with QEMSCAN® software (Gottleib et al. 2000) and the other through point counting in conjunction with WDS mapping of trace elements with the CAMECA SX-100 EPMA. Samples analyzed with QEMSCAN® were also subjected to point counting and element mapping to check for large-scale deviations between these two methods. Point counting for the major minerals was done at a coarse count (350 to 1000 points) dependent on the size of the minerals and the complexity of the thin section. WDS mapping for the elements Ce, P, Ca, Zr, and Ti was found to be more reliable for abundance estimates of trace phases monazite, apatite, zircon, and rutile. The modes of the phases were extracted from the X-ray maps using the image processing software ImageJ. Point counts and WDS mapping results were then combined and normalized to 100 % to create an idealized representation of the thin section for HPE reservoirs. Phases such as ilmenite, sulfides, quartz, kyanite, and magnetite are typically not included in the total calculation as they are generally in low abundance and were not found to host high HPE concentrations (Section 4.2).

Both point-counting and QEMSCAN® proved to be effective on these thin sections, especially for calculating the abundances of major minerals (e.g., garnet, plagioclase, clinopyroxene, and orthopyroxene) and a blanket absolute uncertainty for these values can reasonably be set at ± 5 vol.% of the xenolith. Greater discrepancy between these two methods occurs with the trace phases as the QEMSCAN® software is fully automated whereas the WDS mapping was done manually. For example, several thin sections (DDM-20, DDM-303, 1554) contained monazite that had extensive sulfate substitution for phosphate and, as such, was not recognized by the QEMSCAN® software as monazite. WDS mapping, on the other hand, was able to positively confirm the presence of monazite (high Ce and PO_4) as potential monazite grains identified in the mapping could be assessed on a grain by grain basis. With this, trace mineral modal accuracy is calculated to be roughly ± 0.1 (vol.%) of the xenolith. Uncertainty is also potentially introduced through questions of whether the analyzed thin section is representative of trace phase abundance in the xenolith as a whole and indeed how well the xenolith population represents the lithological makeup of the lower crust. It is therefore likely that uncertainty in the mineral modes propagates to a large uncertainty in the calculated heat production. This uncertainty is likely magnified in metasedimentary xenoliths due to greater mineralogical diversity and generally greater HPE concentrations. To combat the shortcomings of the modal abundance calculations, the lower crustal heat production measurement is calculated and modeled on a basis of idealized crustal compositions/mineralogies (Chapter 4).

3.3 Reconstructed Bulk Rock Trace-Element Compositions

3.3.1 LA-ICP-MS Setup

Trace-element analysis was performed by laser ablation inductively coupled mass spectrometry (LA-ICP-MS) analyses using a Resonetics M-50 LR laser system in conjunction with a Thermo Element XR mass spectrometer. For the rare earth elements (REEs), internal standards, and the heavy heat-producing elements U and Th, LA-ICP-MS measurements were performed in low mass resolution mode for most minerals. The exception was monazite, which was analyzed for its U and Th concentrations via EPMA due to its small grain size and relatively high concentrations of these elements. During the ICP-MS analyses, longer dwell times were assigned to the HPEs as they are the primary focus of the study while all other analyzed elements are either utilized as internal standards or to confirm the mineral species. The isotope ^{39}K was measured in medium mass resolution (interference resolved from ArH$^+$ at mass resolution 5178) by LA-ICP-MS or via the EMPA if the mineral is particularly high in K (e.g. plagioclase, alkali feldspar, amphibole, biotite). The LA-ICP-MS resolution change requires each xenolith to be ablated during at least two separate sessions due to the requirement of different tuning parameters. The data from each analytical series were reduced using Iolite version 3.32 software. The NIST 612 SRM (standard reference material) was used as a primary calibration standard and data were compared to NIST 614 as a secondary standard, along with an additional mineral secondary standard similar to the material being ablated (e.g., garnet, rutile, apatite, zircon). All LA-ICP-MS analyses were corrected for instrumental drift and suppression effects through the use of an internal standard (^{43}Ca for-titanite, apatite, and most major minerals except orthopyroxene, ^{29}Si for orthopyroxene and, in some cases, garnet and plagioclase; ^{90}Zr-zircon, and ^{49}Ti, rutile and ilmenite), which was either quantified via EPMA or calculated through the stoichiometry of a mineral formula assuming mostly-idealized formulas.

Whereas the analytical conditions for each sample remained relatively constant throughout the project, variables such as laser repetition rate, spot size, and intensity were in some cases changed to ensure the laser coupled well with the sample surface and delivered a strong enough signal to the detector. The mineral data were then collected and put into a lower crustal mineral database (available in Appendix C).

3.3.2 Calculation of Heat Production

Equation 1 was used to calculate a reconstructed bulk-rock HPE (RHPE) concentration for each of the three major heat-producing elements U, Th and K:

$$\mathrm{RHPE}_{\mathrm{ppm}} = \left(\mathrm{n}_1 \cdot \mathrm{HPE}_{\mathrm{ppm}}\right) + \left(\mathrm{n}_2 \cdot \mathrm{HPE}_{\mathrm{ppm}}\right) + \cdots + \left(\mathrm{n}_i \cdot \mathrm{HPE}_{\mathrm{ppm}}\right) \quad \textbf{(1)}$$

where n_i is the proportion of a mineral i in the rock and HPE_{ppm} is concentration of that heat-producing element in mineral i.

These reconstructed bulk-rock concentrations of each of these heat-producing elements were then applied to Equation 2 from Hasterok and Chapman (2011) to calculate a bulk-rock heat production (A) value:

$$A = 10^{-5}\rho(3.5C_{K2O\,(wt.\%)} + 9.67C_{U(ppm)} + 2.63C_{Th(ppm)}) \quad \textbf{(2)}$$

where ρ is the density of the rock in kg/m^3, and C_{K2O}, C_U and C_{Th} are the concentrations of K_2O, U and Th, respectively, in the rock. As such, phases that contain high concentrations of HPEs or are volumetrically abundant in the rock were preferentially chosen for LA-ICP-MS analyses. Other minerals, such as kyanite, pyrrhotite, quartz, and ilmenite were generally not analyzed in most xenoliths after a few reconnaissance analyses showed that the HPE concentrations in these minerals is so low as to make a negligible contribution to the overall HPE budget of the whole rock.

Chapter 4: Sample Characterization

The mineralogical and textural diversity of the lower crustal xenoliths from the A-154 kimberlite pipes is manifest in a spectrum of lithologies. As noted by Krauss et al. (2007), the two most common lithologies are mafic granulites, which comprise both garnet two-pyroxene and garnet-clinopyroxene varieties, and aluminous metasedimentary granulites. All studied xenoliths in this sample set contain variable modal abundances of garnet and plagioclase, commonly in association with pyroxene. Garnet two-pyroxene granulites comprise clinopyroxene, orthopyroxene, garnet, and plagioclase constitute approximately 50 % of all xenoliths recovered from A-154. These include samples: 1140, 1214, 1525, 1542, 1638, MX-0125, and MX-0154.

Minor and trace minerals in these samples include amphibole, biotite, apatite, titanite, Fe-Ti oxides (magnetite, ilmenite, rutile), pyrrhotite, and rare zircon. Texturally, these samples are largely unfoliated though compositional banding occurs in some samples. In several samples, garnet and clinopyroxene form aggregates in banded regions leaving other portions of the sample devoid of garnet and rich in plagioclase. Orthopyroxene exists in varying proportions in each of these garnet two-pyroxene xenoliths and its presence indicates that the xenolith probably formed at lower pressures than that of the orthopyroxene-free, garnet-clinopyroxene granulites (Pattison, 2003). The latter make up 25 to 30 % of the available A-154 granulite xenoliths and comprise mainly garnet, clinopyroxene, and plagioclase. In this project, the single pyroxene samples are: 1030, 1612, MX-0011, MX-0111, and 1654. Hydrous phases are less common in single pyroxene garnet granulites than in the two-pyroxene garnet granulites. These samples are also generally less altered than some of the two-pyroxene granulites and are commonly less texturally diverse than the orthopyroxene-bearing granulites.

The aluminous group of granulite xenoliths likely represent metamorphosed semi-pelitic and pelitic sediments. These rocks comprise roughly 20 % of this sample set. The aluminous/metasedimentary xenoliths in this project include samples: 1554, DDM-20, and DDM-303. The mineralogy of these samples can be highly variable and diverse but generally includes quartz, potassium feldspar, garnet, plagioclase, orthopyroxene, rutile, zircon, apatite, monazite, and hydrous phases such as amphibole and biotite. Some gneissic fabric is present within these samples. Metasedimentary granulites are differentiated from the other granulite species due to the occurrence of primary quartz, alkali feldspar, and sparse kyanite, generally indicative of a semi-pelitic to pelitic protolith (see Bucher and Frey, 2002 pp. 217-258 for review). The powdered whole-rock composition of the xenoliths gathered via Krauss et al. (2007) and the Peter Hooper

GeoAnalytical Lab at Washington State University (Johnson et al. 1999) indicate that the petrographically identified metasediments have lower calcium contents than the otherwise mafic samples, reflecting the lack of clinopyroxene and lower grossular content of the garnets (Figure 1).

Chapter 5: Results

5.1 Thermometry

Mineral concentrations measured via EPMA can be used to estimate the re-equilibration temperature recorded by garnet and its associated ferromagnesian phase. This study utilizes the Fe^{2+}-Mg exchange thermometer calibrations of Krogh-Ravna (2000b) for garnet-clinopyroxene, Krogh-Ravna (2000a) for garnet-amphibole, and five widely-used calibrations for garnet-biotite (Ferry and Spear, 1978; Hodges and Spear, 1982; Perchuk and Lavrent'eva, 1983; Kleeman & Reinhardt, 1994; Holdaway, 2000). Due to analytical and calibration uncertainties, a blanket error for the thermometry is assumed to be ± 50 °C.

However, before temperature calculations are made, the retrograde zoning profiles in the minerals of interest must be assessed and the appropriate mineral analyses from these profiles selected as input for the calculations. Figure 2 presents representative rim-to-core zoning profiles of Mg/(Mg+Fe) for each of the mineral relations. The garnet analysis within 5 μm (the closest possible) of the biotite-garnet interface has the lowest Mg number (Mg#) indicating the greatest amount of down-temperature Fe^{2+}-Mg equilibration with the adjacent biotite. As such, this garnet rim analysis was the one used in the garnet-biotite temperature calculation.

The temperatures using all four calibrations of the garnet-biotite geothermometer noted above were calculated assuming a pressure of 10 kbar, as this was the average metamorphic pressure of Diavik lower crustal xenoliths reported by Krauss et al. (2007), which reports a range

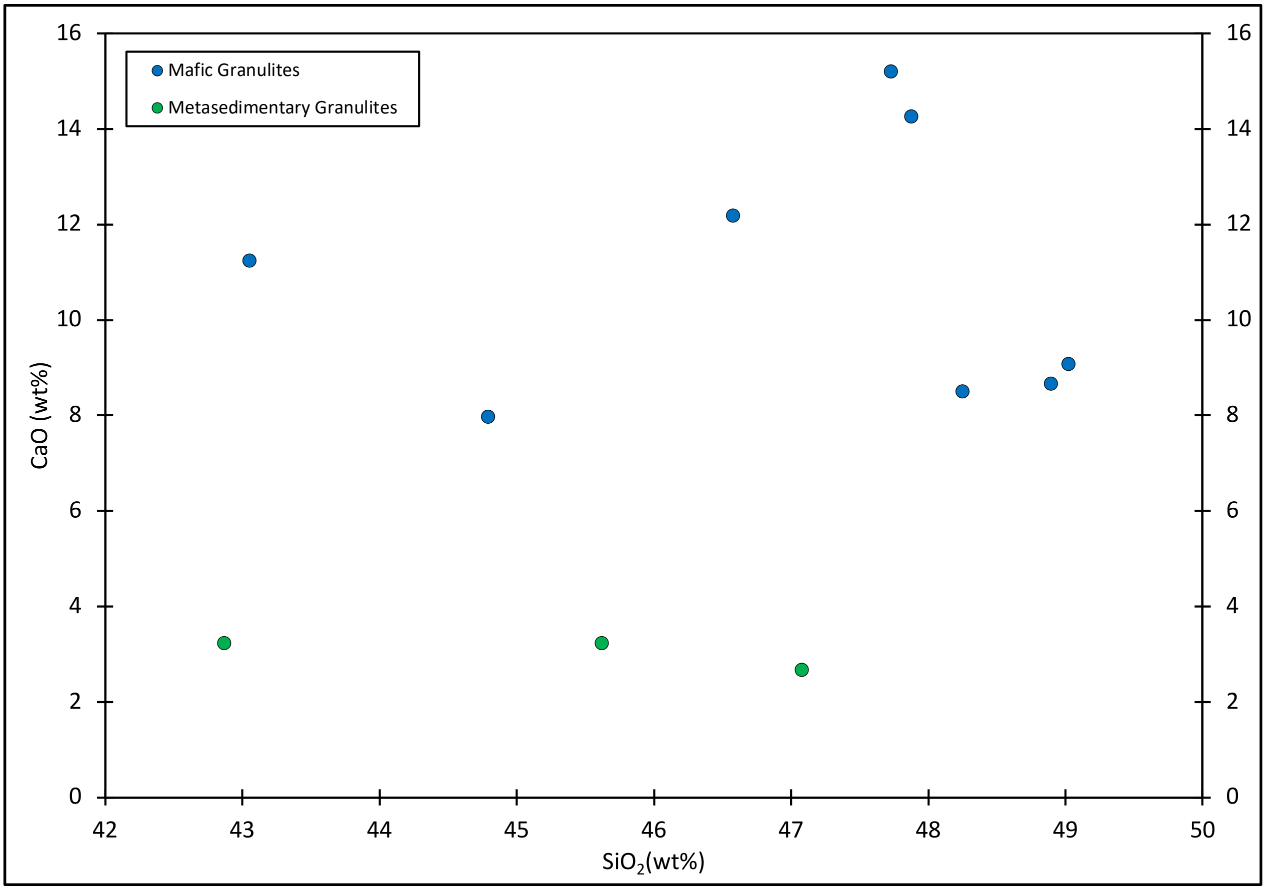

Figure 1. The whole-rock compositions of 11 of the 15 xenoliths examined in this study. Metasedimentary granulites, identified on a basis of petrography, have considerably lower CaO contents. Whole rock analyses performed by Peter Hooper Geoanalytical Lab (Johnson et al. 1999) and also gathered from Krauss et al. (2007). Data in available in Appendix A.

of 9-11 kbar. Calculated biotite-garnet temperatures are presented in Table 2. Multiple temperatures are sometimes reported for a single xenolith (e.g., xenolith 1542) in cases where there are several mineral pairings/associations suitable for thermometry. The calculated temperatures span a range from 450°C -800°C and inclusion temperatures are generally lower than touching temperatures, as is expected. In general, the Ferry and Spear (1978) calibration yields the lowest average temperature while the Holdaway et al. (2000) calibration gives the highest in most cases. It should be noted that the Ferry and Spear (1978) experimental calibration of the garnet-biotite geothermometer was done in a Ca-free system. Thus, application of this calibration to natural samples assumes that the presence of Ca in garnet has no effect on its Fe^{2+}-Mg partitioning behavior. This assumption is now known to be incorrect (e.g., Hodges and Spear, 1982) and results in spuriously low calculated temperatures if, as is the case in the present study, garnet contains significant Ca. The Hodges and Spear (1982) calibration of the geothermometer is based primarily on the Ferry and Spear (1978) experiments but uses non-ideal Ca-Fe-Mg mixing parameters in garnet to account for the effect of Ca on Fe-Mg partitioning. Given these observations, the garnet-biotite temperatures obtained with the Ferry and Spear (1978) calibration, though reported in Table 2, are not considered in the interpretation of results.

Fluorine in biotite and amphibole was also analyzed during this project (Appendix B2), and its concentration is generally higher (> 1 wt%) in biotite grains that give lower calculated equilibration temperatures (e.g., 1542, DDM-20). This may be due to the Fe^{2+}-F avoidance principle proposed by Rosenberg and Foit (1977) in which high F biotite has a greater affinity for Mg (relative to Fe^{2+}) than pure hydroxy biotite, which results in a higher biotite Mg# in higher F biotite and thereby a lower calculated biotite-garnet temperature. The study by Perchuk & Aranovich (1984) attempts to quantify and correct for the effect of F on biotite temperatures.

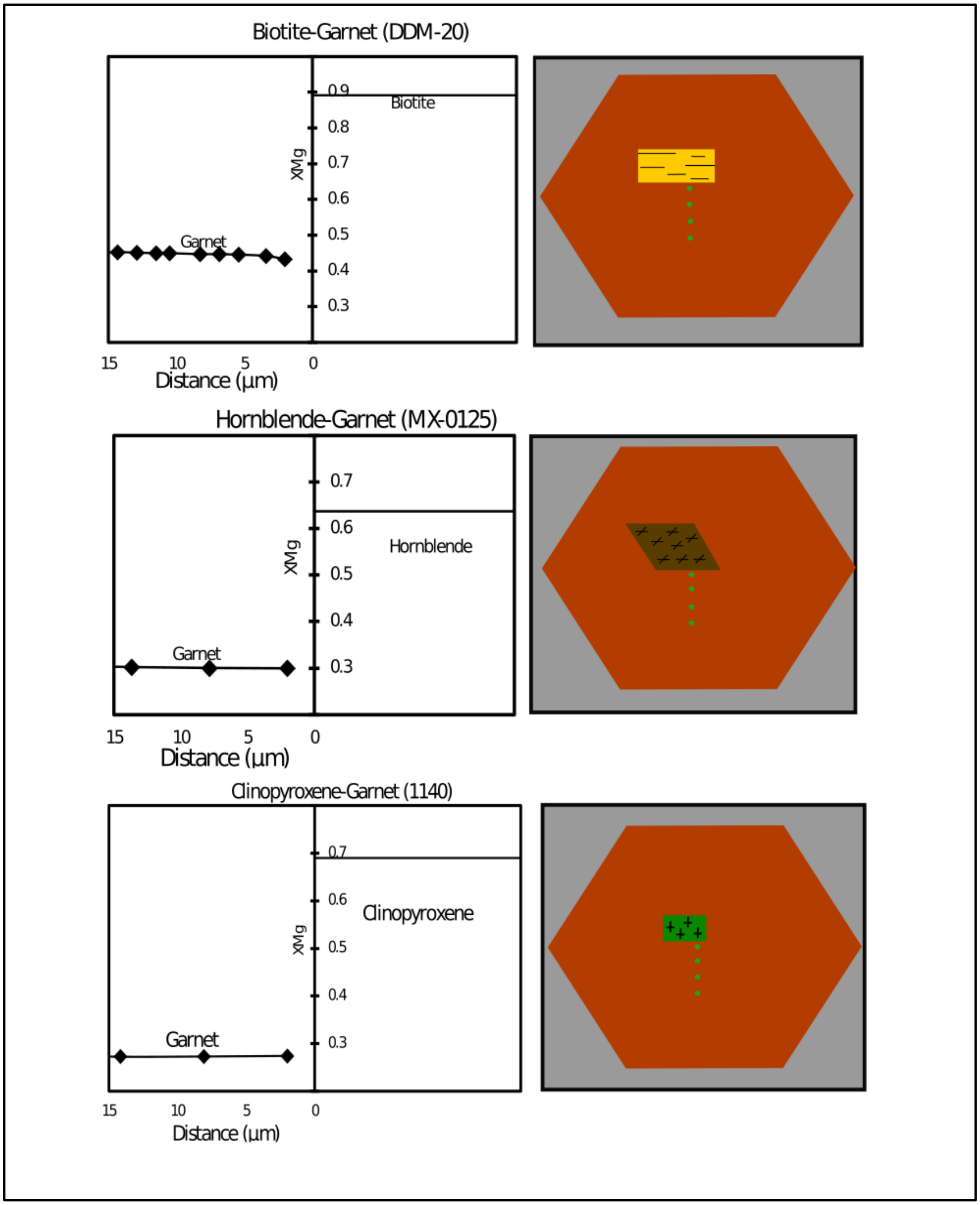

Figure 2. Mg# zoning profiles in garnet near interface with inclusions of biotite, hornblende, and clinopyroxene. Note the slight decrease in garnet Mg# at the garnet-biotite interface.

Table 2. Calculated Garnet-Biotite Temperatures

Sample #	*Rock Type*	*Relationship*	*FS*	*HS*	*KR*	*PL*	*H*	*Avg.*
DDM-20	Metased.	Inclusion	416	446	444	487	507	471
1542	Mafic	Inclusion	428	489	491	495	545	505
1542	Mafic	Inclusion	526	589	579	556	619	586
1542	Mafic	Inclusion	449	507	504	509	561	520
1542	Mafic	Touch	457	518	515	514	569	529
1542	Mafic	Touch	486	545	540	532	585	551
MX-0154	Mafic	Inclusion	490	558	554	535	591	560
MX-0154	Mafic	Touch	529	605	593	558	617	593
MX-0154	Mafic	Touch	552	627	610	571	631	610
MX-0154	Mafic	Touch	535	606	595	562	622	596
MX-0154	Mafic	Touch	544	614	599	567	622	601
1554	Metased.	Inclusion	473	515	521	524	559	530
1554	Metased.	Touch	493	531	536	537	573	544
1554	Metased.	Touch	498	528	523	539	568	540
1554	Metased.	Touch	467	507	516	520	556	525
1554	Metased.	Touch	565	612	605	579	635	608
MX-0125	Mafic	Touch	601	671	638	591	649	637
MX-0125	Mafic	Touch	666	748	706	633	694	695
MX-0125	Mafic	Touch	648	728	689	624	680	680

Biotite-garnet temperatures (°C) calculated from various calibrations of Fe-Mg^{2+} exchange in the system. Reported temperatures are calculated based on the rim garnet coupled with the averaged biotite composition in each mineral pair. *FS* (Ferry and Spear, 1978), *HS* (Hodges and Spear, 1982), *PL* (Perchuk and Lavrent'eva, 1983), *KR* (Kleemann and Reinhardt 1994), and *H* (Holdaway et al., 2000). The column labelled Avg is the average of temperatures given by all calibrations excluding FS.

Utilizing their methodology, temperatures gathered from samples DDM-20 and 1554 are likely underestimates of the lower crustal temperature. The magnitude of the fluorine effect on biotite's Fe^{2+}-Mg partitioning behavior is not well understood and so the calculated garnet-biotite temperatures are taken as is regardless of the biotite fluorine content.

While not representing the lowest temperatures calculated for the lower crustal sample suite, amphibole-garnet relationship were also analyzed in a similar approach to the garnet-biotite relationships, to test the amount of retrograde equilibration between these two minerals and to see what they reveal about the lower crustal thermal history. Calculated hornblende temperatures span a range of ~524-627°C with an average of 576°C. Zoning profiles are again presented in Figure 2, while the analyses and calculated temperatures of the first point in the analytical traverse (similar to the biotite) are utilized (Appendix B2) for the temperature calculations, which are reported in Table 3. Unlike with the biotite-garnet relationships, the decrease in the garnet Mg# during a core-to-rim traverse is not present in the hornblende-garnet system. In addition, within this group the temperature variation between samples is much more limited than in the biotite-garnet system and there is no apparent effect of F interaction creating lower calculated temperatures.

The garnet-clinopyroxene thermometer gives distinctly high temperatures (~ 600 to 750 °C; average of 687 °C) in comparison to the other two mineral-pair geothermometers examined (Appendix B2). Rim to core profiles (Figure 2) also do not show the Mg# increase observed in the biotite-garnet profiles and the temperatures calculated across a traverse do not show much variation or dispersion to higher temperatures. This indicates significantly less retrograde Fe^{2+}-Mg exchange between garnet and clinopyroxene than between the other mineral pairs investigated in this study. Indeed the average temperature obtained from the compositions of clinopyroxene inclusions and touching garnet (~ 650 °C) is only about 100 to 200 °C lower than the peak

Table 3. Hornblende Temperatures

Sample #	*Rock Type*	*Relationship*	*Krogh-Ravna (2000a)* (°C)
1214	2-pyx mafic	Inclusion	549
1214	2-pyx mafic	Inclusion	524
1214	2-pyx mafic	Inclusion	556
1214	2-pyx mafic	Inclusion	576
1214	2-pyx mafic	Inclusion	585
1214	2-pyx mafic	Inclusion	575
1214	2-pyx mafic	Inclusion	625
1214	2-pyx mafic	Inclusion	570
1214	2-pyx mafic	Inclusion	553
MX-0154	2-pyx mafic	Inclusion	560
MX-0125	2-pyx mafic	Touch	606
MX-0125	2-pyx mafic	Touch	627
MX-0125	2-pyx mafic	Touch	578
MX-0125	2-pyx mafic	Touch	584

Hornblende temperatures from the EPMA data in appendix B2, temperatures are the first point of an analytical traverse and are the closest to the garnet-hornblende contact.

metamorphic temperature estimated for these xenoliths based on core compositions (Krauss et al., 2007). Recent studies of Fe^{2+}-Mg diffusion in clinopyroxene (Müller et al., 2013) and garnet (Borinski et al., 2012) support this claim as they indicate that the diffusion rate in clinopyroxene is actually 5 to 10 times slower than it is in garnet. As such, even the lowest temperatures recorded by this geothermometer reflect the relatively high closure temperature of Fe^{2+}-Mg exchange between garnet and clinopyroxene rather than the ambient temperature of the Slave craton lower crust at the time of kimberlite magmatism. Individual temperatures are available in Appendix B.

5.2 Heat production in the Lower Crust

Because kimberlite magma infiltration along some of the grain boundaries of lower crustal xenoliths make whole-rock major and trace-element analyses unreliable, bulk-rock HPE concentrations in these rocks were estimated by combining modal data on the xenoliths with data on the HPE concentrations of individual minerals obtained by LA-ICP-MS or EPMA. This calculated whole-rock composition is henceforth called a "reconstructed bulk-rock composition". In samples with multiple HPE analyses for individual minerals, the average value is utilized for the calculation. The reconstructed heat production values for the Diavik xenoliths ranges from 0.04 - 0.31 $\mu W/m^3$; with an average of 0.16 ± 0.08 $\mu W/m^3$ (n=15). While the chemical data collected for individual minerals in these rocks are precise, significant uncertainty is imbedded in the reconstructed heat production values because of uncertainties in the mineral modes compounded with the question of whether the xenoliths investigated in the present study are in fact representative of the lower crust in the Slave craton (Section 3.2). To remove this bias, the measured HPE concentration data on a per-mineral basis is utilized to calculate heat production values for idealized lower crustal rocks based on an assumed mineralogy and mineral abundances.

5.3 Range of Crustal Heat-Production Values

Using this approach, a range of lower crustal heat production values can be calculated assuming an idealized very HPE-depleted mafic lower crust end-member and a relatively enriched metasedimentary lower crust end-member. Examples of both end members are present in lower crustal xenoliths from the Diavik A-154 kimberlite pipe. It can be shown that the average heat production value (0.16 ± 0.08 $\mu W/m^3$) derived from reconstructed bulk rock compositions of 15 individual xenoliths is comparable to that derived from two-component mixing between idealized mafic and metasedimentary end members (Section 3.3.3). The individual xenolith reconstructions are presented with their modal abundance data (Section 3.1) in Table 4 and summarized through box and whisker plots in Figure 3. The median values and the median absolute deviations (uncertainty) are presented in Table 5 and a full database of analyses is available in Appendix C.

5.3.1 Depleted Lower Crust

An idealized mafic lower crust is taken to contain equal parts plagioclase, clinopyroxene, and garnet. A similar mineralogy is present in the xenolith 1654, where only these major minerals comprise the rock and no trace phases (e.g., apatite, zircon, rutile) are present. Using Equation 1 in conjunction with the HPE concentrations from Table 5 and Figure 3, the concentration of the HPE can be created for an idealized, three-mineral mafic lower crust. Potentially, minimum HPE concentrations in these minerals can be utilized to create an absolute lower bound for HPE concentration in the lower crust; however, this yields a heat production value of 0.01 $\mu W/m^3$, which is comparable to the optimized mantle heat production value of 0.012 $\mu W/m^3$ of Russell et al. (2001) and is therefore likely too low to represent a realistic lower crust heat production. To remedy this, the median HPE concentrations measured for the plagioclase, clinopyroxene and

Table 4. Reconstructed Heat Production Values for Xenoliths

Sample	Type	Method	# of point counts	Kfs	Amp	Ap	Bt	Cpx	Grt	Ilm	Ky	Mnz	Mnz*	Opx	Pl	Po	Qtz	Rt	Scp	Ttn	Zrn	HP
1030	M	PC	587	n.d.	n.d.	0.3	0.0	15.1	26.7	-	n.d.	n.d.	n.d.	n.d.	57	-	n.d.	0.80	n.d.	n.d.	-	0.09±0.05
1140	M	Q	n/a	-	0.8	0.3	n.d.	21.5	12.0	2.6	n.d.	n.d.	n.d.	20.6	42.2	-	n.d.	3.3	n.d.	n.d.	0.02	0.10±0.01
1214	M	PC	378	n.d.	17.0	0.3	n.d.	16.4	19.3	1.0	n.d.	-	n.d.	17.2	28.7	-	n.d.	-	n.d.	n.d.	0.01	0.16±0.01
1525	M	PC	501	n.d.	2.0	0.2	0.0	55.7	0.0	1.8	n.d.	n.d.	n.d.	6.8	33.4	-	n.d.	0.0	n.d.	n.d.	0.01	0.10±0.01
1542	M	PC	424	n.d.	2.6	0.3	3.2	25.3	17.3	1.55	n.d.	n.d.	n.d.	7.6	39.8	-	n.d.	2.2	n.d.	n.d.	-	0.27±0.03
1554	F	Q	n/a	2.76	0.1	0.01	-	0.2	66.8	1.4	0.3	0.00	0.002	0.2	25.9	1.4	n.d.	1.0	n.d.	n.d.	0.04	0.31±0.01
1612	M	PC	429	n.d.	n.d.	0.1	0.2	42.9	15.8	0.5	n.d.	n.d.	n.d.	-	40.5	-	n.d.	0.04	n.d.	n.d.	-	0.17±0.08
1638	M	PC	268	n.d.	-	0.3	n.d.	19.4	22.3	0.5	n.d.	n.d.	n.d.	8.0	48.2	n.d.	n.d.	0.4	0.8	n.d.	-	0.12±0.002
1654	M	PC	244	n.d.	n.d.	n.d.	n.d.	47.1	18.9	n.d.	n.d.	n.d.	n.d.	n.d.	34.0	n.d.	n.d.	0.0	n.d.	n.d.	n.d.	0.11±0.01
DDM-20	F	PC	461	5.0	n.d.	0.1	-	n.d.	19.2	0.3	-	0.002	0.002	0.4	38.9	-	35.8	0.2	n.d.	n.d.	0.01	0.17±0.03
DDM-303	F	Q	n/a	7.4	0.26	0.04	n.d.	-	27.1	0.2	0.6	-	n.d.	-	60.9	2.2	n.d.	1.3	n.d.	n.d.	0.03	0.31±0.02
MX-0011	M	Q	n/a	-	-	0.3	n.d.	48.1	19.6	0.3	n.d.	n.d.	n.d.	-	29.9	1.0	n.d.	0.4	n.d.	0.5	-	0.16±0.02
MX-0111	M	Q	n/a	0.11	0.09	0.13	n.d.	43.6	37.7	2.1	n.d.	-	n.d.	-	16.2	0.1	n.d.	-	n.d.	-	-	0.04±0.004
MX-0125	M	PC	387	n.d.	14.8	0.2	2.6	31.2	25.3	0.8	n.d.	n.d.	n.d.	n.d.	25.1	n.d.	n.d.	n.d.	n.d.	n.d.	0.01	0.18±0.01
MX-0154	M	PC	430	n.d.	n.d.	0.1	1.8	11.4	37.1	1.2	n.d.	n.d.	n.d.	1.4	45.1	-	n.d.	0.2	n.d.	1.6	0.01	0.15±0.02

Modal abundances are presented in volume percent. Uncertainties are a propagation of the analytical uncertainties in Appendix C, uncertainties in the abundances are assumed to be large and are not included in the uncertainty. “-“ indicates the mineral being present in negligible or nonquantifiable amount, “n.d.” indicates that the phase was not detected in the xenolith. “PC” indicates a point count while “Q” represents a QEMSCAN ® analysis. “M” represents a mafic xenolith while “F” represents a metasedimentary xenolith. “Mnz*” represents monazite with a higher than normal Th content and is calculated separately than other monazite. Mineral abbreviations are that of Kretz, (1983) and Whitney and Evans (2010). Heat production is reported in μW/m^3.

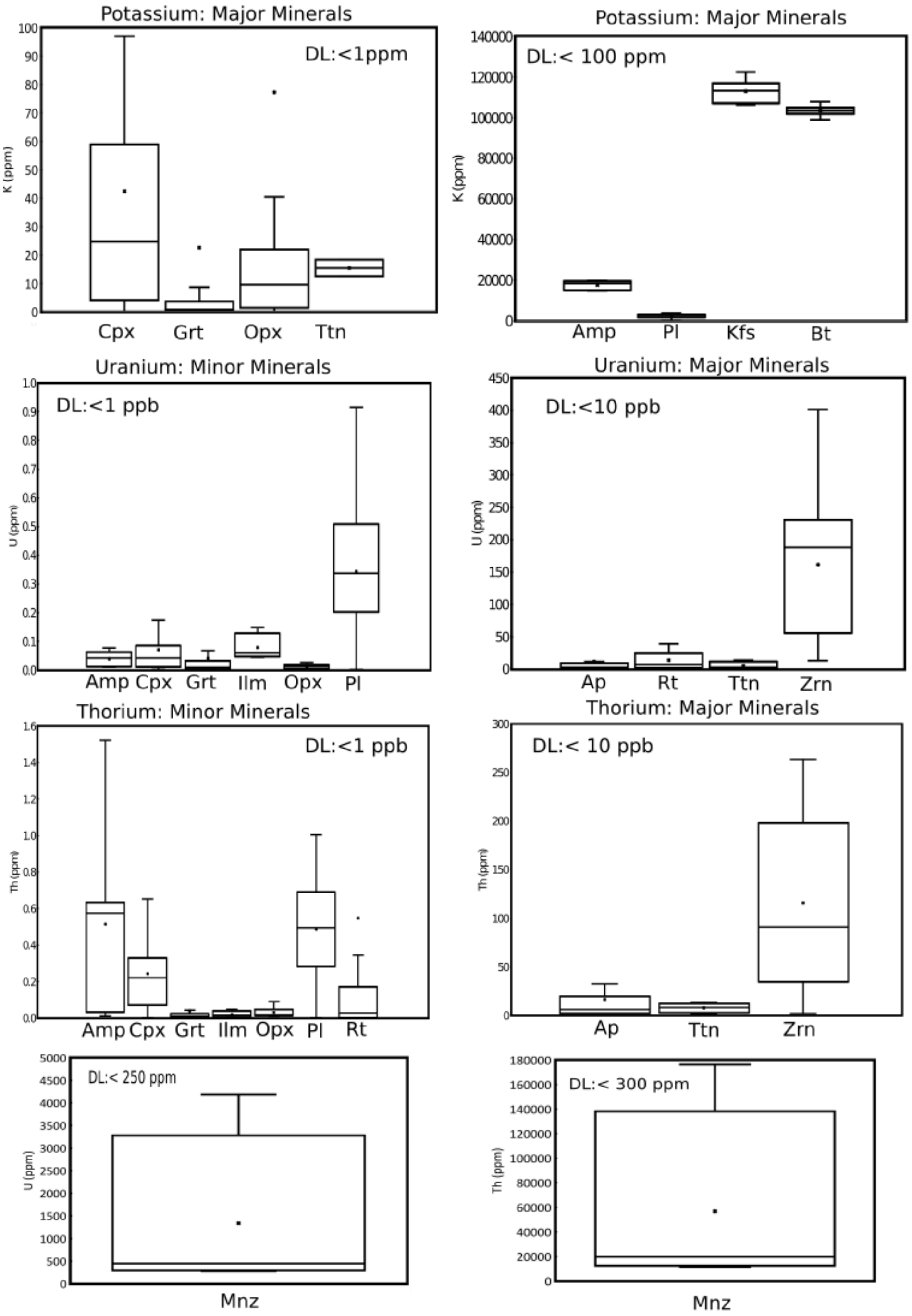

Figure 3. Box and whisker plots of the elemental concentrations collected in this study, the standard mean is marked as a dot. The center line is the median and the box is bounded by the 1st and 3rd quartiles. Detection limits for trace K, U, and Th are averages and calculated by the method of Pettke et al. (2012). Detection limits for K in phases where it is a major or minor element and for Th and U in monazite are calculated using the Probe for EPMA software (Donovan et al. 2015). Mineral abbriviations are of Whitney & Evans (2010) and Kretz (1983).

garnet are utilized here and yield a heat production value of 0.08 ± 0.01 μW/m^3 for the mafic "depleted" lower crust. This value is lower than the 0.19 μW/m^3 estimate of Gao and Rudnick (2003) for the lower crust but higher than some estimates for subcratonic lithospheric mantle (e.g., Russel et al., 2001). Uncertainties here are a propagation of the HPE median absolute deviations on a per mineral basis (Table 5).

5.3.2 Enriched Lower Crust

Metasedimentary xenoliths are present in the xenolith sample set and are relatively enriched in incompatible elements and HPEs compared to the mafic rocks. These samples tend to be devoid of clinopyroxene but have sizable amounts of garnet and plagioclase as well as minerals such as alkali feldspar, rutile, zircon, apatite, and monazite. Using a well-constrained mineralogy from a xenolith (sample DDM-303), an "enriched" lower crust is reconstructed using the median HPE concentrations from Table 5. Utilizing a density of 3000 kg/m^3 ("metapelite;" Gao et al., 2000) results in a maximum lower crustal heat production of 0.37 ± 0.06 μW/m^3.

5.3.3 A Potential Crustal Estimate

These two estimates allow for a range of lower crustal heat production values to be calculated based on these two end-member compositions. As the A-154 kimberlite pipe hosts both mafic and metasedimentary granulites, it is convenient to model the lower crust as a binary mixture of these end-members. The observed proportion of the two xenolith types in the sample collection yields a model lower crust comprising roughly 20 % metasedimentary granulites and 80 % mafic granulites. This mixture has a weighted average rock density of 3164 kg/m^3 (from metapelite-mafic granulite densities reported by Gao et al., 2003) and a weighted average heat production value of 0.14 ± 0.02 μW/m^3. These results are summarized in Table 6, along with the average xenolith heat production.

Table 5. Chemical Data

Mineral	*K Method*	*U, Th Method*	*n(K)*	*n (U,Th)*	*K (ppm)*	*U (ppm)*	*Th (ppm)*
Amphibole	EPMA	ICP-MS	33	13	18000 ± 1300	0.04 ± 0.02	0.58 ± 0.04
Apatite	N/A	ICP-MS	-	57	-	2.4±2.1	6.2 ± 6.1
Biotite	ICP-MS	ICP-MS	15	4	83500 ±600	0.02 ± 0.02	0.02 ± 0.02
Clinopyroxene	ICP-MS	ICP-MS	51	54	25 ±22	0.06 ± 0.04	0.25 ± 0.15
Garnet	ICP-MS	ICP-MS	49	78	2.2±2.2	0.01 ± 0.01	0.01 ± 0.01
Ilmenite	N/A	ICP-MS	-	4	-	0.08 ± 0.02	0.02 ± 0.01
Alkali Feldspar	EMPA	ICP-MS	17	1	113000 ± 1200	0.05 ± 0.05	0.09 ± 0.09
Orthopyroxene	ICP-MS	ICP-MS	12	18	12±9	0.01 ± 0.01	0.01 ± 0.01
Plagioclase	EPMA	ICP-MS	266	114	2700 ± 500	0.40 ± 0.16	0.55 ± 0.20
Monazite	N/A	EPMA	-	17	-	550 ± 200	16000 ± 7000
Rutile	N/A	ICP-MS	-	26	-	6.5 ± 0.16	0.67 ± 0.43
Scapolite	EPMA	ICP-MS	1	1	1500±100	0.79 ±0.02	1.12±0.01
Titanite	ICP-MS	ICP-MS	4	7	15 ± 12	2.2 ± 1.1	8.0± 3.0
Zircon	N/A	ICP-MS	-	11	-	188 ± 129	91 ± 73

The HPE concentrations of the various minerals studied in this project presented as median values of the whole dataset (Appendix C1). “n” values represent the total amount of analyses of each mineral species. Uncertainties are reported as median absolute deviation.

Table 6. Different Crustal Models

Crust	*% Enriched*	*% Mafic*	*Density (kg/m^3)*	*K (ppm)*	*U (ppm)*	*Th (ppm)*	*HP ($\mu W/m^3$)*
Depleted	0	100	3200	900	0.15	0.27	0.08±0.01
Mix	20	80	3161	2700	0.20	0.53	0.14±0.02
Xenolith Average	-	-	3160	3000	0.27	0.49	0.16±0.08
Enriched	100	0	3000	10000	0.42	1.6	0.37±0.06

The HPE concentrations of the three derived crustal models. Density for the mixed crust is a best estimate fit to the HPE mixture. Uncertainty is presented as a propagation of mineral median absolute deviates as a function of heat production. Modal abundance uncertainty is not included in the xenolith average.

Chapter 6: Discussion

6.1 Ambient Lower Crustal Temperatures

Garnet-amphibole and garnet-clinopyroxene thermometers record minimum temperatures of 590 and 525 °C, respectively. Most of the temperatures indicated by the garnet-clinopyroxene thermometer exceed 600 °C, which is too high for an ambient lower crustal temperature in a cratonic regime (e.g., higher than the Superior craton in Jaupart et al., 2014). Thus, as discussed in Section 3.1, it is likely that garnet-clinopyroxene temperatures reflect the closure temperature of Fe^{2+}-Mg exchange between these minerals rather than the present-day temperature of the Slave craton lower crust. The lowest amphibole temperature (524 °C) is significantly lower than the lowest garnet-clinopyroxene temperature (Fig. 4) but may still represent the closure temperature of Fe^{2+}-Mg exchange in this system rather than the true ambient lower crustal temperature.

Of the three mineral exchange types (biotite-garnet, hornblende-garnet, and clinopyroxene-garnet)investigated in the present study, the system likely to have the lowest Fe-Mg elemental closure temperature is the garnet-biotite thermometer (Lasaga, 1983; Ghent and Stout, 1986). As such, this thermometer potentially provides the most robust estimate of the ambient temperature of the lower continental crust beneath the Diavik kimberlite. The average of biotite-garnet temperatures given by the various calibrations (excluding Ferry and Spear, 1978) range from 480-710 °C (Table 2). Most of these temperatures are lower than 600 °C and the inclusion temperatures, which are hypothesized to more readily re-equilibrate during cooling, are typically less than 550 °C, with several lower than 500 °C. Notably, the lowest recorded hornblende-garnet temperature (524 °C) is generally comparable with the lowest biotite-garnet temperatures.

Previous estimates for the Slave craton Moho vary between ~ 350 and 500 °C, depending on the method utilized. These methods typically involve estimates from a reference geotherm or are mathematically deduced from other geophysical factors. For example, the mantle geotherm presented by Russell et al. (2001) for the Jericho pipe (an older kimberlite pipe from the northern Slave craton) estimates a Moho temperature of 469 °C. Lewis et al. (2003) estimated Moho temperatures of ~ 350 to 500 °C through a variety of methods, which act as a bounding range of estimates for the Slave craton Moho (Figure 4).

With the exception of two mineral pairs, most biotite-garnet temperatures calculated in this study fall above the geophysically-based estimates of Moho temperature range with the exception of two high F garnet-biotite pairs. This indicates that the garnet-biotite temperatures, along with the garnet-clinopyroxene and garnet-hornblende temperatures, likely represent closure temperatures of Fe^{2+}-Mg exchange in these systems and are only a maximum estimate of lower crustal temperature at the time of kimberlite eruption. Temperatures that plot within the Moho temperature range were derived from mineral pairs where biotite have high F content (> 2 wt%) and are therefore potentially underestimating their temperature due to the Fe^{2+}-F avoidance principle (Rosenberg and Foit, 1977; Perchuk and Aranovich, 1984). As such, the thermometric estimates on mineral pairs all indicate a maximum temperature of the Slave craton Moho to be ~ 520 °C at the time of kimberlite eruption.

6.2 Lower Crustal Heat production across rock types

The present study models the heat production values of both an end-member mafic and end-member enriched lower crust as well as a mixed lower crust comprising mafic and metasedimentary granulite in 4:1 proportions as found in xenoliths from the A-154 kimberlite. These different models create a rather extreme range of heat production values (0.08 $\mu W/m^3$ to

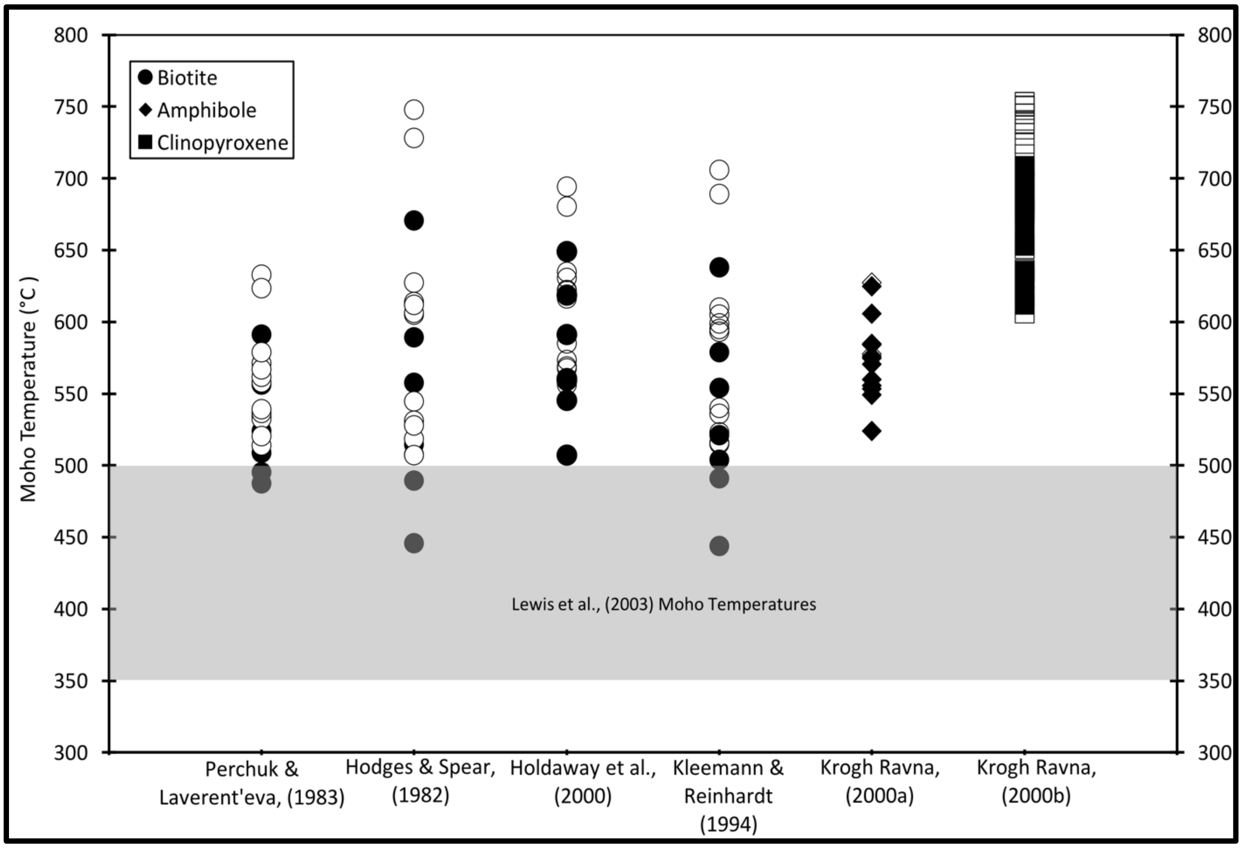

Figure 4. Calculated retrograde garnet-biotite, garnet-amphibole and garnet-clinopyroxene temperatures (this study) compared to previous literature estimates of Moho temperatures (Lewis et al., 2003). Filled symbols represent temperatures recorded by garnet-inclusion mineral pairs whereas open symbols temperatures recorded by garnet-touching mineral pairs. Garnet-biotite temperatures are based on the calibrations of Hodges and Spear (1982), Kleemann and Reinhardt (1994), Perchuk and Lavrent'eva (1983), and Holdaway (2000). Garnet-hornblende, garnet-clinopyroxene temperatures are based on the calibrations of Krogh-Ravna (2000a,b).

$0.37\mu W/m^3$) for the lower crust, which in turn propagates to differences in calculated crustal geotherms. Figure 5 plots the heat production of rocks as a function of rock density, which in this case is a proxy for "felsic" (lower density) and "mafic" (higher density).

Certain highly HPE-enriched minerals are more plentiful in the metasedimentary rocks than in the depleted mafic granulites and likely generate more variance in the estimation of heat production in this rock type. Minerals such as alkali feldspar, zircon, rutile, and monazite have high to very high concentrations of HPE and are present in greater abundances in the more enriched, metasedimentary samples; however, the higher silica contents of these samples make them less dense than their mafic counterparts. This causes the relationship between rock density and heat production to be slightly non-linear, as heat production is dependent on both density and the concentration of HPEs.

Table 7 compares the three HPE concentrations calculated in this study with those from literature. The mixed sample heat production value is similar to that of Gao and Rudnick (2003) and Huang et al. (2013), which were both based on geophysical estimates of lower crustal compositions and indicate that the lower crust of the Slave craton is dominated by mafic rocks. The depleted (mafic) granulite xenolith sample from this study has the lowest calculated heat production compared to all other studies. In particular, it has the lowest reported U and Th concentrations and a much lower K content owing to it being modeled on an alkali feldspar-free basis with most of the potassium residing in plagioclase (~ 0.02 wt% K_2O). In addition, the reconstructed bulk compositions effectively screen out grain boundary K and Th contamination from the host kimberlite, decreasing some of the enrichment of these elements in bulk-rock analysis of kimberlite-hosted xenoliths. The estimate of the proportion of enriched Slave craton lower crust is within the range of values reported in literature but still lower than the average value

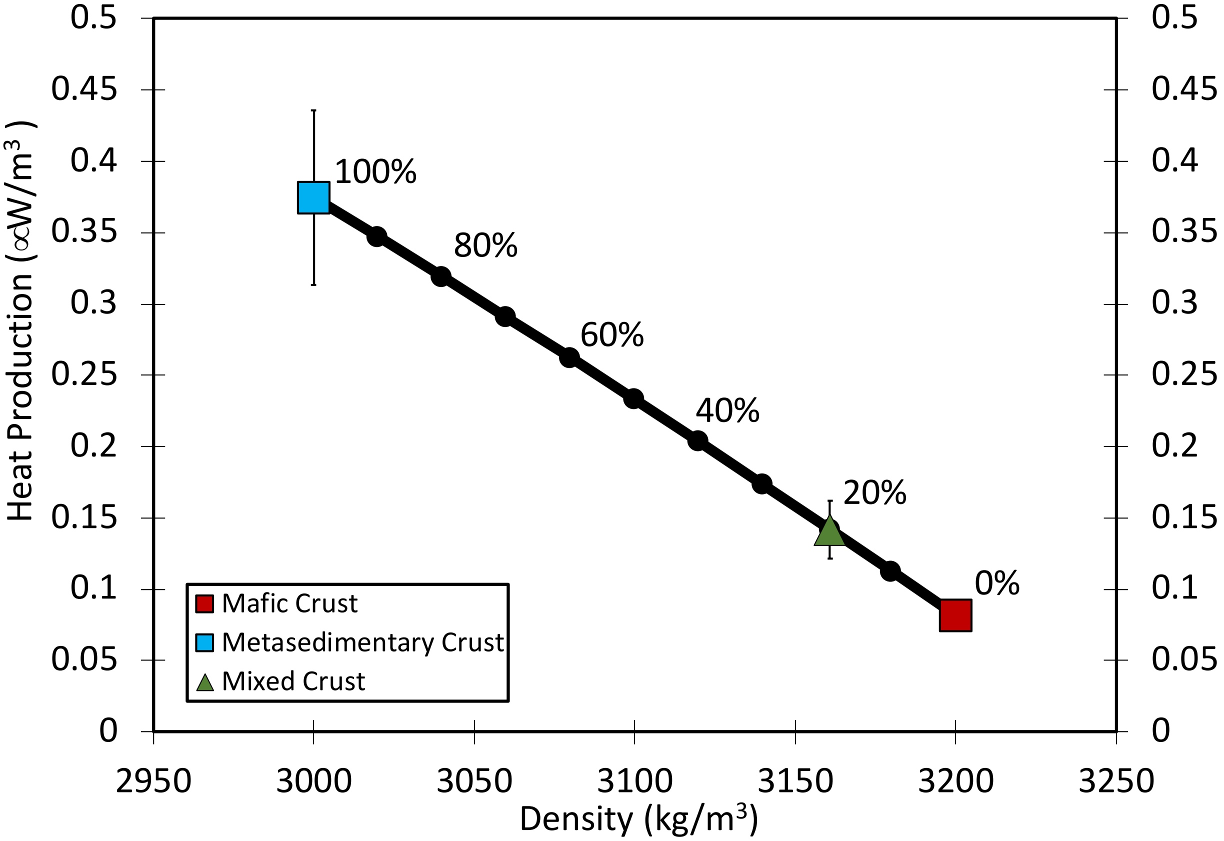

Figure 5. Heat production for a mix between the calculated mafic granulite and metasedimentary granulite end members. The numbers along the mixing line represent the percentage of the metasedimentary end member in the mix. Metasedimentary xenoliths make up approximately 20% of the Diavik lower crustal xenolith collection and therefore the estimated heat production of the bulk lower crust beneath Diavik is indicated by the green symbol.

(Table 7), potentially due to the studied Diavik xenoliths originating from ancient cratonic lower crust. It is also worth noting that the enriched estimate is nearly equivalent to the lower crustal heat production of Hasterok and Chapman (2011), indicating that for their model geotherms to be applicable to the Lac de Gras region, the lower crust would need to be entirely made up of metasedimentary rocks. As such, these estimates yield a lower heat production than estimates made for non-cratonic crust, such as Hacker et al. (2011), who give a heat production value that is 80 % higher than the enriched estimate.

While generally more depleted than some of the literature models, the heat production estimates in this are comparable with low end estimates of deep crust heat production. Figure 6 shows these literature values in comparison with others in the literature as a function of crustal thickness. In general, active margin lower crustal estimates fall into the $> 0.5\ \mu W/m^3$ and > 45 km zones while stable cratonic areas and passive margins roughly group to under $0.5\ \mu W/m^3$ and between 30 to 45 km This is potentially due to greater degrees of HPE enrichment at subduction zones (e.g., Hacker et al., 2011) or thickened crustal sections such as is the case of the Kohistan arc (Jagoutz and Schmidt, 2012).

6.3 Heat Production Time Dependence

As heat production is dependent on the time-integrated decay of radioactive nuclides, heat production today is reduced compared to times in the geologic past. Using the half-lives (Turcotte and Schubert, 2002) of the four radioactive isotopes relevant to this project (^{235}U, ^{238}U, ^{232}Th, ^{40}K), the heat production of present-day composition lower crust can be calculated back to Hadean times. It should be noted, however, that whereas isotopic decay rates are constant throughout Earth's history, it is likely that crustal composition changed over time as the craton evolved. The Acasta Gneiss Complex of the western Slave craton contains intact rocks as old as 4.03 Ga (Stern

Table 7. Crustal Comparisons

Study	*K2O (wt %)*	*Th (ppm)*	*U (ppm)*	*Heat Production (μW/m^3)*	*Sample*
Hasterok and Chapman (2011)	N/A	N/A	N/A	0.40	Terrane
Pollack and Chapman (1977)	N/A	N/A	N/A	0.25	Terrane
Rudnick and Fountain (1995)	0.6	1.2	0.2	0.18	Terrane
Weaver and Tamey (1984)	1.0	0.42	0.05	0.16	Terrane
Hacker et al. (2011)	1.5	5.6	0.7	0.70	Model
Shaw et al. (1986)	1.6	7.7	1.1	1.17*	Terrane
Taylor and McLennan (1995)	0.34	1.06	0.28	0.19	Model
Dupuy et al. (1979)	1.42	5.8	0.6	0.83*	Xenolith
Rudnick and Taylor (1987)	0.45	0.5	0.2	0.15*	Xenolith
Rudnick and Presper (1989)	0.79	1.6	0.4	0.40	Xenolith
Gao and Rudnick (2003)	0.61	1.2	0.2	0.19	Model
Huang et al. (2013)	-	-	-	0.17	Model
Enriched (This Study)	1.2	1.6	0.42	0.37	Xenolith
Mixed (This Study)	0.33	0.53	0.20	0.14	Xenolith
Depleted (This Study)	0.11	0.27	0.15	0.08	Xenolith

The three crustal models compared to those in Table 1 (modified from Rudnick, 1992). If not directly provided, heat production is calculated (*) using equation 2 with a density of 3200 kg/m^3 (Gao et al. 2003).

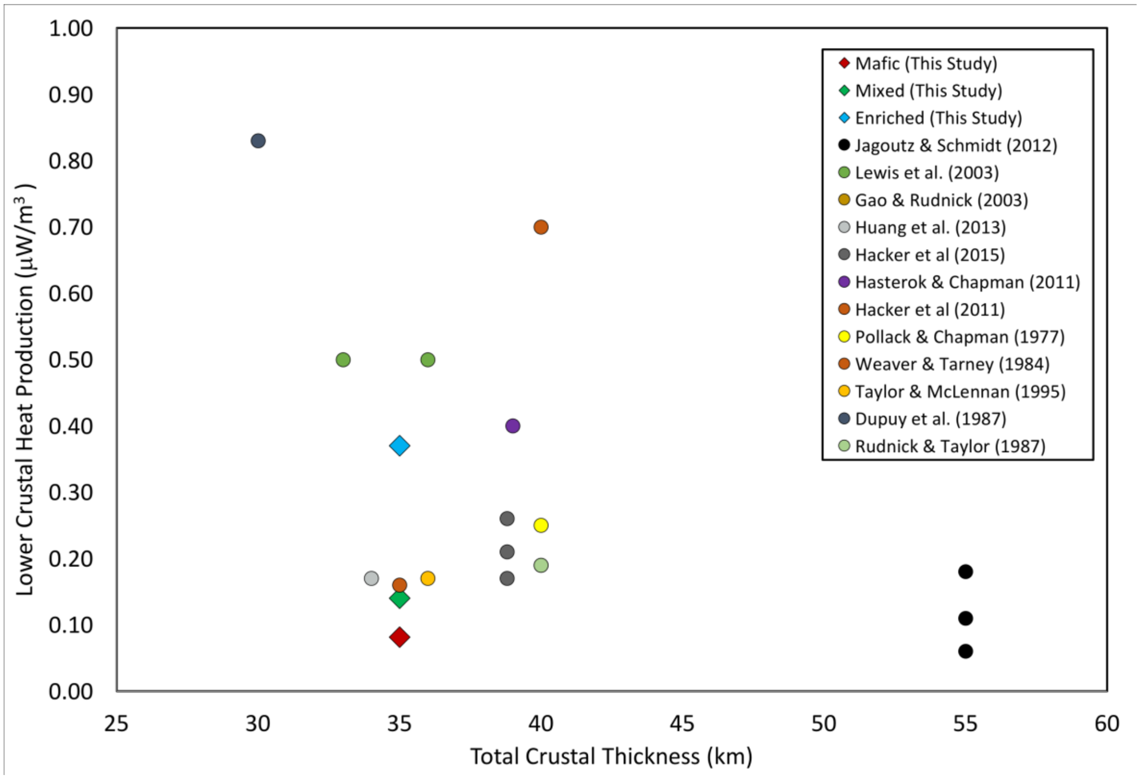

Figure 6. A compilation of the crusts calculated in this study (using the Diavik crustal thickness of Krauss et al., 2007). Generally, thick crusts (>45 km) or high heat production (> 0.50 µW/m^3) values correlate to volcanic arcs or active margins while moderate crustal thickness and lower heat production is more indicative a cratonic setting.

and Bleeker, 1998; Bowring and Williams, 1999; Reimink et al., 2014), which indicates some form of evolved crust was present at that time. The change in lower crustal heat production from present day to 3.0 Ga for the three estimates of lower crustal composition are presented in Figure 7. It is important to note, however, that the Slave craton underwent a major episode of granitic magmatism from 2.63-2.58 Ga (van Breeman et al., 1992), which likely resulted in significant migration of HPEs from the lower crust to the upper crust at that time. Thus, the HPE distributions assumed in the present are likely invalid prior to ~2.6 Ga.

As is shown in the figure 7, the heat production of all models is almost two to three times higher in the Archean than today. Clearly, both end-member estimates of Slave lower crustal heat production represent extremes and the mixed crustal composition likely is a more realistic indication of past heat production. The later sections will use the heat production from these compositions to calculate crustal parameters such as Moho temperature, heat flux, and the effects of varying crustal thickness and stratification that will test that validity of these heat production values and compare them to crustal variables calculated by others.

6.4 Historical Heat Flux

Utilizing the historical heat production values calculated in Section 6.3, the historical crustal heat flux can be calculated using Equation 4.

$$q_C = q_M + (A_{UC} * d_{UC}) + (A_{LC} * d_{LC}) \qquad \textbf{(4)}$$

This calculation is dependent on several assumptions: (1) that crustal thickness has remained constant through time; (2) that the relative proportions of typical upper and lower crustal lithologies has remained constant over time; (3) that mantle heat flux has remained constant over time. The parameter space of several of these variables is explored in Section 6.5. While likely not viable for the entirety of geologic time, the heat flux modeled through this method can act as a

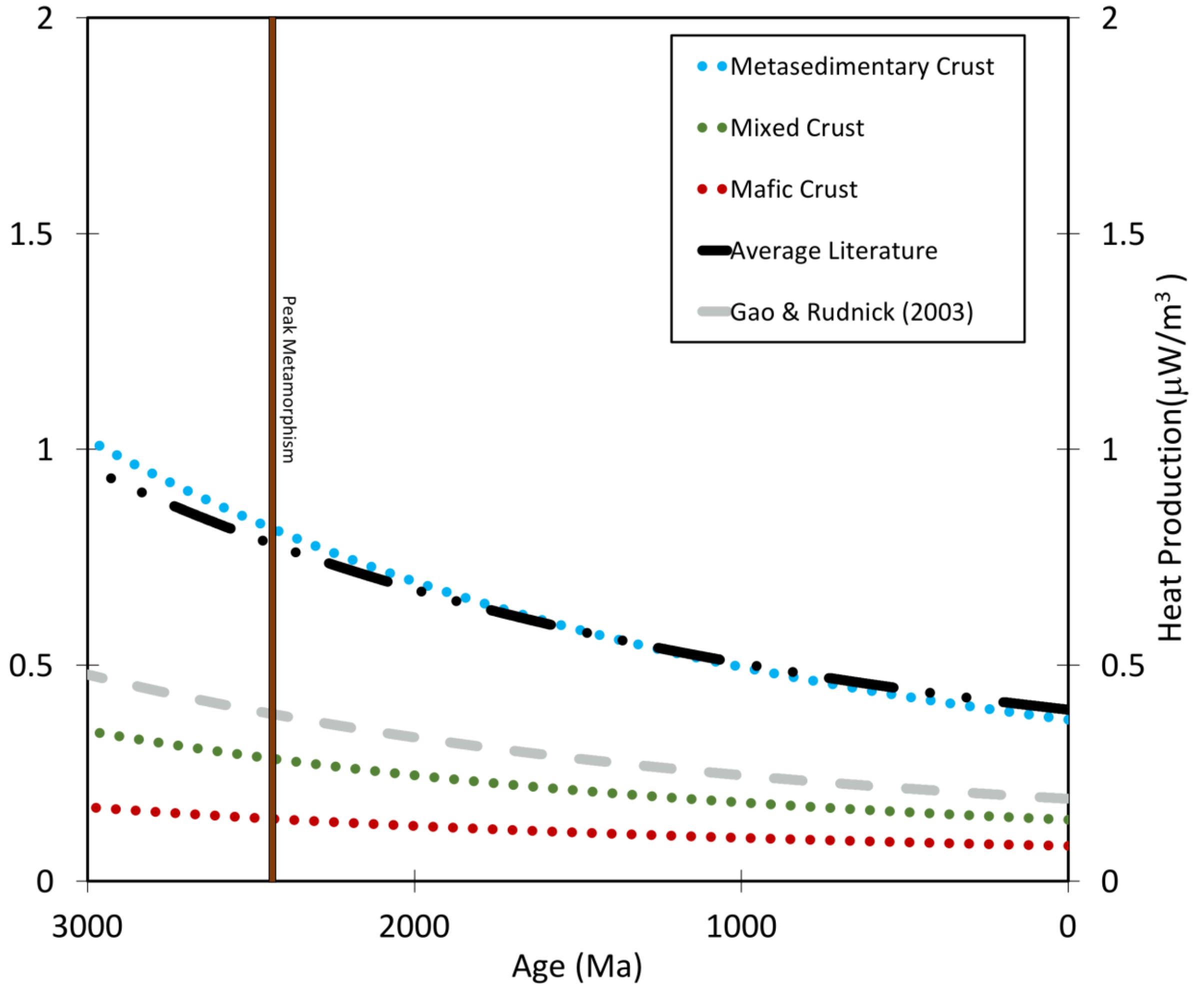

Figure 7. Change in lower crustal heat production over time for various lower crustal compositions. Metasedimentary, mafic, and, mixed lower crust (this study) and average literature heat production values for lower crust (Table 1). Steady state heat production is unlikely past 2.5-2.6 Ga (peak metamorphism in line with geochronology of Davis et al. 2003)

minimum bounding value, as variables such as mantle heat flux were likely higher the past than they are today.

Using the half-lives of the four major heat-producing isotopes, the heat production values are calculated back to 3.0 Ga to estimate past heat flux (section 5.3). Upper crustal heat production is calculated algebraically in the modern day utilizing the lower crustal heat production values calculated in this study in conjunction with crustal thickness estimates from Krauss et al. (2007) and the modern heat flow at Lac de Gras presented by Mareschal et al. (2004). It is important to note, however, that the upper crustal heat production calculated via this method is roughly 1.1 $\mu W/m^3$, a value that could represent mixing of middle crustal rocks with the 1.7 $\mu W/m^3$ upper crustal rock estimate of Thompson et al. (1995). The crust is calculated to have a constant thickness and stratification throughout geologic time though this is likely not the case before 2.5 Ga (Krauss et al., 2007; Lewis et al., 2003; van Breeman et al., 1992). Mantle heat flux is another variable included here: while it is treated as a constant for mathematical purposes, it is a value from the Phanerozoic (Russell et al., 2001) and is probably not the case at 3 Ga and therefore only allows for the calculated continental heat flux value to act as a minimum bound. Values utilized in Equation 4 are presented in Table 8.

Through the application of these heat flow calculations, Figure 8 shows that heat flow through the Slave craton was roughly 56 mW/m^2 at 2.5 Ga for both the mixed and depleted crusts while the metasedimentary crust was closer to 84 mW/m^2. This is likely an underestimate as this model utilizes a constant mantle heat flow corresponding to the Phanerozoic (Russell et al., 2001). The metasedimentary crust increases heat production at a much greater rate compared to the other two models, generally due to its relatively higher concentration of K. Along with this, utilizing the lower crustal heat production values from this study it can be shown that crustal heat production alone accounts for the heat flow at 2.5 Ga to be roughly 8 mW/m^2 to 38 mW/m^2 higher than

Table 8. Heat flux Calculations

Symbol	*Variable*	*Value*	*Units*	*Citation*
q_C	Continental Heat Flux	46	mW/m^2	Mareschal et al. (2004)
q_M	Mantle Heat Flux	15.1	mW/m^2	Russell et al. (2001)
d_{LC}	Lower Crust Thickness	10	km	Krauss et al. (2007)
d_{UC}	Upper Crust Thickness	25	km	Krauss et al. (2007)
A_{UC}	Upper Crust Heat Production	Calculated	μW/m^3	Calculated
A_{LC}	Lower Crust Heat Production	0.08-0.37	μW/m^3	This Study

The variables utilized in Equation 4 to calculate heat flux through time. Upper crustal heat production is calculated algebraically and is also extrapolated through geologic time. Continental heat flux starts at 46 mW/m^2 for the present day to calculate the upper crustal heat production and then the total heat flux is calculated through time.

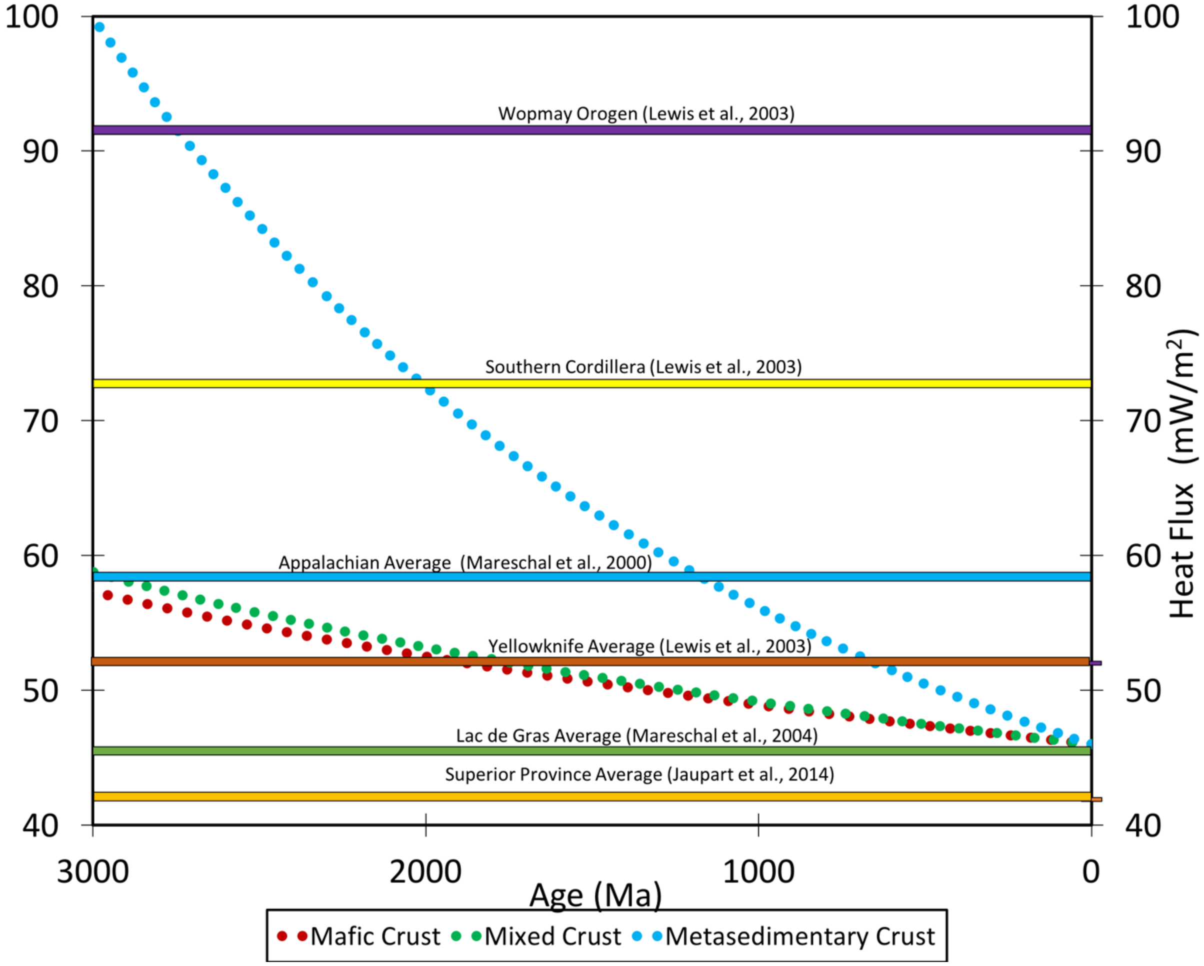

Figure 8. The continental heat flux of the Lac de Gras region calculated through time based on the heat production values shown in Figure 5. Modern day heat flow measurements are shown by horizontal bars. Sources of heat flow data are indicated next to their respective heat flow measurement lines.

present, depending on the model utilized. It is likely that the ancient heat production values calculated here are a result of utilizing an initial value that is generally much higher than those of other cratons, such as the 42 mW/m^2 Superior craton described in Jaupart et al. (2014); this is likely due to the relatively thick and enriched layer utilized to model the upper crust which is modelled to decay at the same rate as the lower crust. As such, it is important to note that a highly enriched upper crust is unlikely for the entirety of geologic time and Taylor and McLennan (1986) show in their Archean crustal models that the upper crust is most likely less differentiated than is presented here, indicating the upper crustal layer was has been enriched in HPEs sometime in the geologic past.

6.5 Heat Production and the Moho

6.5.1 In-Situ Moho temperatures

When combined with other crustal parameters including crustal thickness, mantle heat flow, and crustal heat flow, heat production data can be utilized to calculate the temperature at the Moho. This is shown in Equation 5 (modified from Kramers et al., 2001, with separate thermal conductivities for the upper and lower crust).

$$T_m = T_0 + d_{UC}\left[\frac{q_c-(q_M+(A_{LC}*d_{LC}))}{2K_{UC}} + \frac{\left(q_M+(A_{LC}*d_{LC})\right)}{K_{UC}}\right] + d_{LC}[\frac{(A_{LC}*d_{LC})}{2K_{LC}} + \frac{q_M}{K_{LC}}] \qquad \textbf{(5)}$$

Variables for Equation 5 are described in Table 9. Using the historical heat production values from section 5.3, Moho temperatures for each crustal model can be calculated through geologic time. Figure 9 shows the Moho temperature over time along with various geochronological markers representing events in the geologic past. Rutile ages of similar xenoliths from Lac de Gras kimberlites are presented in Davis (1997) and Förster et al. (2017). The rutile ages are much younger than the ages of the metamorphic zircons. The ages were interpreted by Davis (1997) and Förster et al. (2017) to represent the time at which lower crustal temperatures

Table 9. Moho Temperature Calculations

Symbol	*Variable*	*Value*	*Units*	*Reference*
T_0	Surface Temperature	273.15	K	Estimate
T_m	Moho Temperature	N/A	K	Calculated
q_C	Continental Heat Flux	46	mW/m^2	Mareschal et al. (2004)
q_M	Mantle Heat Flux	15.1	mW/m^2	Russell et al. (2001)
K_{LC}	Lower Crust Heat Conductivity	2000	mW/m*K	Merriman et al. (2013)
K_{UC}	Upper Crust Heat Conductivity	2250	mW/m*K	Merriman et al. (2013)
d_{UC}	Upper Crust Thickness	25	km	Krauss et al. (2007)
d_{LC}	Lower Crust Thickness	10	km	Krauss et al. (2007)
A_{LC}	Lower Crust Heat Production	0.08-0.37	μW/m^3	This Study

The variables utilized in equation 5 to calculate Moho temperature through time and the effects of varying crustal thickness and stratification.

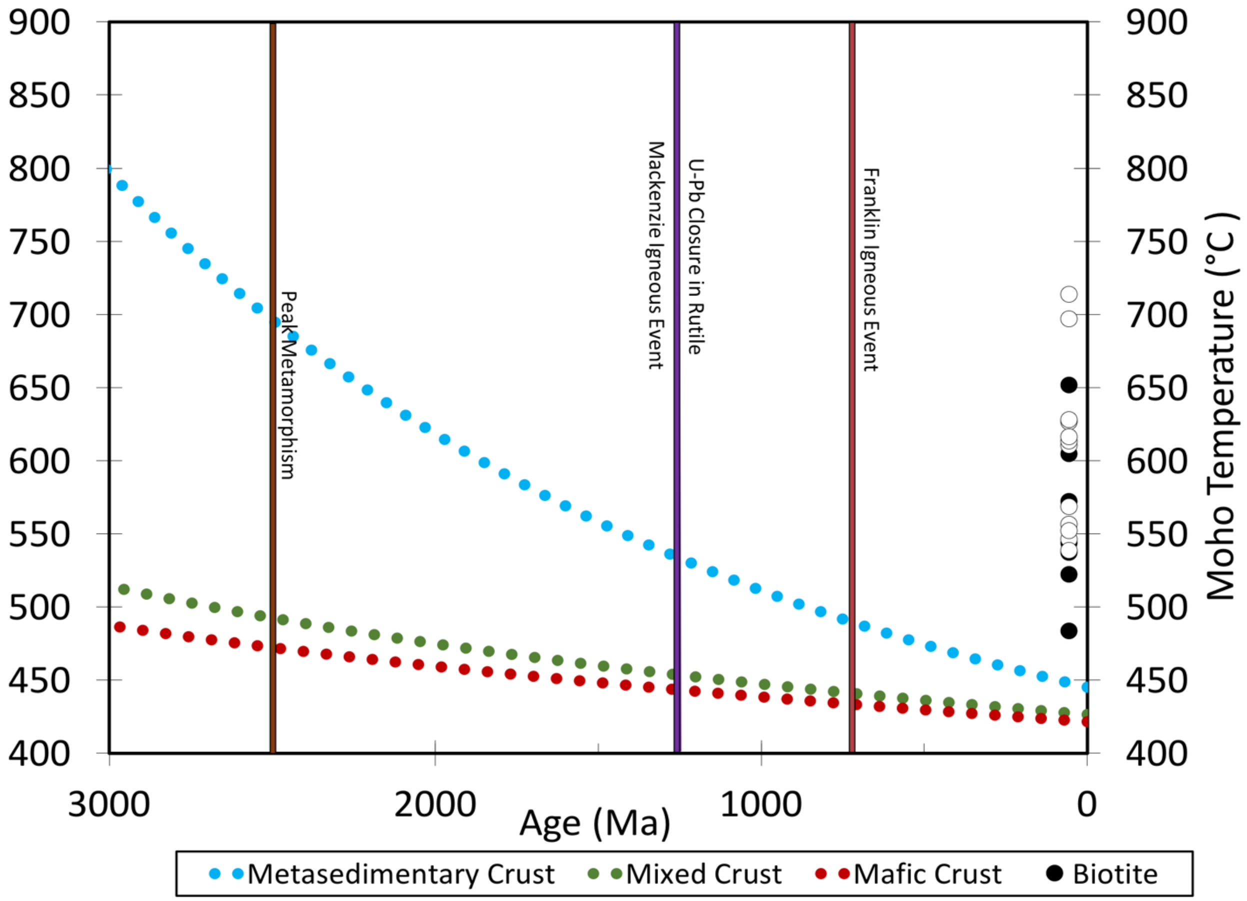

Figure 9. The change in Moho temperature calculated through time using heat production values calculated in Figure 5. The average garnet-biotite temperatures across the four calibrations presented in Figure are also plotted here to compare with the results of the model calculations. Open symbols represent touching relationships while closed symbols represent inclusions. The age of peak metamorphism corresponds to the dominant age of metamorphic zircon growth as reported by Davis et al. (2003) whereas rutile U-Pb age are from Förster et al. (2017). Ages of igneous events are from Heaman and LeCheminant, (1989) and Heaman et al. (1992).

dropped to below the blocking temperature of U-Pb exchange in rutile (calculated by Cherniak, 2000 to be roughly 550 °C), or, alternatively, related to possible reheating of the Slave craton lower crust during the Mackenzie igneous event at 1200 Ma (LeCheminant & Heaman, 1989). The modern-day Moho temperatures calculated using metasedimentary, mixed, and mafic lower crustal models and assuming a 25 km thick upper crust and 10 km thick lower crust are 445 °C, 426 °C, and 422 °C, respectively. It should be noted that these calculated Moho temperatures are strongly dependent on values chosen for the crustal thermal conductivity of each of the two crusts, which is temperature-dependent (Merriman et al., 2013). This model utilizes upper and lower crustal thermal conductivity values of 2250 mW/m*K and 2000 mW/m*K, respectively. These conductivity values are from Merriman et al. (2013), based on a tonalite-trondhjemite-granodiorite (TTG) composition upper crust and a mafic granulite composition lower crust at a temperature of ~225 °C, which is the middle of the range of temperatures expected for the crustal column.

Ambient temperature thermometry (Section 4.1) records lower crustal temperatures as low as ~ 500 °, indicating that portions of the lower crust have cooled to this temperature through time. As such, Figure 9 also presents the average garnet-biotite temperatures described in Chapter 4. These temperatures group universally above the Moho temperatures estimated from the range of heat production determined in this study at the time of kimberlite eruption (~ 55 Ma, Moser and Amelin, 1996; Graham et al., 1999; Sarkar et al., 2015). Along with this, Figure 10 updates Figure 4 with the Moho temperatures calculated from the heat production values and crustal architecture proposed here. In this figure, it is shown that all biotite-garnet temperatures plot above the calculated Moho temperatures regardless of the calibration utilized (though two high-F biotites are within 5 °C). This reinforces that the biotite-garnet geothermometer is only giving a maximum

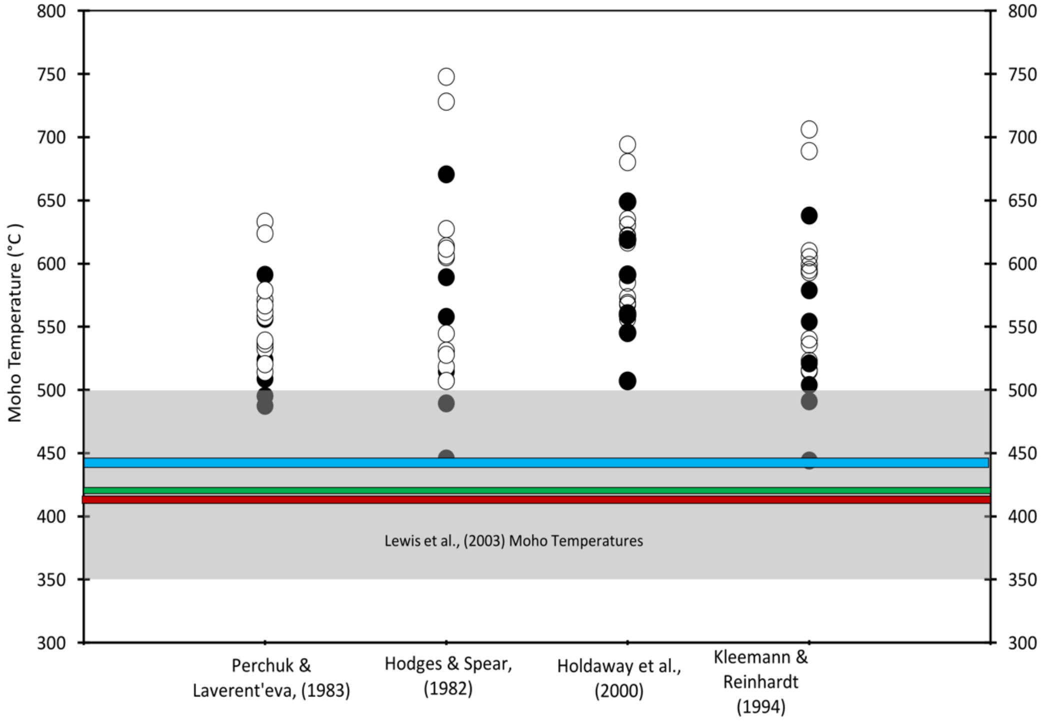

Figure 10. Modelled present-day Moho temperatures for the mafic (red), mixed (green), and metasedimentary (blue) crusts compared to the biotite from Figure 4. Open symbols again represent touching mineral relations while closed symbols are inclusions.

estimate of the Moho temperature at the time of kimberlite eruption and is likely only reporting the closure temperature of Fe^{2+}-Mg equilibration.

6.5.2 The Differentiation Index

The differentiation index (DI) is a measure of the degree of crustal stratification in HPEs (Perry et al., 2006; Jaupart et al., 2016). Specifically, the DI is the ratio of average surface heat production relative to the heat production of the bulk crust. A DI of 1 represents a homogeneous crust with respect to HPE distribution whereas a DI > 1 reflects a stratified crust with HPE concentrated near the surface. The value of the DI can have a significant effect on Moho temperatures (Perry et al., 2006; Jaupart et al., 2016).

To understand how the three lower crustal models of the present study relate to crusts with similar thickness but different stratifications, the DI is calculated as a function of crustal thickness (Figure 11). This is accomplished through utilizing a weighted average crustal thickness and rock density and highlights the various effects of different crustal stratifications as a function of crustal thickness. Upper crustal heat production is held at a constant 1.7 $\mu W/m^3$ (Thompson et al., 1995) in order to facilitate comparison between the three lower crustal models (i.e., unlike in Fig. 10, upper crustal heat production is not calculated from heat flow, crustal thickness, and lower crustal heat production). This model closely follows the model described by Jaupart et al. (2016) in which a lower degree of crustal differentiation (DI closer to 1) generally relates to a greater contribution of the crust to Moho temperatures.

6.5.3 Crustal Thickness and Stratification

Crustal thickness and stratification have a large effect on Moho temperatures. By utilizing Equation 5, the effects of thickened crust or highly-stratified crust can be investigated in conjunction with the three proposed heat production values. Figure 12 shows the variation in

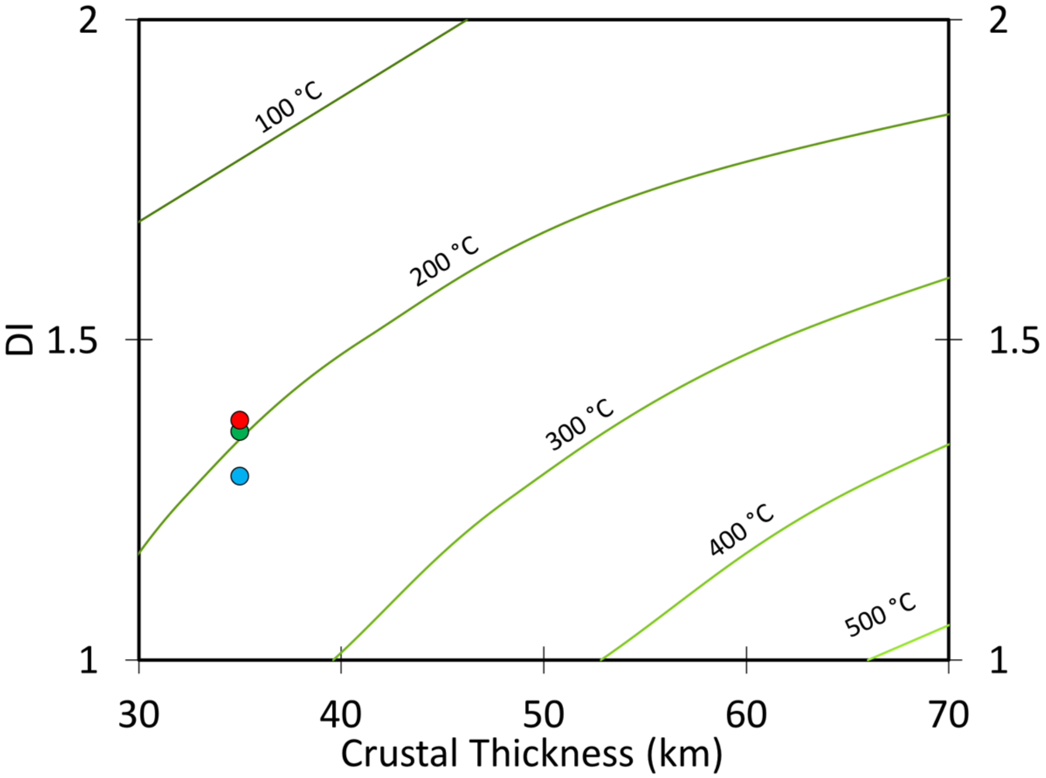

Figure 11. The effect of crustal thickness and differentiation index (DI) on Moho temperatures, where DI is a measure of the stratification of heat-producing elements in the crust (see text). The thermal density of the crust is modelled as a weighted average distributed between the upper and lower crust. Thermal conductivity is a single weighted average between the two crusts based on crustal thickness.

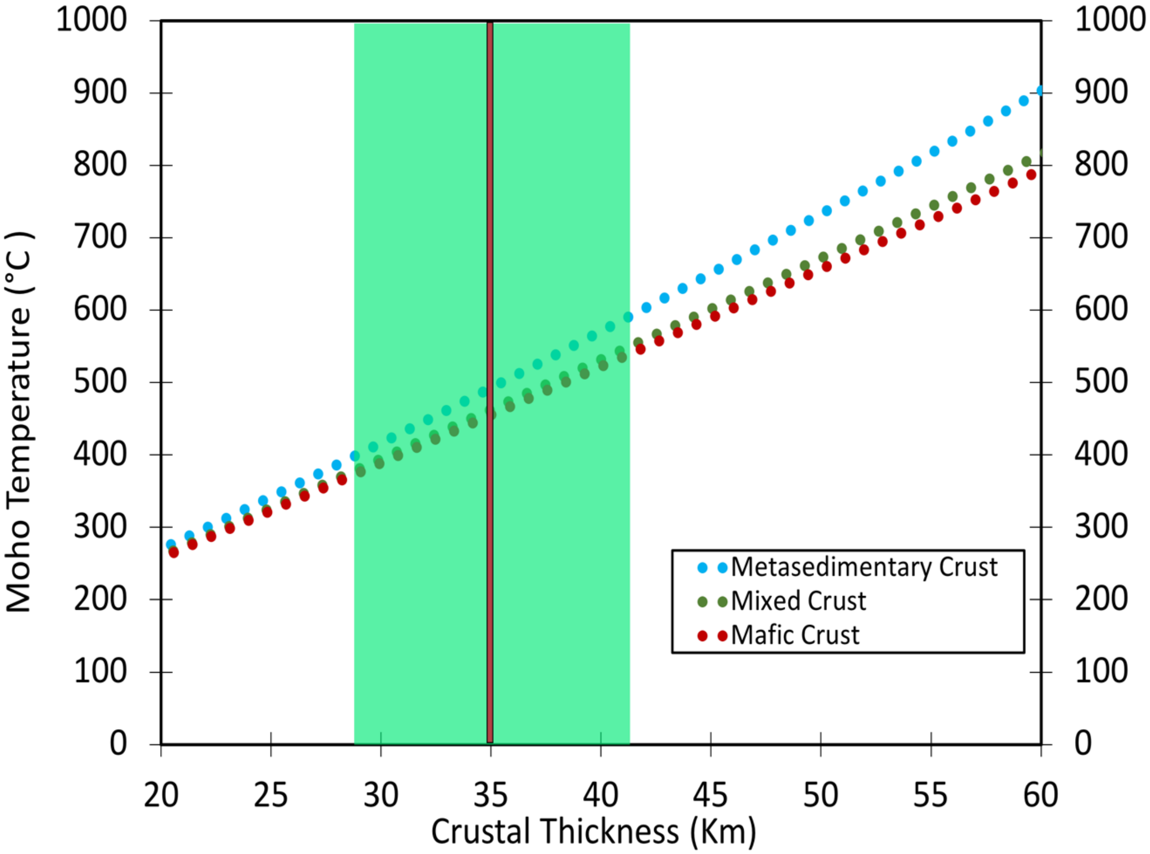

Figure 12. The variation of Moho temperature with crustal thickness calculated utilizing the three lower crust heat production models and assuming a constant upper crust:lower crust ratio of 5:2. The green section is a range of potential crustal thicknesses from the geobarometry of Krauss et al. (2007) and the red line indicates the value utilized for section 6.5.1. (see text).

calculated Moho temperatures as a function of crustal thickness. In this calculation the crustal stratification is held constant, and follows the structure suggested from geobarometry estimates on these xenoliths from Krauss et al. (2007), wherein the lower crust is inferred to be 40% as thick as the upper crust. The values from Table 9 and the back-calculated upper crustal heat production are utilized in this model. At a total crustal thickness of 20 km, the difference in Moho temperatures between the three heat production values is only ~ 15 °C; however, this change is amplified as crustal thickness increases. This is due to the size of the lower crustal layer, or the "difference" between each crustal model increasing with each incremental increase in crustal thickness and giving the crust a higher contribution to the Moho heat flux. The Moho temperatures calculated from the depleted lower and mixed lower crustal models are virtually unresolvable, even at crustal thicknesses of greater than 50 km. Even the enriched lower crust model does not produce a markedly higher (> 50 °C) Moho temperatures except when crustal thickness exceeds 50 km.

The proportion of upper crust to lower crust in a crustal column also has an effect on Moho temperatures due to their different concentrations of HPEs. Assuming a constant crustal thickness of 35 km, the effects of changing crustal stratification (the ratio between upper and lower crustal thickness) can be explored with Equation 5. Figure 13 shows that increasing the upper crust:lower crust thickness ratio from 0 to 5 results in a pronounced increase in Moho temperatures but further increases in this ratio have relatively little effect on Moho temperatures. The actual value of upper to lower crust ratio in the Slave craton can be reasonably well-constrained through a combination of surface geological observations and xenolith data. The deepest crustal levels exposed at surface in the craton are the granulite-facies rocks of the Ghost domain (Pehrsson et al., 2000; Bennett et al., 2005), which record Neoarchean paleopressures of 6-7 kilobars (~ 21 to 25 km depth). Upper crustal rocks tend to be more felsic to intermediate dominant in the Ghost domain, whereas mafic

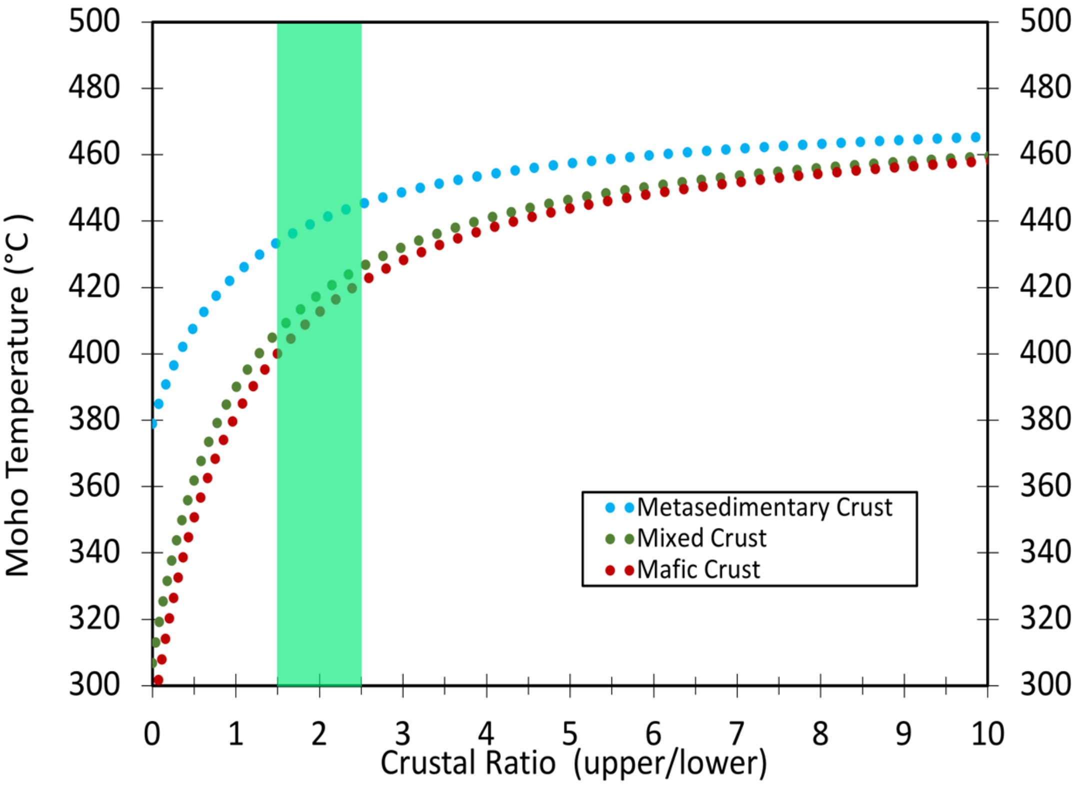

Figure 13. The variation in Moho temperatures as it relates to different upper crust:lower crust thickness ratios assuming a 35 km thick total crust. The green band corresponds to upper crust:lower crust ratios identified through Slave craton geology (see text).

rocks are subordinate. In contrast, the Diavik lower crustal xenolith suite records Neoarchean paleopressures of 10 ± 2 kilobars (~ 28 to 42 km depth) and is predominately mafic (Krauss et al., 2007). These observations suggest that the transition from upper to lower crustal lithologies occurs between 25 and 28 km depth, which corresponds to upper crust:lower crust thickness ratios between ~1.5 and 2.5 assuming total crustal thicknesses between 35 and 42 km.

6.6 Lithospheric Geotherms

Radiogenic heat production in both the crust and the mantle are primary variables in calculated lithospheric geotherms (Hasterok and Chapman, 2011). This is of interest as the A-154 kimberlite is a currently operational diamond mine. Thus, having a well-constrained mantle geotherm is crucial for understanding the size of the diamond window in the lithospheric mantle that was sampled by this kimberlite and also for determining whether indicator mineral temperatures obtained for nearby kimberlites reflect derivation from within or outside the diamond window. To investigate the potential of these lower crust heat production measurements to influence calculated lithospheric geotherms, the heat production values measured here are used as input for the geotherm modeling program FITPLOT (Mather et al., 2011). This program creates xenolith-based geotherms using pressure-temperature (P-T) estimates from mantle xenolith-derived thermobarometric data and includes various other crustal and mantle input parameters.

To construct a geotherm, the present study utilizes P-T data from central Slave Craton kimberlites and crustal input parameters from the A-154 kimberlite pipe in which the studied lower crustal xenoliths were erupted. The central Slave craton mantle P-T array is compiled in Grütter and Moore (2003) and references therein. Unfortunately, the data available to constrain the central Slave P-T array are relatively sparse, which translates to a large uncertainty envelope associated with its modeled lithospheric geotherm (Fig. 14). As such, a second geotherm was also constructed, that utilizes the lower crustal heat production values of the present study and the mantle P-T array derived for the Murowa kimberlite of southern Africa (Pearson et al., 2018) to independently test the effects of varying heat production parameters. The Murowa mantle P-T array is better defined than the central Slave array, which allows the effects of changing lower crustal heat production on the geotherm to be separated from effects of geotherm dispersion associated with scatter in the mantle P-T array. It also potentially allows for a less-biased test of how heat production in the lower crust affects mantle geotherms when propagated to depth. Table 10 shows the various input parameters for both the Murowa and central Slave geotherms, along with the FITPLOT calculated Moho temperatures and lithospheric depth.

For each of the two localities, Figure 14 presents three model lithospheric geotherms derived using the depleted, enriched and mixed lower crustal heat production values generated in the present study. In both the Murowa and central Slave cases, it is apparent that varying lower crustal heat production input values in the FITPLOT program causes only small changes in Moho temperature (35 to 50 °C), in-line with the steady-state crustal geotherm calculations presented above. Surprisingly, the FITPLOT program predicts that increasing heat production in the lower crust results in slightly lower modelled temperatures in the deep lithosphere and, in turn, a small (~ 10 km) increase in the calculated lithospheric thickness. This counterintuitive result appears to be an artefact of the FITPLOT program, which regresses the mantle geotherm to the P-T array. As such, a higher Moho temperature forces the program to fit a steeper-sloped line to the mantle P-T array, which results in lower temperatures in the deep lithosphere when the geotherm is extrapolated to depths below the constraining mantle P-T data. A higher Moho temperature should result in a thinner lithosphere with all other variables held constant.

Table 10. Geotherm Modelling Parameters and Results

	Input						*Output*	
Geotherm	*UC HP* (μW/m^3)	*UC (km)*	*LC HP* (μW/m)	*LC (km)*	*Total Crust (km)*	*Tp* (°C)	*Moho T* (°C)	*Lithospheric Depth (km)*
Murowa Enriched	1.12	20	0.37	20	40	1300	452	167
Murowa Mixed	1.12	20	0.14	20	40	1300	419	162
Murowa Depleted	1.12	20	0.08	20	40	1300	410	161
Diavik Enriched	1.7	25	0.37	10	35	1300	455	194
Diavik Mixed	1.7	25	0.14	10	35	1300	434	192
Diavik Depleted	1.7	25	0.08	10	35	1300	430	191

The crustal input parameters utilized in FITPLOT. Values are from Pearson et al. (2018) and citations within. Moho temperatures are output as calculated values from the FITPLOT program. Geotherms are calculated using lower crustal heat production models from this study. Murowa crustal thickness is of Gore et al. (2009) and Diavik upper crustal heat production is of Thompson et al. (1995).

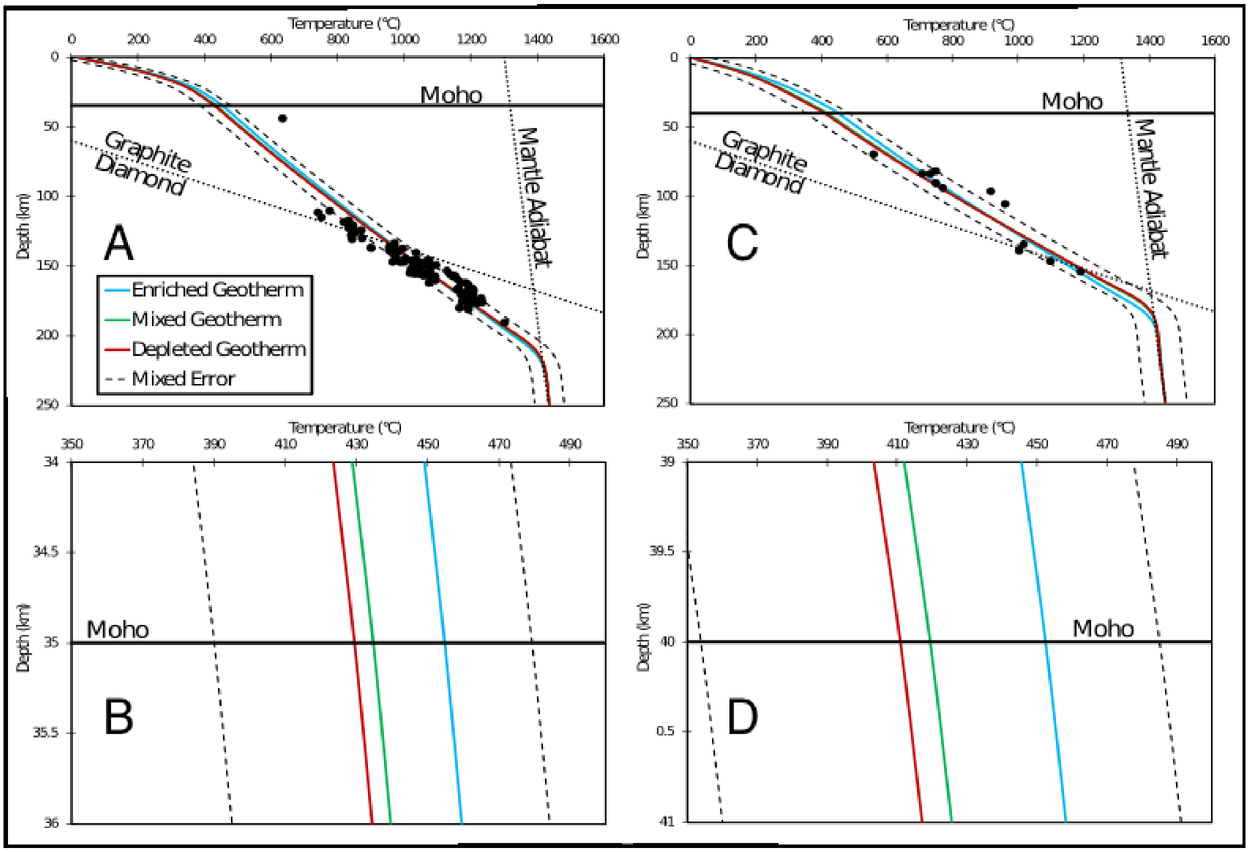

Figure 14. FITPLOT modeling (Mather et al., 2011) of the Murowa (C and D) and central Slave (A and B) mantle P-T data arrays using the depleted, enriched and mixed lower crustal heat production values of the present study. Graphite-Diamond line is that of Kennedy and Kennedy (1976). Note that the exact Moho temperature has relatively little effect on the calculated mantle geotherm and in turn the predicted size of the diamond window and lithospheric thickness.

From this evaluation, using the model approaches adopted here and the assumptions implicit within them, varying the lower crustal heat production normally does not propagate to large uncertainties in the size of the "diamond window" or modelled lithospheric thickness for most mantle xenolith datasets. Generally, calculated lithospheric thickness varies by only ~ 10 km with the expected range of lower crustal heat production values. Moho temperature is affected to a higher degree (35 to 50 °C) by changing values of lower crustal heat production but geotherms in FITPLOT will tend to conform to the mantle P-T array regardless of the Moho temperature. Adjusting lower crustal heat production values can improve the fit of the geotherm by calculating a Moho temperature that better fits the P-T array; however this is highly dependent on the array having a good linear character that regresses back to a realistic Moho temperature in accordance with the crustal parameters. Currently, having well-constrained lower crustal heat production values can reduce uncertainty in geotherms with ideal P-T arrays but is unlikely to have a major influence on predictions of the diamond prospectivity of a specific kimberlite pipe.

Chapter 7: Summary and Conclusions

The cratonic lower crust is lithologically diverse, making the development of a comprehensive heat-production model challenging. Through the application of mineral thermometry, heat-producing-element concentration determinations, and modal abundance estimates, this project attempts to constrain the thermal structure of the Slave craton lower crust and the impact of that thermal structure on the underlying lithospheric mantle.

The lower crustal xenolith suite from the Diavik A-154 kimberlite comprises dominantly two rock types, mafic granulite and metasedimentary ("enriched") granulite in approximately 80:20 proportions. Direct measurement of the heat-producing element concentrations of the constituent minerals of these two rock types yields a weighted average radiogenic heat production value for the lower crust of 0.14 ± 0.02 μW/m^3, which is lower than some other estimates of lower crustal heat production worldwide (e.g., Hacker et al, 2011) but generally comparable to global estimates of lower crustal composition (e.g., Gao and Rudnick, 2003; Huang et al, 2013). Combining this lower crustal heat-production value with previously measured surface heat flow in the Diavik area (Mareschal et al., 2004) and constraints on the lower crust thickness of the Slave craton results in a calculated Moho temperature beneath the Diavik diamond mine of ~ 425 °C (at 35 km depth, utilizing the "mixed" crustal estimate), 50 °C lower than that estimated by Russell et al. (2001). This modeled Moho temperature can be compared to direct mineralogical temperature estimates for the Diavik xenoliths derived from garnet-amphibole and garnet-biotite mineral pairs that have undergone extensive Fe^{2+}-Mg re-equilibration during cooling from peak metamorphic temperatures. These Fe^{2+}-Mg exchange geothermometers yield re-equilibrated temperatures as low as 471 °C. These mineralogical temperature estimates should be taken as an upper bound on present-day temperatures in the Slave craton lower crust as the recorded temperatures may either reflect an ancient ambient temperature of the lower crust or the cessation of Fe-Mg re-equilibration between the minerals at some temperature above the ambient temperature. In both cases, these estimates are maximum estimates of the lower crustal temperature today. Thus, the mineralogical temperature estimates derived from the xenoliths are consistent with the modeled Moho temperature of ~ 425 °C.

Using heat production values calculated in this study, several conclusions can be drawn about the thermal structure of Slave cratonic crust. Back-calculating crustal radiogenic heat production to 2.5 Ga results in a Moho temperature hundred degrees higher compared to 425 °C in the present day. This result indicates that in-situ lower crustal heat production cannot be completely responsible for the > 800 °C peak metamorphic temperatures recorded in the lower crustal xenoliths samples (Davis et al., 2003; Krauss et al., 2007). Surface heat flow in the Lac de Gras region of the Slave Craton is calculated to have been 55 mW/m^2 to 85 mW/m^2 at 2.5 Ga. This compares to values measured today of 46 mW/m^2 (Mareshal et al., 2004) indicating significant cooling of the lithosphere in the timeframe.

The surface heat flow of the Slave Craton is high in comparison to other cratonic regions, as reported by Mareschal et al. (2004) and this study supports their proposal that this is linked to a relatively thick and HPE enriched upper crustal layer and a thin mafic lower crust. Finally, while having a subtle effect on Moho temperatures when modelling lithospheric geotherms, depending on the approach taken, estimated lower crustal heat production values are unlikely to have a major effect on the predicted size of the diamond window or lithospheric thickness.

References

Aulbach, S., Griffin, W. L., Pearson, N. J., O'Reilly, S. Y., & Doyle, B. J. (2007). Lithosphere formation in the central Slave Craton (Canada): plume subcretion or lithosphere accretion? *Contributions to Mineralogy and Petrology, 154*, 409-427.

Bennett, V., Jackson, V. A., Rivers, T., Relf, C., Horan, P., & Tubrett, M. (2005). Geology and U–Pb geochronology of the Neoarchean Snare River terrane: tracking evolving tectonic regimes and crustal growth mechanisms. *Canadian Journal of Earth Science, 42*, 895-934.

Bleeker, W., & Hall, B. (2007). The Slave craton: geological and metallogenic evolution. *Geological Association of Canada, Mineral Deposits Division, Special Publication*(5), 849-879.

Borinski, S. A., Hoppe, U., Chakraborty, S., Ganguly, J., & Bhowmik, S. K. (2012). Multicomponent diffusion in garnets I: general theoretical considerations and experimental data for Fe–Mg systems. *Contributions to Mineralogy and Petrology, 164*, 571-586.

Bowring, S. A., & Williams, I. S. (1999). Priscoan (4.00–4.03 Ga) orthogneisses from northwestern Canada. *Contributions to Mineralogy and Petrology, 134*(1), 3-16.

Bucher , K., & Frey, M. (2002). Metamorphism of Pelitic Rocks (Metapelites). In *Petrogenesis of Metamorphic Rocks* (pp. 217-258). Springer.

Chapman, D. S., & Pollack, H. N. (1977). Regional geotherms and lithospheric thickness. *Geology, 5*(5), 265.

Cherniak, D. J. (2000). Pb diffusion in rutile. *Contribuations to Mineralogy Petrology, 139*, 198-207.

Condie, K. C., Latysh, N., Van Schmus, W. R., Kozuch, M., & Selverstone, J. (1999). Geochemistry, Nd and Sr isotopes, and UrPb Zircon ages of Granitoid and Metasedimentary Xenoliths from the Navajo Volcanic Field, Four Corners area, Southwestern United States. *Chemical Geology, 156*, 95-133.

Creaser, R. A., Grütter, H., Carlson, J. A., & Crawford, B. (2003). Mac- rocrystal phlogopite Rb – Sr dates for the Ekati property kimber- lites, Slave Province, Canada: evidence for multiple intrusive episodes in the Paleocene and Eocene. *Proceedings of the 8th International Kimberlite Conference*, (p. 61). Victoria, B.C.

Czas, J., Stachel, T., Peason, D. G., Stern, R. A., & Read, G. H. (2018, December). Diamond brecciation and annealing accompanying major metasomatism in eclogite xenoliths from the Sask Craton, Canada. *Mineralogy and Petrology, 112*(Supplement 1), 311-323.

Davis, W. J. (1997, April). U-Pb zircon and rutile ages from granulite xenoliths in the Slave province: Evidence for mafic magmatism in the lower crust coincident with Proterozoic dike swarms. *Geology, 24*, 343-346.

Davis, W., Canil, D., MacKenzie, J. M., & Carbno, G. B. (2003). Petrology and U-Pb geochronology of lower crustal xenoliths and the development of a craton, Slave Province, Canada. *Lithos*(71), 541-573.

Donovan, J. J., Kremser, D., Fournelle, J. H., & Goemann, K. (2015). *Probe for EPMA: Acquisition, Automation and Analysis. Probe Software, Inc* (Vol. 11). Eugene, Oregon.

Dupuy, C., Leyreloup, A., & Vernieres, J. (401-415). The lower crust of the Massif Central (Bournac, France)-with special references to REE, U and Th composition, evolution, heat-flow production. In L. H. Ahrens, *Origin and Distribution of the Elements.* Oxford: Pergamon Press.

Ferry, J. M., & Spear, F. S. (1978). Experimental calibration of the partitioning of Fe and Mg between biotite and garnet. *Contributions to Mineralogy and Petrology, 66*, 113-117.

Förster, B., Aulbach, S., Symes, C., Gerdes, A., Hofer, H. E., & Chacko, T. (2017). A Reconnaissance Study of Ti-minerals in Cratonic Granulite Xenoliths and their Potential as Recorders of Lower Crust Formation and Evolution. *Journal of Petrology, 58*(10), 2007-2034.

Frost, B. R., & Chacko, T. (1989). The Granulite Uncertainty Principle: Limitations on Thermobarometry in Granulites. *The Journal of Geology, 97*(4), 435-450.

Gao, S., & Rudnick, R. L. (2003). Composition of the Continental Crust. In R. Rudnick, D. Heinrich, & K. Turekian, *Treatise on Geochemistry* (Vol. 3). Elsevier.

Gao, S., Hern, H., Liu, Y.-S., Jin, S.-Y., Popp, T., Jin, Z.-M., . . . Zhao, Z.-B. (2000). Measured and calculated seismic velocities and densities for granulitesf rom xenolitho ccurrencesa nd adjacente xposed lower crustal sections: A comparative study from the North China craton. *Journal of Geophysical Research, 105*(B8), 18965-18976.

Ghent, E. D., & Stout, M. Z. (1986). Garnet-Hornblende Thermometry, CaMgSi2O56 Activity, and the Minimum Pressure Limits of Metamorphism for Garnet Amphibolites. *Geology, 94*(5), 736-743.

Gore, J. J., O'Reilly, S. Y., & Ryan, C. G. (2009). Crustal Structure of the Zimbabwe Craton and the Limpopo Belt of Southern Africa: New Constraints from Seismic Data and Implications for it Evolution. *South African Journal of Geology, 112*(3-4), 213-228.

Gottlieb, P., Wilkie, G., Sutherland, D., Ho-Tun, E., Suthers, S., Perera, K., . . . Rayner, J. (2000). Using quantitative electron microscopt for process mineralogy applications. *Journal of the Minerals, Metals and Materials Society, 52*(4), 24-25.

Graham, I., Burgess, J. L., Bryan, D., Ravenscroft, P. J., Thomas, E., Doyle, B. J., . . . Armstrong, K. A. (1999). Exploration history and geology of the Diavik kimberlites. Lac de Gras Northwest Territories, Canada. *Seventh International Kimberlite Conference*, (pp. 262-279). Cape Town.

Grütter, H., & Moore, R. (2003). Pyroxene Geotherms Revisted - An Emperical Approach Based on Canadian Xenoliths. *8th International Kimberlite Conference Extended Abstract*.

Hacker, B. R., Kelemen, P. B., & Behn, M. D. (2011). Differentiation of the continental crust by relamination. *Earth and Planetary Science Letters, 307*, 501-516.

Harlov, D. E. (2012). The potential role of fluids during regional granulite- facies dehydration in the lower crust. *Geoscience Frontiers, 3*(6), 813-827.

Hasterok, D., & Chapman, D. S. (2011, July). Heat Production and Geotherms for the Continental Lithosphere. *Earth and Planetary Science Letters, 307*(1-2), 59-70.

Heaman, L. M., & Pearson, D. G. (2010). Nature and evolution of the Slave Province subcontinental lithospheric mantle. *Canadian Journal of Earth Sciences, 47*, 369-388.

Heaman, L. M., Kjarsgaard, B. A., & Creaser, R. A. (2003). The timing of kimberlite magmatism in North America: implications for global kimberlite genesis and diamond exploration. *Lithos, 71*, 153-184.

Heaman, L. M., LeCheminant, A. N., & Rainbird, R. H. (1992). Nature and timing of Franklin igneous events, Canada: Implications for a Late Proterozoic mantle plume and the break-up of Laurentia. *Earth and Planetary Science Letters, 109*, 117-131.

Helmstaedt, H. (2009). Crust–mantle coupling revisited: The Archean Slave craton, NWT, Canada. *Lithos, 112*, 1055-1068.

Hodges, K., & Spear, F. S. (1982). Geothermometry, geobarometry and the Al2SiO5 triple point at Mt. Moosilauke, New Hampshire. *American Mineralogist, 67*(11-12), 1118-1134.

Holdaway, M. J., Mukhopadhyay, B., Dyar, M. D., Guidotti, C. V., & Dutrow, B. L. (1997). Garnet-biotite geothermometry revised: New Margules parameters and a natural specimen data set from Maine. *American Mineralogist, 82*, 582–595.

Huang, Y., Chubakov, V., Fabio, M., Rudnick, R. L., & McDonough, W. F. (2013). A reference Earth model for the heat-producing elements and associated geoneutrino flux. *Geochemistry, Geophysics, Geosystems, 14*(6), 2004-2029.

Indares, A., & Martignole, J. (1985). Biotite-Garnet Geothermometry in Granulite-Facies Rocks: Evaluation of Equilibrium Criteria. *Canadian Mineralogist, 23*, 187-193.

Jagoutz, O., & Schmidt, M. W. (2012). The formation and bulk composition of modern juvenile continental crust: The Kohistan arc. *Chemical Geology*(298-299), 79-96.

Jaupart, C., Mareschal, J. C., Bouquerel, H., & Phaneuf, C. (2014). The building and stabilization of an Archean Craton in the Superior Province, Canada, from a heat flow perspective. *Journal of Geophysical Research: Soild Earth, 119*, 1-26.

Jaupart, C., Mareschal, J.-C., & Iarotsky, L. (2016, July). Radiogenic heat production in the continental crust. *Lithos, 262*, 398-427.

Johnson, D. M., Hooper, P. R., & Conrey, R. M. (1999). XRF Analysis of Rocks and Minerals for Major and Trace Elements on a Single Low Dilution Li-tetraborate Fused Bead. *CPDS-International Centre for Diffraction Data* , 843-867.

Kennedy, C. S., & Kennedy, G. C. (1976). The equilibrium boundary between graphite and diamond. *Journal of Geophysical Research, 81*, 2467–2470.

Kleemann, U., & Reinhardt, J. (1994). Garnet-biotite thermometry revisited: The effect of A1VI and Ti in biotite. *European Journal of Mineralogy, 6*, 925-941.

Koreshkova, M. Y., Downes, H., Levsky, L. K., & Vladykin, N. V. (2011). Petrology and Geochemistry of Granulite Xenoliths from Udachnaya and Komsomolskaya Kimberlite Pipes, Siberia. *Journal of Petrology, 52*(10), 1857-1885.

Kramers, J. D., Kreissig, K., & Jones, M. Q. (2001). Crustal heat production and style of metamorphism: a comparison between two Archean high grade provinces in the Limpopo Belt, southern Africa. *Precambrian Research, 112*, 149-163.

Krauss, C., Chacko, T., & Heaman, L. M. (2007). Petrological and chronological investigation of lower crustal xenoliths from the Diavik diamond mine, Slave Craton, NT, Canada. *Geological Association of Canada–Mineralogical Association of Canada Annual Meeting*, *32.*

Kretz, R. (1983). Symbols for Rock-Forming Minerals. *American Mineralogist, 68*, 277-279.

LeCheminant, A. N., & Heaman, L. M. (1989). Mackenzie igneous events, Canada: Middle Proterozoic hotspot magmatism associated with ocean opening. *Earth and Planetary Science Letters, 96*, 38-48.

Lewis, T. J., Hyndman, R. D., & Fluck, P. (2003). Heat flow, heat generation, and crustal temperatures in the northern Canadian Cordillera: Thermal control of tectonics. *Journal of Geophysical Research, 108*(B6), 2316.

Loomis, T. P. (1983). *Compositional zoning of crystals: A record of growth and reaction history.* New York: Springer-Verlag.

Mareschal, J. C., Jaupart, C., Gariépy, C., Cheng, L. Z., Guillou-Frottier, L., Bienfait, G., & Lapointe, R. (2000). Heat flow and deep thermal structure near the southeastern edge of the Canadian Shield. *Canadian Journal of Earth Sciences, 37*(2-3), 399-414.

Mareschal, J. C., Nyblade, A., Perry, H. C., Jaupart, C., & Bienfait, G. (2004). Heat flow and deep lithospheric thermal structure at Lac de Gras, Slave Province, Canada. *Geophysical Research Letters, 31*.

Mather, K. A., Pearson , D. G., Mckenzie, D., Kjarsgaard, B. A., & Priestley, K. (2011). Constraints on the depth and thermal history of cratonic lithosphere from peridotite xenoliths, xenocrysts, and seismology. *Lithos, 125*, 729-742.

Merriman, J. D., Li, A. G., Hofmeister, A. M., Nabelek, P. I., & Benn, K. (2013). Thermal transport properties of major Archean rock types to high temperature and implications for cratonic geotherms. *Precambrian Research, 233*, 358-372.

Moser, D., & Amelin, Y. (1-7). *Report on Rb-Sr dating of Alberta Kimberlites.* Kennecott Internal Report.

Müller, T., Dohmen, R., Becker, H. W., ter Heege, J. H., & Chakraborty, S. (2013). Fe–Mg interdiffusion rates in clinopyroxene: experimental data and implications for Fe–Mg exchange geothermometers. *Contributions to Mineralogy and Petrology, 166*, 1563-1576.

Pattison, D. R. (2003). Petrogenetic significance of orthopyroxene-free garnet+clinopyroxene+plagioclase-bearing metabasites with respect to the amphibolite and granulite facies. *Journal of Metamorphic Geology, 21*, 21-34.

Pearson, D. G., Liu, J., Smith, C. B., Mather, K. A., Kreb, M. Y., Bulanova, G. P., & Kobussen, A. (2018). Characteristics and Origin of the Mantle Root Beneath the Murowa Diamond Mine: Implications for Craton and Diamond Formation. In *Geoscience and Exploration of the Argyle, Bunder, Diavik, and Murowa Diamond Deposits* (pp. 403-424). SOCIETY OF ECONOMIC GEOLOGISTS.

Pehrsson, S. J., Chacko, T., Pilkington, M., Villeneuve, M. E., & Bethune, K. (2000). Anton terrane revisited: Late Archean exhumation of a moderate- pressure granulite terrane in the western Slave Province. *Geology, 28*(12), 1075-1078.

Perchuk, L. L., & Aranovich, L. Y. (1984). Improvement of the biotite-garnet geothermometer: correction for the fluorine content of biotite. *Doklady Akademii Nauk SSSR, 277*, 471-475.

Perchuk, L. L., & Lavrent'eva, I. V. (1983). Experimental Investigation of Exchange Equilibria in the System Cordierite-Garnet-Biotite. In S. K. Saxena, *Kinetics and Equilibrium in Mineral Reactions* (pp. 199-239).

Perry, H. K., Jaupart, C., Mareschal, J. C., & Bienfait, G. (2006). Crustal heat production in the Superior Province, Canadian Shield, and in North America inferred from heat flow data. *Journal of Geophysical Research, 111*, 1-20.

Pettke, T., Oberli, F., Audetat, A., Guillong, M., Simon, A. C., Hanley, J. J., & Klemm, L. M. (2012). Recent developments in element concentration and isotope ratio analysis of individual fluid inclusions by laser ablation single and multiple collector ICP-MS. *Ore Geology Reviews, 44*, 10-38.

Ravna, E. K. (2000). Distribution of Fe2+ and Mg between coexisting garnet and hornblende in synthetic and natural systems: an empirical calibration of the garnet-hornblende Fe-Mg geothermometer. *Lithos*, 265-277.

Ravna, E. K. (2000). The garnet-clinopyroxene Fe2+-Mg geothermometer: an updataed calibration. *Journal of Metamorphic Geology, 18*, 211-219.

Reimink, J. R., Chacko, T., Stern, R. A., & Heaman, L. M. (2014). Earth's earliest evolved crust generated in an Iceland-like setting. *Nature Geoscience, 7*, 529-533.

Rosenberg, P. E., & Franklin, F. F. (1977). Fe2+-F Avoidance in Silicates. *Geochimica et Cosmochimica Acta, 41*, 345-346.

Rudnick, R. L. (1992). Xenoliths-Samples of the lower continental crust. In D. M. Fountain , R. J. Arculus, & R. W. Kay, *The Continental Lower Crust* (pp. 269-316). Elsevier.

Rudnick, R. L., & Fountain, D. M. (1995, August). Nature and Composition of the Continential Crust: A Lower Crustal Perspective. *Reviews of Geophysics*, 267-309.

Rudnick, R. L., & Presper, T. (1990). Geochemistry of intermediate- to high-pressure granulites. In D. Vielzeuf, & P. Vidal, *Granulites and Crustal Evolution.* Norwell, Mass.: Kluwer.

Rudnick, R. L., & Taylor, S. R. (1987, December 10). The Composition and Petrogenesis of the Lower Crust: A Xenolith Study. *Journal of Geophysical Reseach, 92*(B13), 13981-14005.

Russell, J. K., Dipple, G. M., & Kopylova, M. G. (2001). Heat production and heat flow in the mantle lithosphere, Slave craton, Canada. *Physics of the Earth and Planetary Interiors, 123*, 27-44.

Sakar, C., Heaman, L. M., & Pearson, D. G. (2015). Duration and periodicity of kimberlite volcanic activity in the Lac de Gras kimberlite field, Canada and some recommendations for kimberlite geochronology. *Lithos, 218-219*, 155-166.

Shankland, T. J., & Ander, M. E. (1983). Electrical Conductivity, Temperatures, and Fluids in the Lower Crust. *Journal of Geophysical Research, 88*(B11), 9475-9484.

Shaw, D. M., Cramer, J. J., Higgins, M. D., & Truscott, M. G. (1986). Composition of the Canadian Precambrian shield and the continental crust of the Earth,. In J. B. Dawson, *Composition of the Canadian Precambrian shield and the continental crust of the Earth,* (Vol. 24).

Stern, R., & Bleeker, W. (1998). Age of the World's Oldest Rocks Refined Using Canada's SHRIMP: The Acasta Gneiss Complex, Northwest Territories, Canada. *Geoscience Canada, 25*(1), 27-31.

Taylor, S. R., & McLennan, S. M. (1986). The geochemical evolution of the continental crust. *Reviews in Geophysics, 33*, 241-265.

Thompson, P. H., Judge, A. S., & Lewis, T. J. (1995). *Thermal parameters in rock units of the Winter Lake-Lac de Gras area, central Slave Province, Northwest Territories - implications for diamond genesis.* Geological Survey of Canada.

Turcotte, D. L., & Schubert, G. (2002). *Geodynamics-2nd Edition.* Cambridge University Press.

van Breeman, O., Davis, W. J., & King, J. E. (1992). Temporal distribution of granitoid plutonc rocks in the Archean Slave Province, northwest Canadian Shield. *Canadian Journal of Earth Science, 29*, 2186-2199.

Weaver, B. L., & Tarney, J. (1984). Empirical approach to estimating the composition of the continental crust. *Nature, 310*, 575-577.

Whitney, D. L., & Evans, B. W. (2010). Abbreviations for names of Rock Forming Minerals. *American Mineralogist, 95*, 185-187.

Appendix A- Whole Rock Analyses

Whole rock analyses for 11 of the 15 xenoliths were done externally. Samples marked with an * were sent to the Peter Hooper GeoAnalytical Lab (Johnson et al, 1999) for whole rock and the remainder are from Krauss et al. (2007). The remaining 4 xenoliths were not large enough to send for whole rock. Major elements are in weight percent oxide while trace elements are in ppm.

	DDM-20*	MX-0011	1214	MX-0154	1542	1654	1554	DDM-303*	1638	1030	1525
SiO2	45.62	47.88	49.02	43.06	44.79	47.73	42.87	47.08	48.26	48.90	46.58
TiO2	0.68	0.91	1.24	1.19	0.83	0.23	1.33	1.04	1.02	1.19	1.97
Al2O3	14.84	14.09	15.02	16.09	14.76	17.17	21.41	20.12	16.14	19.67	12.80
FeO	10.06	11.45	12.38	14.74	13.39	6.09	16.79	11.13	10.78	8.43	11.65
MnO	0.21	0.23	0.17	0.56	0.21	0.12	0.22	0.15	0.18	0.13	0.21
MgO	15.12	7.02	8.70	8.75	13.32	10.86	9.73	9.83	10.60	7.54	9.46
CaO	3.21	14.25	9.06	11.24	7.97	15.20	3.22	2.66	8.49	8.65	12.17
Na2O	1.35	2.13	2.67	1.10	1.74	1.65	1.85	2.99	2.53	2.96	2.64
K2O	1.01	0.51	0.56	0.68	0.49	0.15	0.69	1.21	0.39	1.21	0.41
P2O5	0.08	0.08	0.13	0.12	0.52	0.07	0.08	0.08	0.20	0.21	0.32
Total	92.2	99.9	100.5	99.4	99.7	100.0	100.3	96.3	99.9	99.9	99.7
LOI	6.94	0.12	1.13	1.57	2.71	2.87	0.61	2.67	1.98	1.47	1.35
Rb	21.4	9.5	6.5	18.4	5.6	7.0	7.4	13.2	7.2	18.9	6.8
Sr	332	189	189	152	361	149	460	386	320	621	456
Y	18.4	13.8	26.2	24.5	32.2	3.2	25.6	29.6	9.6	18.1	34.6
Zr	111	37.1	105	29.5	26.1	5.0	66.9	158	46.5	67.6	114
Nb	6.82	5.51	8.84	4.21	5.87	2.87	12.39	16.79	4.76	4.78	14.87
Cs	0.43	0.06	0.12	0.29	0.13	0.13	0.09	0.13	0.17	0.20	0.15
Ba	1607	423	529	7300	434	2300	614	964	287	2883	337
La	24.3	4.8	9.9	4.9	23.0	2.1	19.1	35.6	11.8	11.7	25.5
Ce	39.4	11.2	24.6	12.1	50.3	3.7	33.5	62.6	27.3	29.1	67.9
Pr	4.03	1.56	3.50	1.77	6.64	0.46	3.73	6.80	3.57	4.35	9.96
Nd	14.3	7.1	15.4	8.1	27.3	1.7	15.0	24.8	14.3	20.4	43.5
Sm	3.27	1.94	4.58	2.55	5.10	0.46	5.62	6.38	2.73	4.77	9.35
Eu	1.57	0.79	1.26	2.63	1.53	0.77	1.71	1.88	0.90	2.10	2.69
Gd	3.73	2.24	5.42	3.52	4.87	0.56	6.48	7.00	2.51	4.54	8.52
Tb	0.60	0.33	0.86	0.59	0.66	0.07	0.89	1.11	0.28	0.57	1.12
Dy	3.6	2.8	5.6	4.7	5.6	0.7	5.9	6.2	2.1	3.8	7.7
Ho	0.70	0.58	1.03	1.00	1.30	0.12	1.07	1.17	0.39	0.72	1.46
Er	1.82	1.79	2.74	2.99	4.30	0.38	2.82	2.88	1.07	1.99	3.93
Tm	0.28	0.27	0.38	0.45	0.68	0.06	0.38	0.41	0.14	0.28	0.53
Yb	1.71	1.73	2.21	2.80	4.68	0.38	2.45	2.50	0.92	1.80	3.30
Lu	0.28	0.24	0.31	0.41	0.75	<d.l.	0.35	0.40	0.11	0.25	0.47
Hf	2.57	1.23	3.25	1.03	0.74	0.17	1.83	4.05	1.53	1.94	3.15
Ta	0.14	0.35	0.49	0.22	0.30	0.10	0.65	0.74	0.23	0.24	0.87
Pb	9.70	3.26	4.74	2.05	3.56	1.58	6.77	22.83	3.72	5.07	4.00
Th	0.41	0.76	0.53	0.57	1.05	0.34	0.62	1.32	0.27	0.29	0.49
U	0.51	0.59	0.26	0.46	0.29	0.19	0.28	0.69	0.17	0.31	0.28

Appendix B1-EPMA Standards for Thermometry

Biotite

Material	*Elements*	*Line*	*Crystal*	*Mineral*	*Source*
Topaz	F	Kα	PC1	Bt	1
Spessartine	Mn	Kα	LLIF	Bt	2
Sanidine	K	Kα	LPET	Bt	3
Frank Smith garnet	Si, Mg	Kα	LTAP	Bt	4
Diopside Wakefield	Ca	Kα	LPET	Bt	5
Rutile MTI	Ti	Kα	PET	Bt	6
Fayalite Rockport	Fe	Kα	LLIF	Bt	7
Chromium oxide Alfa	Cr	Kα	PET	Bt	8
Tugtupite	Cl, Na	Kα	LPET	Bt	18

Amphibole

Material	*Elements*	*Line*	*Crystal*	*Mineral*	*Source*
Topaz	F	Kα	PC1	Amph	1
Spessartine	Mn	Kα	LLIF	Amph	2
Sanidine	K	Kα	LPET	Amph	3
Frank Smith garnet	Si, Mg	Kα	LTAP	Amph	4
Diopside Wakefield	Ca	Kα	LPET	Amph	5
Rutile MTI	Ti	Kα	PET	Amph	6
Fayalite Rockport	Fe	Kα	LLIF	Amph	7
Chromium oxide Alfa	Cr	Kα	PET	Amph	8
Tugtupite	Cl, Na	Kα	LPET	Amph	18

Garnet

Material	*Elements*	*Line*	*Crystal*	*Mineral*	*Source*
Spessartine	Mn	Kα	LLIF	Grt	2
Sanidine	K	Kα	TAP	Grt	3
Gore garnet	Fe	Kα	LLIF	Grt	10
Frank Smith garnet	Al	Kα	LTAP	Grt	4
Rutile MTI	Ti	Kα	PET	Grt	6
Plagioclase (labradorite)	Ca	Kα	LPET	Grt	11
Chromium oxide Alfa	Cr	Kα	LLIF	Grt	8
Albite VA	Na	Kα	TAP	Grt	9

Clinopyroxene-Garnet EPMA Standard Assignments

Material	*Elements*	*Line*	*Crystal*	*Mineral*	*Source*
Spessartine	Mn	Kα	LLIF	Cpx	2
Sanidine	K	Kα	PETH	Cpx	3
Rutile MTI	Ti	Kα	PET	Cpx	6
Frank Smith garnet	Mg	Kα	LTAP	Cpx	4
Diopside Wakefield	Ca,Mg	Kα	LPET	Cpx	5
Fayalite Rockport	Fe	Kα	LLIF	Cpx	7
Albite VA	Si	Kα	TAP	Cpx	9
Chromium oxide Alfa	Cr	Kα	PET	Cpx	8

Material	*Elements*	*Line*	*Crystal*	*Mineral*	*Source*
Spessartine	Mn	Kα	LLIF	Grt	2
Gore garnet	Si, Al, Fe	Kα	LTAP,TAP, LLIF	Grt	10
Frank Smith garnet	Mg	Kα	LTAP	Grt	4
Rutile MTI	Ti	Kα	PET	Grt	6
Plagioclase (labradorite)	Ca	Kα	LPET	Grt	11
Chromium oxide Alfa	Cr	Kα	PET	Grt	8
Albite VA	Na	Kα	TAP	Grt	9

Appendix B1- EPMA standards for the collection of heat producing elements

Feldspars

Material	*Elements*	*Line*	*Crystal*	*Mineral*	*Source*
Sanidine	Si,Al,K	Kα	TAP,LTAP,LPET	Fds	3
SrTiO3	Ti	Kα	LPET	Fds	18
Gore garnet	Fe	Kα	LLIF	Fds	10
Frank Smith garnet	Mg	Kα	TAP	Fds	4
Plagioclase (labradorite)	Ca	Kα	PET	Fds	11
Albite VA	Na	Kα	LTAP	Fds	9

Amphibole/Mica

Material	*Elements*	*Line*	*Crystal*	*Mineral*	*Source*
Fayalite Rockport	Si	Kα	TAP	Amp/Bt	7
TiO2 Rutile MTI	Ti	Kα	PET	Amp/Bt	6
Gore garnet	Al	Kα	TAP	Amp/Bt	10
Chromium oxide Alfa	Cr	Kα	PET	Amp/Bt	8
Fayalite Rockport	Fe	Kα	LIFH	Amp/Bt	7
Spessartine	Mn	Kα	LIFH	Amp/Bt	2
Diopside Wakefield	Mg	Kα	TAP	Amp/Bt	5
Plagioclase (labradorite)	Ca	Kα	PETH	Amp/Bt	11
Albite VA	Na	Kα	TAP	Amp/Bt	9
Sanidine	K	Kα	PETH	Amp/Bt	3

Monazite

Material	*Elements*	*Line*	*Crystal*	*Mineral*	*Source*
Diopside Wakefield	Si, Ca	Kα	TAP	Mnz	5
PbSiO3 alamosite glass	Pb	mβ	PET	Mnz	12
Thorianite	Th	ma	PET	Mnz	13
Uraninite	U	mβ	PET	Mnz	14
YPO4	Y	la	PET	Mnz	12
LaPO4	La	la	LLIF	Mnz	15
CePO4	Ce	la	LLIF	Mnz	12
PrPO4	Pr	Lβ	LLIF	Mnz	12
NdPO4	Nd	Lβ	LLIF	Mnz	12
SmPO4	Sm	Lβ	LLIF	Mnz	12
GdPO4	Gd	Lβ	LLIF	Mnz	12
Fluorapatite Ca5(PO4)3F	P	Kα	PET	Mnz	16
Anhydrite ON CaSO4	S	Kα	PET	Mnz	17

List of Standards (updated from the supplementary material of Czas et al., 2018):

1. Topaz from the Thomas Range, Utah, assumes analysis from Handbook of mineralogy.
2. http://www.minsocam.org/msa/special/pig/pig_articles/etched_spssrtn.pdf
3. Ackermann S, Kunz M, Armbruster T, Schefer J and Hanni H (2005) Cation distribution in a Fe-bearing K-feldspar from Itrongay, Madagascar. A combined neutron-and X-ray single crystal diffraction study. Schweiz Miner Petrog 84:345-354. doi.org/10.5169/seals-63754
4. Royal Ontario Museum collection. Composition from bulk XRF analysis
5. http://astimex.com/com/catalog/min.html
6. http://www.mtixtl.com/tio2substrates.aspx
7. Jarosewich E, Nelen JA, Norberg JA (1980) Reference samples for electron microprobe analysis. Geostanard Newslett 4:43-47 (https://mineralsciences.si.edu/facilities/standards.htm)
8. Alfa Aesar Chromium (III) Oxide
9. McGuire AV, Francis CA, Dyar MD (1992) Minerals standards for electron microprobe analyses of oxygen. Am Mineral 77:1087-1091 (http://iageo.com/microanalytical-reference-materials/)
10. Vielzeuf D, Champenois M, Valley JW, Brunet F, and Devidal JL (2005) SIMS analyses of oxygen isotopes; matrix effects in Fe-Mg-Ca garnets. Chem Geol 223:208-226. doi:10.1016/j.chemgeo.2005.07.008
11. Jarosewich E, Nelen JA, Norberg JA (1980) Reference samples for electron microprobe analysis. Geostanard Newslett 4:43-47 (https://mineralsciences.si.edu/facilities/standards.htm)
12. Synthetic from Dr. J Hanchar, Memorial University of Newfoundland
13. Synthetic Material
14. Synthetic Material
15. Smithsonian Collection of REE phosphates, synthetized by Cherniak
16. Tacker RC (2004) Hydroxyl ordering in igneous apatite. Am Mineral 89:1411–1421
17. EAS Museum Sample M2790, McLaren Mine, Ontario, Canada Sr content assumed in house
18. Tugtupite from Greenland, Ilimaussaq intrusion, Tugtup agtakorfia (type locality)

Appendix B2- EPMA data for thermometry, biotite/amphibole/clinopyroxene analyses are paired with garnets of the same analysis # (e.g. biotite analysis 1 is to be paired with garnet analysis 1). Clinopyroxene temperatures (Krogh-Ravna, 2000b) are presented with their garnets (pairs 34-76).

Table B1. Biotite Compositions - EPMA

Sample	DDM-20	MX-0154	MX-0154	MX-0154	MX-0154	MX-0154	MX-0125	MX-0125	MX-0125	1554	1554	1554
Anal. #	1	2	3	4	5	6	7	8	9	10	11	12
SiO2	40.4	38.12	38.31	37.98	38.39	37.7	37.71	37.4	37.05	38.55	38.47	38.61
TiO2	3.97	4.28	4.9	5.07	4.43	4.88	5.65	5.5	5.61	2.88	2.22	2.93
Al2O3	13.85	15.48	14	14.32	14.38	14.41	14.98	14.52	14.63	15.18	16.77	15.95
Cr2O3	0.09	0.03	0	0	0.01	0.01	0.09	0.05	0.05	0.13	0.13	0.23
FeO	4.85	8.9	11.65	11.21	10.56	11.23	11.84	13.84	13.99	7.93	6.69	5.83
MnO	0	0.02	0.01	0.01	0	0.02	0.02	0.02	0	0.02	0.01	0.01
MgO	22.67	18.23	17.48	17.18	17.97	17.05	15.72	14.84	14.46	20.34	20.88	21.52
CaO	0	0.02	0.04	0.04	0.04	0.05	0.01	0.02	0	0.02	0.01	0.02
Na2O	0.1	0.14	0.12	0.2	0.21	0.19	0.24	0.05	0.06	0.31	0.18	0.47
K2O	9.9	9.65	9.64	9.74	9.99	9.9	9.77	9.78	9.93	9.65	10.12	9.62
F	2.15	1.36	0.9	1.02	1.04	1.04	0.32	0.19	0.21	0.68	0.89	0.59
Cl	0.12	0.09	0.03	0.05	0.03	0.04	0.22	0.11	0.11	0.05	0.07	0.06
O=F	0.9	0.57	0.38	0.43	0.44	0.44	0.13	0.08	0.09	0.28	0.37	0.25
O=Cl	0.03	0.02	0.01	0.01	0.01	0.01	0.05	0.03	0.02	0.01	0.02	0.01
Total	97.18	95.73	96.68	96.39	96.59	96.07	96.38	96.21	95.98	95.45	96.05	95.56
11 Oxy												
Si	2.855	2.776	2.794	2.779	2.794	2.772	2.759	2.764	2.751	2.792	2.758	2.764
Ti	0.211	0.235	0.269	0.279	0.243	0.27	0.311	0.306	0.313	0.157	0.119	0.158
Al	1.154	1.329	1.203	1.235	1.234	1.249	1.292	1.265	1.281	1.296	1.417	1.346
Cr	0.005	0.001	0	0	0	0.001	0.005	0.003	0.003	0.008	0.007	0.013
Fe	0.287	0.542	0.71	0.686	0.643	0.69	0.725	0.856	0.869	0.48	0.401	0.349
Mn	0	0.001	0.001	0.001	0	0.001	0.001	0.001	0	0.001	0	0
Mg	2.389	1.979	1.9	1.874	1.95	1.869	1.714	1.635	1.601	2.196	2.232	2.297
Ca	0	0.001	0.003	0.003	0.003	0.004	0	0.001	0	0.001	0.001	0.001
Na	0.014	0.02	0.016	0.028	0.03	0.027	0.034	0.008	0.008	0.043	0.024	0.066
K	0.893	0.896	0.897	0.909	0.927	0.928	0.912	0.922	0.941	0.892	0.926	0.878
F	0.48	0.313	0.207	0.236	0.239	0.243	0.074	0.043	0.05	0.155	0.201	0.133
Cl	0.014	0.011	0.004	0.006	0.004	0.005	0.028	0.014	0.014	0.006	0.009	0.007

Table B2. Biotite Compositions – EPMA cont.

Sample	1554	1554	1542	1542	1542	1542	1542
***Anal.* #**	13	14	15	16	17	18	19
SiO2	39.1	38.9	39.16	39.84	40.29	39.96	39.57
TiO2	2.49	2	4.22	4.44	4.53	4.41	4.32
Al2O3	15.67	14.33	13.56	13.53	13.53	13.3	13.41
Cr2O3	0.33	0.01	0.07	0.07	0.03	0.12	0.09
FeO	6.16	10.35	6.66	7	6.07	6.18	7.42
MnO	0	0.01	0	0	0.01	0	0.01
MgO	21.52	19.62	21.38	20.75	22.02	21.36	20.94
CaO	0	0.01	0.03	0.01	0.03	0	0.02
Na2O	0.59	0.19	0.12	0.14	0.16	0.16	0.15
K2O	9.4	9.99	9.8	10.33	9.93	10.25	9.81
F	0.83	0.97	2.39	2.35	2.37	2.46	2.26
Cl	0.14	0.09	0.17	0.14	0.14	0.14	0.13
O=F	0.35	0.41	1.01	0.99	1	1.04	0.95
O=Cl	0.03	0.02	0.04	0.03	0.03	0.03	0.03
Total	95.84	96.03	96.52	97.58	98.09	97.26	97.15
11 Oxy							
Si	2.796	2.841	2.823	2.848	2.845	2.856	2.839
Ti	0.134	0.11	0.229	0.239	0.24	0.237	0.233
Al	1.32	1.233	1.152	1.14	1.126	1.12	1.134
Cr	0.019	0.001	0.004	0.004	0.002	0.007	0.005
Fe	0.368	0.632	0.401	0.419	0.359	0.369	0.445
Mn	0	0.001	0	0	0.001	0	0.001
Mg	2.294	2.136	2.298	2.211	2.318	2.275	2.24
Ca	0	0	0.002	0	0.002	0	0.001
Na	0.081	0.027	0.017	0.019	0.022	0.023	0.02
K	0.857	0.931	0.902	0.942	0.894	0.935	0.898
F	0.188	0.225	0.545	0.531	0.529	0.556	0.513
Cl	0.017	0.011	0.021	0.017	0.017	0.016	0.016

Table B3. Amphibole Compositions – EPMA

Sample	1214	1214	1214	1214	1214	1214	1214	1214	1214	MX-0154	MX-0125	MX-0125
Anal. #	20	21	22	23	24	25	26	27	28	29	30	31
SiO_2	41.68	42.25	41.11	41.22	40.96	40.81	41.11	41.18	41.71	41.90	43.06	43.06
TiO_2	2.48	2.42	2.65	2.31	2.68	2.56	2.13	2.62	1.86	3.36	2.12	2.12
Al_2O_3	12.05	11.92	12.31	12.73	12.68	13.17	12.20	11.96	12.17	13.34	12.41	12.41
Cr_2O_3	0.03	0.04	0.06	0.03	0.04	0.03	0.06	0.06	0.05	0.01	0.06	0.06
FeO	13.16	12.45	13.90	13.88	13.56	13.80	14.06	13.89	13.19	9.95	12.59	12.59
MnO	0.04	0.03	0.03	0.03	0.03	0.03	0.03	0.03	0.02	0.07	0.05	0.05
MgO	12.20	12.89	11.81	11.84	11.85	11.57	11.76	11.76	12.54	13.50	12.36	12.36
CaO	11.44	11.47	11.37	11.40	11.41	11.36	11.58	11.48	11.62	11.44	11.66	11.66
Na_2O	2.22	2.14	2.00	2.06	2.10	2.09	1.61	1.77	1.47	1.67	1.54	1.54
K2O	1.83	1.78	2.16	2.00	1.92	1.94	2.38	2.33	2.43	2.25	1.74	1.74
F	0.40	0.42	0.50	0.50	0.50	0.41	0.50	0.45	0.57	0.43	0.00	0.00
Cl	0.31	0.28	0.24	0.33	0.30	0.31	0.32	0.31	0.35	0.08	0.00	0.00
O=F	0.17	0.18	0.21	0.21	0.21	0.17	0.21	0.19	0.24	0.18	0.00	0.00
O=Cl	0.07	0.06	0.05	0.07	0.07	0.07	0.07	0.07	0.08	0.02	0.00	0.00
Total	97.59	97.85	97.87	98.04	97.76	97.82	97.46	97.58	97.65	97.79	97.58	97.58
22 Oxy												
Si	5.985	6.020	5.919	5.918	5.892	5.867	5.955	5.952	5.999	5.899	6.095	6.095
Ti	0.268	0.259	0.287	0.249	0.290	0.276	0.232	0.284	0.201	0.356	0.225	0.225
Al	2.039	2.001	2.089	2.154	2.151	2.232	2.083	2.038	2.063	2.213	2.071	2.071
Cr	0.003	0.005	0.007	0.003	0.005	0.004	0.007	0.007	0.005	0.001	0.007	0.007
Fe	1.581	1.484	1.674	1.666	1.631	1.659	1.703	1.679	1.586	1.172	1.490	1.490
Mn	0.004	0.004	0.003	0.004	0.004	0.004	0.004	0.004	0.003	0.008	0.006	0.006
Mg	2.612	2.737	2.535	2.534	2.541	2.479	2.540	2.535	2.689	2.833	2.608	2.608
Ca	1.760	1.751	1.754	1.754	1.759	1.750	1.798	1.779	1.790	1.726	1.768	1.768
Na	0.617	0.592	0.557	0.574	0.586	0.582	0.454	0.496	0.411	0.455	0.423	0.423
K	0.334	0.324	0.396	0.367	0.352	0.356	0.441	0.431	0.446	0.404	0.314	0.314
F	0.183	0.188	0.229	0.227	0.225	0.184	0.228	0.204	0.260	0.193	0.000	0.000
Cl	0.076	0.067	0.059	0.081	0.074	0.075	0.079	0.076	0.086	0.019	0.000	0.000

Table B4. Amphibole Compositions – EPMA cont.

Sample	MX-0125	MX-0125
***Anal.* #**	32	33
SiO_2	43.60	43.60
TiO_2	1.95	1.95
Al_2O_3	12.06	12.06
Cr_2O_3	0.06	0.06
FeO	12.24	12.24
MnO	0.05	0.05
MgO	12.91	12.91
CaO	11.69	11.69
Na_2O	1.47	1.47
K2O	1.68	1.68
F	0.00	0.00
Cl	0.00	0.00
O=F	0.00	0.00
O=Cl	0.00	0.00
Total	97.70	97.70
22 Oxy		
Si	5.985	6.020
Ti	0.268	0.259
Al	2.039	2.001
Cr	0.003	0.005
Fe	1.581	1.484
Mn	0.004	0.004
Mg	2.612	2.737
Ca	1.760	1.751
Na	0.617	0.592
K	0.334	0.324
F	0.183	0.188
Cl	0.076	0.067

Table B5. Clinopyroxene Compositions – EPMA

Sample	1030	1030	1030	1030	1030	1030	1030	1140	1140	1140	1140	1140
***Anal.* #**	34	35	36	37	38	39	40	41	42	43	44	45
SiO_2	52.21	51.51	52.14	51.58	51.21	52.21	51.85	51.14	51.07	51.51	51.51	51.95
TiO_2	0.41	0.27	0.37	0.45	0.49	0.41	0.51	0.31	0.32	0.27	0.27	0.19
Al_2O_3	4.07	4.46	4.06	4.72	4.68	4.07	4.33	3.23	2.96	2.63	2.63	2.07
Cr_2O_3	0	0.01	0	0.01	0	0.01	0	0.05	0.02	0.04	0.03	0.03
FeO	6.58	6.57	6.44	6.89	7.1	6.46	6.75	9.85	9.12	10.14	10.04	9.6
MnO	0.04	0.06	0.04	0.04	0.04	0.04	0.04	0.14	0.11	0.14	0.14	0.14
MgO	13.26	13.75	13.38	12.63	12.53	13.21	12.95	12.02	12.62	12.5	12.47	12.75
CaO	21.28	21.48	21.71	21.06	21.26	21.6	21.57	21.83	22.02	21.58	21.8	22.11
Na_2O	1.33	1.04	1.22	1.46	1.35	1.31	1.27	0.73	0.73	0.66	0.64	0.63
Total	99.2	99.15	99.36	98.83	98.66	99.34	99.26	99.3	98.96	99.46	99.53	99.46
6 Oxy												
Si	1.938	1.915	1.933	1.925	1.918	1.936	1.927	1.931	1.931	1.942	1.941	1.956
Ti	0.011	0.007	0.01	0.013	0.014	0.011	0.014	0.009	0.009	0.008	0.008	0.005
Al	0.178	0.196	0.178	0.208	0.207	0.178	0.189	0.144	0.132	0.117	0.117	0.092
Cr	0	0	0	0	0	0	0	0.001	0.001	0.001	0.001	0.001
Fe	0.204	0.204	0.2	0.215	0.223	0.2	0.21	0.311	0.288	0.32	0.317	0.302
Mn	0.001	0.002	0.001	0.001	0.001	0.001	0.001	0.004	0.003	0.004	0.005	0.004
Mg	0.734	0.762	0.74	0.703	0.7	0.73	0.717	0.677	0.711	0.703	0.7	0.716
Ca	0.846	0.855	0.862	0.842	0.853	0.858	0.859	0.883	0.892	0.872	0.881	0.892
Na	0.096	0.075	0.087	0.105	0.098	0.094	0.092	0.054	0.053	0.048	0.047	0.046
Total	4.009	4.017	4.011	4.011	4.014	4.01	4.01	4.014	4.021	4.015	4.016	4.015

Table B6. Clinopyroxene Compositions – EPMA cont.

Sample	1140	1214	1214	1214	1214	1214	1214	1214	1214	1214	1612	1612
***Anal.* #**	46	47	48	49	50	51	52	53	54	55	56	57
SiO_2	51.03	51.27	50.83	51.08	51.22	52.39	51.65	51.06	50.82	51.7	51.18	51.26
TiO_2	0.36	0.36	0.33	0.34	0.27	0.27	0.35	0.36	0.38	0.25	0.4	0.47
Al_2O_3	2.88	2.73	3.25	2.97	2.68	2.09	2.61	3.09	3.36	2.78	2.99	3.11
Cr_2O_3	0.01	0.05	0.03	0.05	0.04	0.03	0.02	0.03	0.03	0.03	0.05	0
FeO	9.86	10.3	9.3	10.25	9.73	8.93	9.24	10.22	9.98	9.17	9.28	9.17
MnO	0.13	0.1	0.1	0.12	0.1	0.09	0.09	0.1	0.11	0.09	0.24	0.23
MgO	12.28	12.69	13.66	12.25	12.68	13.2	12.86	12.28	12.1	12.6	12.51	12.29
CaO	21.91	21.17	20.59	21.51	21.68	21.94	21.62	21.19	21.35	21.76	21.96	22.03
Na_2O	0.63	0.65	0.62	0.67	0.64	0.66	0.73	0.71	0.72	0.73	0.58	0.62
Total	99.1	99.33	98.7	99.24	99.05	99.61	99.18	99.03	98.84	99.11	99.19	99.18
6 Oxy												
Si	1.932	1.936	1.92	1.932	1.938	1.961	1.945	1.933	1.927	1.948	1.931	1.933
Ti	0.01	0.01	0.009	0.01	0.008	0.008	0.01	0.01	0.011	0.007	0.011	0.013
Al	0.129	0.122	0.145	0.132	0.12	0.092	0.116	0.138	0.15	0.124	0.133	0.138
Cr	0	0.001	0.001	0.001	0.001	0.001	0.001	0.001	0.001	0.001	0.002	0
Fe	0.312	0.325	0.294	0.324	0.308	0.28	0.291	0.323	0.316	0.289	0.293	0.289
Mn	0.004	0.003	0.003	0.004	0.003	0.003	0.003	0.003	0.003	0.003	0.008	0.007
Mg	0.693	0.714	0.769	0.691	0.715	0.736	0.722	0.693	0.684	0.707	0.703	0.691
Ca	0.889	0.857	0.834	0.872	0.879	0.88	0.872	0.859	0.868	0.878	0.888	0.89
Na	0.046	0.048	0.046	0.049	0.047	0.048	0.054	0.052	0.053	0.053	0.043	0.045
Total	4.016	4.016	4.021	4.016	4.018	4.009	4.014	4.013	4.013	4.01	4.012	4.007

Table B7. Clinopyroxene Compositions – EPMA cont.

Sample	1612	1612	1612	1612	1612	1654	1654	MX-0011	MX-0011	MX-0011	MX-0011	MX-0011
Anal. #	58	59	60	61	62	63	64	65	66	67	68	69
SiO_2	50.9	51.58	51.21	51.35	50.95	51.64	51.86	50.78	51.14	50.59	51.08	51.26
TiO_2	0.52	0.39	0.53	0.39	0.49	0.42	0.38	0.89	0.51	0.69	0.66	0.61
Al_2O_3	3.37	2.98	3	3	3.47	4.34	4.26	5.01	5.08	5.33	4.83	5.24
Cr_2O_3	0.05	0.06	0.04	0.06	0.07	0.09	0.1	0.04	0.05	0.05	0.04	0.05
FeO	9.66	8.46	9.54	9.21	9.81	4.67	4.32	8.78	8.88	8.78	9.02	8.78
MnO	0.24	0.18	0.26	0.23	0.25	0.04	0.04	0.08	0.08	0.09	0.08	0.07
MgO	11.88	12.78	12.4	12.23	11.68	14.17	14.39	11.23	11.24	11.22	11.31	11.19
CaO	22.03	22.17	21.92	22.26	21.97	22.64	22.68	21.25	21.2	21.25	21.18	21.09
Na_2O	0.67	0.65	0.59	0.61	0.66	0.84	0.85	1.48	1.49	1.43	1.49	1.61
Total	99.32	99.25	99.49	99.33	99.34	98.86	98.88	99.53	99.67	99.42	99.68	99.9
6 Oxy												
Si	1.923	1.937	1.929	1.935	1.925	1.915	1.919	1.902	1.912	1.897	1.911	1.91
Ti	0.015	0.011	0.015	0.011	0.014	0.012	0.01	0.025	0.014	0.019	0.018	0.017
Al	0.15	0.132	0.133	0.133	0.154	0.19	0.186	0.221	0.224	0.235	0.213	0.23
Cr	0.001	0.002	0.001	0.002	0.002	0.003	0.003	0.001	0.002	0.001	0.001	0.002
Fe	0.305	0.266	0.3	0.29	0.31	0.145	0.134	0.275	0.278	0.275	0.282	0.274
Mn	0.008	0.006	0.008	0.007	0.008	0.001	0.001	0.003	0.003	0.003	0.003	0.002
Mg	0.669	0.716	0.696	0.687	0.657	0.783	0.794	0.627	0.627	0.627	0.631	0.622
Ca	0.892	0.892	0.885	0.899	0.889	0.9	0.899	0.853	0.849	0.854	0.849	0.842
Na	0.049	0.047	0.043	0.044	0.048	0.061	0.061	0.107	0.108	0.104	0.108	0.117
Total	4.011	4.008	4.01	4.009	4.007	4.008	4.007	4.015	4.015	4.017	4.017	4.015

Table B8. Clinopyroxene Compositions – EPMA cont.

Sample	MX-0011	MX-0111	MX-0111	MX-0111	MX-0111	MX-0125	MX-0125
***Anal.* #**	70	71	72	73	74	75	76
SiO_2	51.01	51.52	50.97	51.24	51.44	52.83	52.52
TiO_2	0.69	0.33	0.4	0.37	0.36	0.21	0.28
Al_2O_3	4.99	2.82	3.14	3.05	2.99	2.17	2.42
Cr_2O_3	0.04	0.05	0.05	0.04	0.04	0.03	0.03
FeO	8.71	9.64	10	10.17	9.64	7.12	7.62
MnO	0.08	0.2	0.23	0.22	0.2	0.13	0.14
MgO	11.32	12.32	11.9	12.02	12.31	13.92	13.57
CaO	21.24	22.13	22.22	21.93	22.09	22.93	22.5
Na_2O	1.51	0.71	0.65	0.67	0.72	0.7	0.7
Total	99.58	99.7	99.55	99.72	99.78	100.02	99.79
6 Oxy							
Si	1.908	1.937	1.925	1.931	1.933	1.958	1.954
Ti	0.02	0.009	0.011	0.011	0.01	0.006	0.008
Al	0.22	0.125	0.14	0.136	0.132	0.095	0.106
Cr	0.001	0.001	0.002	0.001	0.001	0.001	0.001
Fe	0.273	0.303	0.316	0.321	0.303	0.221	0.237
Mn	0.002	0.006	0.007	0.007	0.006	0.004	0.005
Mg	0.632	0.69	0.67	0.675	0.689	0.769	0.753
Ca	0.851	0.892	0.899	0.885	0.889	0.91	0.897
Na	0.109	0.052	0.047	0.049	0.053	0.05	0.051
Total	4.016	4.016	4.017	4.015	4.017	4.013	4.01

Table B9. Garnet Compositions – EPMA

Sample	DDM-20	MX-0154	MX-0154	MX-0154	MX-0154	MX-0154	MX-0125	MX-0125	MX-0125	1554	1554	1554
Anal. **#**	1	2	3	4	5	6	7	8	9	10	11	12
SiO_2	38.94	38.2	38.77	39.12	38.2	38.07	38.10	38.71	37.83	38.88	39.56	39.62
TiO_2	0.04	0.07	0.03	0.07	0.06	0.03	0.10	0.05	0.06	0.03	0.02	0.05
Al_2O_3	22.13	21.87	22.32	22.53	22.06	21.72	21.81	21.83	21.87	22.56	22.23	22.35
Cr_2O_3	0.06	0.03	0	0.01	0	0.01	0.09	0.05	0.06	0.05	0.1	0.08
FeO	24.15	24.74	25.48	24.92	24.98	25.45	25.35	25	25.32	26.45	24.56	23.36
MnO	0.28	1.01	0.94	0.9	0.93	0.95	1.42	1.28	1.26	0.39	0.36	0.34
MgO	10.36	6.33	5.48	5.9	6.23	5.83	6.03	5.72	5.34	7.92	9.68	11.07
CaO	3.08	6.65	7.42	7.28	6.88	6.61	6.63	7.71	7.48	4.15	3.73	3
Na_2O	0.02	0.01	0.01	0	0	0	0.01	0	0	0.02	0.01	0
Total	99.1	98.91	100.49	100.76	99.35	98.67	99.54	100.35	99.22	100.45	100.26	99.87
12 Oxy												
Si	2.989	2.99	2.996	3.002	2.98	2.996	2.98	2.998	2.973	2.982	3.007	3
Ti	0.002	0.004	0.002	0.004	0.003	0.002	0.01	0.003	0.003	0.002	0.001	0.003
Al	2.002	2.018	2.033	2.038	2.028	2.015	2.01	1.993	2.026	2.039	1.991	1.995
Cr	0.004	0.002	0	0.001	0	0.001	0.01	0.003	0.004	0.003	0.006	0.005
Fe	1.55	1.619	1.647	1.599	1.63	1.675	1.66	1.62	1.664	1.697	1.562	1.479
Mn	0.018	0.067	0.062	0.059	0.062	0.064	0.09	0.084	0.084	0.025	0.023	0.022
Mg	1.185	0.738	0.631	0.675	0.724	0.685	0.70	0.661	0.626	0.906	1.097	1.25
Ca	0.254	0.558	0.615	0.598	0.575	0.557	0.56	0.64	0.63	0.341	0.304	0.243
Na	0.003	0.001	0.001	0	0	0	0.00	0	0	0.003	0.002	0
Total	8.008	7.997	7.986	7.975	8.002	7.994	8.01	8.001	8.009	7.997	7.994	7.997

Table B10. Garnet Compositions – EPMA cont.

Sample	1554	1554	1542	1542	1542	1542	1542	1214	1214	1214	1214	1214
Anal. #	13	14	15	16	17	18	19	20	21	22	23	24
SiO_2	39.36	39.11	38.6	39.98	39.23	38.37	39.1	39.12	38.98	39.08	38.89	38.70
TiO_2	0.02	0.03	0.06	0.01	0.08	0	0.06	0.07	0.11	0.07	0.04	0.04
Al_2O_3	22.63	22.29	22.25	22.71	21.77	21.91	22.11	20.87	20.86	20.83	20.90	20.95
Cr_2O_3	0.12	0.07	0.02	0.04	0.04	0.07	0.06	0.06	0.06	0.09	0.06	0.05
FeO	24.26	26.13	24.37	22.25	22.89	22.54	23.64	27.04	26.37	27.29	26.70	26.57
MnO	0.32	0.32	0.44	0.54	0.46	0.55	0.55	0.85	0.83	0.90	0.87	0.80
MgO	9.69	7.99	7.59	9.36	8.8	8.55	8.21	5.34	5.39	5.01	5.18	5.45
CaO	4.04	4.44	6.4	6.36	6.03	6.22	5.81	6.50	6.51	6.47	6.53	6.45
Na_2O	0.03	0.01	0	0.02	0	0	0	0.00	0.03	0.02	0.02	0.00
Total	100.47	100.39	99.76	101.28	99.33	98.22	99.55	99.86	99.12	99.77	99.19	99.02
12 Oxy												
Si	2.984	2.998	2.977	2.998	3.013	2.984	3.005	3.057	3.060	3.061	3.057	3.045
Ti	0.001	0.001	0.004	0	0.004	0	0.003	0.004	0.006	0.004	0.002	0.002
Al	2.022	2.014	2.023	2.007	1.971	2.009	2.003	1.922	1.930	1.923	1.936	1.943
Cr	0.007	0.004	0.001	0.002	0.002	0.004	0.004	0.004	0.003	0.006	0.004	0.003
Fe	1.539	1.675	1.572	1.395	1.47	1.466	1.519	1.767	1.731	1.788	1.755	1.748
Mn	0.021	0.021	0.029	0.035	0.03	0.036	0.036	0.056	0.055	0.060	0.058	0.054
Mg	1.096	0.913	0.872	1.046	1.008	0.991	0.941	0.622	0.630	0.585	0.607	0.640
Ca	0.329	0.365	0.529	0.511	0.496	0.518	0.478	0.544	0.548	0.543	0.550	0.544
Na	0.004	0.001	0	0.003	0	0	0	0.001	0.005	0.003	0.003	0.000
Total	8.002	7.992	8.007	7.998	7.996	8.009	7.989	7.977	7.969	7.973	7.972	7.979

Table B11. Garnet Compositions – EPMA cont.

Sample	1214	1214	1214	1214	MX-0154	MX-0125	MX-0125	MX-0125	MX-0125	1030	1030	1030
***Anal.* #**	25	26	27	28	29	30	31	32	33	34	35	36
SiO_2	38.63	38.75	39.42	38.60	39.12	38.28	38.75	38.35	38.50	39.25	39.63	39.35
TiO_2	0.06	0.04	0.06	0.05	0.05	0.04	0.03	0.07	0.07	0	0.04	0.04
Al_2O_3	21.12	21.21	20.67	21.16	22.14	22.02	21.75	21.90	21.91	22.66	22.96	22.94
Cr_2O_3	0.03	0.05	0.05	0.06	0.01	0.06	0.07	0.06	0.04	0	0	0
FeO	26.83	26.22	26.91	26.39	23.71	25.06	24.98	25.22	25.10	21.97	21.92	22.1
MnO	0.83	0.78	0.83	0.82	1.08	1.28	1.26	1.34	1.36	0.37	0.37	0.41
MgO	5.11	5.67	5.13	5.35	6.62	5.64	5.98	5.81	5.84	8.73	8.58	8.68
CaO	6.51	6.45	6.48	6.63	7.48	7.50	7.45	7.04	7.15	7.1	7.6	7.27
Na_2O	0.01	0.02	0.00	0.01	0.00	0.00	0.00	0.00	0.01	0	0	0
Total	99.12	99.17	99.55	99.06	100.21	99.88	100.27	99.79	99.97	100.08	101.1	100.79
12 Oxy												
Si	3.040	3.037	3.085	3.035	3.008	2.981	3.001	2.988	2.992	2.983	2.982	2.972
Ti	0.004	0.002	0.003	0.003	0.003	0.002	0.002	0.004	0.004	0	0.002	0.002
Al	1.959	1.960	1.907	1.961	2.006	2.021	1.986	2.011	2.007	2.03	2.036	2.042
Cr	0.002	0.003	0.003	0.004	0.000	0.004	0.005	0.004	0.003	0	0	0
Fe	1.766	1.719	1.761	1.735	1.524	1.632	1.618	1.643	1.631	1.397	1.379	1.396
Mn	0.056	0.052	0.055	0.054	0.070	0.084	0.082	0.088	0.089	0.024	0.024	0.026
Mg	0.599	0.663	0.598	0.627	0.758	0.655	0.690	0.675	0.677	0.989	0.962	0.977
Ca	0.549	0.542	0.544	0.559	0.616	0.626	0.618	0.587	0.596	0.578	0.613	0.588
Na	0.002	0.003	0.000	0.002	0.000	0.000	0.001	0.000	0.001	0	0	0
Total	7.976	7.981	7.957	7.981	7.986	8.005	8.003	8.001	8.000	8.001	7.998	8.005
T(°C)	-	-	-	-	-	-	-	-	-	666	631	685

Table B12. Garnet Compositions – EPMA cont.

Sample	1030	1030	1030	1030	1140	1140	1140	1140	1140	1140	1214	1214
***Anal.* #**	37	38	39	40	41	42	43	44	45	46	47	48
SiO_2	39.47	39.21	39.7	39.21	38.04	38.13	38.19	38.92	37.87	37.99	37.98	38.1
TiO_2	0.05	0.06	0.05	0.06	0.06	0.04	0.06	0.03	0.03	0.07	0.05	0.04
Al_2O_3	22.58	22.55	22.7	22.82	21.28	21.52	21.39	21.28	21.37	21.4	21.88	22
Cr_2O_3	0	0	0	0	0.08	0.08	0.05	0.08	0.05	0.02	0.06	0.07
FeO	21.88	21.8	21.55	21.82	25.83	26.13	26.07	25.31	26.4	26.23	26.63	26.54
MnO	0.38	0.36	0.4	0.35	1.05	1.05	1.07	1.09	1.24	1.11	0.81	0.81
MgO	8.6	8.72	8.91	8.51	5.51	5.76	5.41	6.72	4.85	5.52	5.27	5.46
CaO	7.46	7.26	7.2	7.57	7.11	6.73	7.01	6.95	7.35	6.91	6.75	6.77
Na_2O	0	0	0	0	0	0	0.01	0.01	0	0	0	0
Total	100.42	99.96	100.51	100.34	98.97	99.45	99.25	100.38	99.16	99.25	99.43	99.79
12 Oxy												
Si	2.991	2.984	2.997	2.974	2.999	2.991	3.003	3.01	2.992	2.99	2.982	2.978
Ti	0.003	0.003	0.003	0.003	0.003	0.003	0.003	0.002	0.002	0.004	0.003	0.002
Al	2.017	2.023	2.02	2.04	1.977	1.989	1.982	1.94	1.991	1.985	2.025	2.027
Cr	0	0	0	0	0.005	0.005	0.003	0.005	0.003	0.001	0.004	0.004
Fe	1.387	1.387	1.36	1.384	1.703	1.714	1.714	1.637	1.745	1.727	1.749	1.735
Mn	0.024	0.023	0.026	0.022	0.07	0.07	0.071	0.071	0.083	0.074	0.054	0.054
Mg	0.971	0.989	1.003	0.962	0.647	0.673	0.634	0.774	0.571	0.648	0.617	0.636
Ca	0.606	0.592	0.582	0.615	0.601	0.565	0.591	0.576	0.623	0.583	0.568	0.567
Na	0	0	0	0	0	0	0.001	0.001	0	0	0	0
Total	7.998	8.002	7.99	8.002	8.007	8.01	8.002	8.016	8.01	8.012	8.001	8.004
T(°C)	680	676	684	699	708	654	700	653	612	635	618	618

Table B13. Garnet Compositions – EPMA cont.

Sample	1214	1214	1214	1214	1214	1214	1214	1612	1612	1612	1612	1612
Anal. #	49	50	51	52	53	54	55	56	57	58	59	60
SiO_2	37.88	37.81	38.22	38.16	38.09	38.34	38.04	38.29	38.4	38.17	38.32	38.7
TiO_2	0.07	0.04	0.05	0.08	0.09	0.05	0	0.06	0.09	0.08	0.08	0.05
Al_2O_3	21.76	21.43	21.49	21.67	21.71	22.08	21.91	22.09	22.14	21.69	22.05	21.95
Cr_2O_3	0.1	0.05	0.05	0	0.03	0.05	0.09	0.07	0.1	0.12	0.13	0.11
FeO	27.51	27.03	26.2	26.07	26.14	26.33	26.58	24.7	24.27	24.47	24.28	24.84
MnO	0.93	0.9	0.81	0.85	0.79	0.77	0.79	2.18	2.09	2.22	2	2.18
MgO	4.96	4.88	5.45	5.96	5.7	5.58	5.47	4.88	4.96	4.52	4.59	5.15
CaO	6.69	6.93	6.95	6.63	6.77	6.91	6.7	7.98	8.15	8.59	8.83	7.64
Na_2O	0	0	0	0	0	0	0	0	0	0.02	0	0
Total	99.9	99.07	99.22	99.42	99.32	100.11	99.58	100.25	100.2	99.88	100.28	100.62
12 Oxy												
Si	2.975	2.991	3.003	2.988	2.987	2.983	2.98	2.981	2.985	2.989	2.982	2.998
Ti	0.004	0.002	0.003	0.005	0.005	0.003	0	0.004	0.005	0.005	0.005	0.003
Al	2.014	1.998	1.99	2	2.007	2.025	2.023	2.027	2.028	2.002	2.023	2.004
Cr	0.006	0.003	0.003	0	0.002	0.003	0.006	0.004	0.006	0.007	0.008	0.007
Fe	1.807	1.788	1.722	1.707	1.714	1.713	1.742	1.608	1.578	1.602	1.58	1.609
Mn	0.062	0.06	0.054	0.056	0.052	0.051	0.052	0.144	0.138	0.147	0.132	0.143
Mg	0.581	0.575	0.638	0.696	0.666	0.647	0.639	0.566	0.575	0.528	0.532	0.595
Ca	0.563	0.587	0.585	0.556	0.569	0.576	0.562	0.666	0.679	0.721	0.736	0.634
Na	0	0	0	0	0	0	0	0	0	0.003	0	0
Total	8.011	8.006	7.998	8.008	8.003	8	8.005	8	7.993	8.004	7.998	7.993
T(°C)	653	688	680	629	724	738	694	708	698	707	606	636

Table B14. Garnet Compositions – EPMA cont.

Sample	1612	1612	1654	1654	MX-0011	MX-0011	MX-0011	MX-0011	MX-0011	MX-0011	MX-0111	MX-0111
***Anal.* #**	61	62	63	64	65	66	67	68	69	70	71	72
SiO_2	38.14	38.22	39.45	39.86	38.66	38.41	38.07	38.39	38.48	38.63	38.3	37.97
TiO_2	0.09	0.11	0.04	0.04	0.09	0.08	0.06	0.1	0.07	0.06	0.05	0.03
Al_2O_3	21.83	22.14	22.79	22.88	21.87	22.09	21.98	22.13	21.94	21.93	21.67	21.57
Cr_2O_3	0.13	0.17	0.14	0.14	0.07	0.06	0.04	0.05	0.04	0.08	0.08	0.09
FeO	24.2	24.55	18.2	18.4	23.54	23.76	23.49	23.71	23.86	23.39	24.82	24.27
MnO	1.97	2.17	0.48	0.47	0.72	0.74	0.73	0.75	0.71	0.7	1.45	1.57
MgO	4.77	4.33	10.64	11.08	5.37	5.34	5.51	5.38	5.12	5.51	5.15	5.03
CaO	8.56	8.7	7.46	7.04	9.7	9.48	9.34	9.41	9.78	9.66	8.3	8.6
Na_2O	0	0	0	0	0.01	0.01	0.01	0.01	0.02	0	0.01	0.01
Total	99.69	100.39	99.2	99.91	100.02	99.95	99.24	99.94	100.01	99.95	99.82	99.14
12 Oxy												
Si	2.984	2.976	2.979	2.985	2.995	2.98	2.973	2.978	2.987	2.992	2.991	2.986
Ti	0.005	0.006	0.002	0.002	0.005	0.005	0.004	0.006	0.004	0.003	0.003	0.002
Al	2.013	2.032	2.029	2.02	1.997	2.02	2.023	2.024	2.007	2.002	1.995	1.999
Cr	0.008	0.01	0.008	0.008	0.005	0.003	0.003	0.003	0.003	0.005	0.005	0.006
Fe	1.584	1.599	1.149	1.152	1.525	1.542	1.534	1.538	1.549	1.516	1.621	1.596
Mn	0.131	0.143	0.031	0.03	0.047	0.049	0.049	0.049	0.046	0.046	0.096	0.105
Mg	0.556	0.503	1.198	1.237	0.62	0.618	0.642	0.622	0.593	0.636	0.599	0.59
Ca	0.718	0.726	0.604	0.565	0.805	0.788	0.781	0.782	0.813	0.802	0.694	0.725
Na	0	0	0	0	0.001	0.001	0.002	0.001	0.003	0.001	0.001	0.001
Total	8.000	7.996	8	7.999	8.000	8.005	8.011	8.003	8.005	8.001	8.006	8.01
T(°C)	692	651	678	745	634	676	705	741	750	716	751	745

Table B15. Garnet Compositions – EPMA cont.

Sample	MX-0111	MX-0111	MX-0125	MX-0125
***Anal.* #**	73	74	75	76
SiO_2	38.19	38.38	38.45	38.76
TiO_2	0.02	0.04	0.01	0.04
Al_2O_3	21.72	21.74	22	21.69
Cr_2O_3	0.05	0.1	0.07	0.07
FeO	24.27	24.68	24.54	24.4
MnO	1.56	1.58	1.35	1.37
MgO	5.2	5.38	6.18	6.27
CaO	8.54	8.01	7.29	7.23
Na_2O	0	0.01	0	0.01
Total	99.55	99.91	99.87	99.85
12 Oxy				
Si	2.987	2.991	2.985	3.007
Ti	0.001	0.002	0	0.002
Al	2.003	1.998	2.013	1.983
Cr	0.003	0.006	0.004	0.004
Fe	1.588	1.609	1.593	1.583
Mn	0.104	0.104	0.089	0.09
Mg	0.606	0.625	0.715	0.726
Ca	0.716	0.669	0.606	0.601
Na	0	0.001	0	0.002
Total	8.008	8.005	8.006	7.998
T(°C)	753	750	734	753

Appendix C1: Heat Production Data (Mineral)

Here heat production is presented on a per-mineral basis. HPE concentrations are reported as a mean of multiple points (n) on an individual grain (mineral #). Single point measurements have an uncertainty collected from the selected instrument while multiple point measurements present 1 standard deviation of the values. Appendix B2 presents each analytical point for the various minerals. A dash represents an unanalyzed element or unassigned min # for that mineral. Minerals marked with * are likely contaminated and should be taken with suspicion.

Sample #	**Mineral**	**Min #**	**n (K)**	**n (Th, U)**	**K**	**K ±**	**Th**	**Th ±**	**U**	**U ±**
1554	Alkali Feldspar	-	10	0	112229	6047	-	-	-	-
DDM-20	Alkali Feldspar	1	2	1	127650	2275	0.089	0.002	0.047	0.001
DDM-303	Alkali Feldspar	1	5	0	113476	3995	-	-	-	-
1525	Amphibole	2	4	2	16975	663	0.011	0.006	0.01	0.003
1525	Amphibole	1	5	2	18320	686	0.032	0.012	0.018	0.003
1542	Amphibole	1	5	2	19350	337	0.211	0.036	0.012	0.002
1214	Amphibole	2	6	2	19607	434	0.575	0.035	0.045	0.004
1214	Amphibole	1	5	2	19271	531	1.52	0.146	0.076	0.027
MX-0125	Amphibole	2	4	1	14926	204	0.634	0.023	0.041	0.003
MX-0125	Amphibole	1	4	2	14858	177	0.62	0.078	0.063	0.006
1030	Apatite	3	0	1	-	-	10	1.5	0.9	0.31
1140	Apatite	2	0	2	-	-	3.3	0.13	7.9	0.62
1140	Apatite	4	0	1	-	-	18.3	0.34	8.61	0.15
1140	Apatite	3	0	1	-	-	23.6	0.22	9.55	0.14
1140	Apatite	1	0	3	-	-	5.68	1.06	11.5	0.65
1214	Apatite	1	0	3	-	-	6.7	10.4	2.1	3.5
1542	Apatite	1	0	4	-	-	5.52	3.47	0.39	0.1
1542	Apatite	2	0	4	-	-	32.4	20.8	2.7	2.2
1638	Apatite	2	0	2	-	-	13.275	0.163	0.263	0.018
1638	Apatite	1	0	1	-	-	23.2	2.2	4.09	0.35
1030	Apatite	1	0	2	-	-	1.28	0.113	0.35	0.042
1030	Apatite	2	0	2	-	-	8.5	1.27	0.895	0.148
1214	Apatite	2	0	2	-	-	1.89	0.182	0.691	0.304
1525	Apatite	2	0	2	-	-	4.07	0.053	0.114	0.002
1525	Apatite	1	0	3	-	-	0.202	0.0177	0.632	0.022
1554	Apatite	2	0	2	-	-	0.117	0.146	0.929	0.197
1612	Apatite	2	0	2	-	-	17.9	22.5	50.7	69.565
1612	Apatite	1	0	2	-	-	5.33	2.079	67.1	29.769
1612	Apatite	3	0	1	-	-	48.5	0.87	94.9	0.77
DDM-20	Apatite	2	0	1	-	-	0.01	0.00	0.08	0.01

Sample #	Mineral	Min #	n (K)	n (Th, U)	K	K ±	Th	Th ±	U	U ±
DDM-20	Apatite	1	0	1	-	-	0.00	0.00	0.10	0.01
DDM-303	Apatite	1	0	1	-	-	12.86	0.28	0.861	0.052
MX-0011	Apatite	2	0	2	-	-	68.1	0.042	4.9	0.034
MX-0011	Apatite	1	0	2	-	-	51.5	5.64	9.13	0.269
MX-0011	Apatite	3	0	2	-	-	112	5.7	26.1	1.2
MX-0111	Apatite	1	0	2	-	-	0.0426	0.04	0.336	0.122
MX-0111	Apatite	2	0	1	-	-	0.05	0.01	0.391	0.015
MX-0125	Apatite	2	0	2	-	-	10.67	1.174	31.6	0.262
MX-0154	Apatite	1	0	2	-	-	2.365	0.177	2.975	0.191
MX-0154	Apatite	2	0	1	-	-	4.4	0.31	3.5	0.28
1542	Biotite	1	3	0	82926	1048	-	-	-	-
MX-0125	Biotite	1	4	2	84517	621	0.006	0.003	0.006	0.003
MX-0125	Biotite	2	4	1	84111	689	0.020	0.002	0.023	0.002
MX-0154	Biotite	1	4	1	80524	2346	0.030	0.004	0.024	0.002
1030	Clinopyroxene	2	1	3	91.2	4.7	0.120	0.065	0.006	0.003
1030	Clinopyroxene	1	2	2	46.2	36.5	0.087	0.017	0.018	0.005
1140	Clinopyroxene	2	3	1	14.2	19.3	0.322	0.030	0.041	0.010
1525	Clinopyroxene	2	2	1	24.7	10.3	0.212	0.004	0.091	0.057
1525	Clinopyroxene	1	3	1	25	3	0.313	0.010	0.115	0.030
1542	Clinopyroxene	3	0	2	-	-	0.400	0.061	0.021	0.013
1542	Clinopyroxene	1	2	2	246	330.8	0.335	0.023	0.024	0.007
1612	Clinopyroxene	4	2	2	47	25.5	0.106	0.013	0.097	0.002
1612	Clinopyroxene	2	3	3	178	142.9	0.168	0.096	0.169	0.077
1612	Clinopyroxene	3	2	3	80	83.9	0.180	0.042	0.173	0.015
1612	Clinopyroxene	1	2	3	97	28.3	0.221	0.184	0.613	0.817
1638	Clinopyroxene	2	1	1	7.3	1.2	0.072	0.005	0.011	0.002
1638	Clinopyroxene	1	2	2	66.8	86.5	0.236	0.005	0.013	0.001
1140	Clinopyroxene	1	3	0	13	7.53	-	-	-	-
1140	Clinopyroxene	3	1	0	20.6	2.4	-	-	-	-
1140	Clinopyroxene	3	1	0	7.38	0.82	-	-	-	-
1140	Clinopyroxene	3	1	0	2.5	0.19	-	-	-	-
1214	Clinopyroxene	1	2	2	6.6	6.26	0.648	0.361	0.064	0.019
1214	Clinopyroxene	2	2	3	11.9	13	0.763	0.404	0.068	0.032
1638	Clinopyroxene	3	1	0	5	1	-	-	-	-
1654	Clinopyroxene	2	0	3	-	-	0.023	0.004	0.005	0.001
1654	Clinopyroxene	3	0	3	-	-	0.021	0.008	0.005	0.001

Sample #	Mineral	Min #	n (K)	n (Th, U)	K	K ±	Th	Th ±	U	U ±
1654	Clinopyroxene	1	0	3	-	-	0.029	0.015	0.009	0.007
1654	Clinopyroxene	4	1	0	1	0.023	-	-	-	-
1654	Clinopyroxene	5	1	0	51	16	-	-	-	-
MX-0011	Clinopyroxene	1	3	2	46.4	69.8	0.505	0.025	0.064	0.029
MX-0011	Clinopyroxene	3	0	2	-	-	0.433	0.058	0.07	0.013
MX-0011	Clinopyroxene	2	2	2	6.8	0.792	0.651	0.146	0.118	0.01
MX-0111	Clinopyroxene	1	2	2	90.1	43.1	0.26	0.01	0.04	0.01
MX-0111	Clinopyroxene	2	1	2	32.4	5.3	0.32	0.04	0.05	0.03
MX-0125	Clinopyroxene	1	1	1	39.4	5	0.262	0.04	0.07	0.014
MX-0125	Clinopyroxene	2	1	1	1.6	0.32	0.288	0.024	0.079	0.007
MX-0154	Clinopyroxene	2	1	2	3.1	0.6	0.0706	0.001	0.015	0.001
MX-0154	Clinopyroxene	1	2	0	51.1	31	-	-	-	-
1030	Garnet	3	0	3	-	-	<d.l.	<d.l.	<d.l.	<d.l.
1030	Garnet	1	2	3	0.51	0.98	0.002	0.001	0.003	0.001
1030	Garnet	2	2	3	3.32	2.52	0.014	0.004	0.006	0.008
1140	Garnet	2	0	2	-	-	0.015	0.007	0.02	0.009
1140	Garnet	3	3	0	0.13	0.12	-	-	-	-
1542	Garnet	2	0	2	-	-	0.084	0.001	0.014	0.001
1542	Garnet	1	2	2	1.06	1.12	0.201	0.206	0.089	0.105
1554	Garnet	3	0	2	-	-	0.015	0.017	0.003	0.002
1554	Garnet	2	0	3	-	-	0.004	0.002	0.007	0.004
1554	Garnet	1	0	3	-	-	0.003	0.001	0.037	0.054
1554	Garnet	4	5	0	0.24	0.14	-	-	-	-
1554	Garnet	5	2	0	0.66	0.15	-	-	-	-
1612	Garnet	3	2	3	152	180	0.009	0.003	0.106	0.048
1612	Garnet	2	3	3	45	23.2	0.019	0.012	0.109	0.026
1612	Garnet	4	2	3	42	5.7	0.014	0.002	0.124	0.017
1612	Garnet	1	2	3	54	20	0.012	0.002	0.146	0.019
1638	Garnet	1	2	1	1.3	0.9	0.025	0.002	0.001	0
1638	Garnet	2	1	2	1.8	0.4	0.076	0.092	0.015	0.019
1214	Garnet	2	1	2	2.4	0.6	0.023	0.018	0.008	0.009
1214	Garnet	1	1	2	2.4	1.1	0.02	0.002	0.012	0.005
1638	Garnet	3	1	0	0.7	-	-	-	-	-
1654	Garnet	3	0	3	-	-	0.003	0.001	0.001	<dl
1654	Garnet	2	0	4	-	-	0.003	0.002	0.002	0.002
1654	Garnet	1	0	4	-	-	0.001	0.001	0.002	0.002
DDM-20	Garnet	3	0	2	-	-	<d.l.	<d.l.	0.001	<d.l.

Sample #	**Mineral**	**Min #**	**n (K)**	**n (Th, U)**	**K**	**K ±**	**Th**	**Th ±**	**U**	**U ±**
DDM-20	Garnet	2	0	2	-	-	0.006	0.008	0.003	0.003
DDM-20	Garnet	1	0	2	-	-	0.005	0.005	0.003	0
DDM-20	Garnet	4	2	0	0.21	0.14	-	-	-	-
DDM-303	Garnet	1	1	2	7.8	-	0.001	0.002	0.005	0.003
DDM-303	Garnet	3	2	0	4.01	0.191	-	-	-	-
DDM-303	Garnet	2	2	0	3.13	2.65	-	-	-	-
MX-0011	Garnet	1	2	2	0.2	0.297	0.044	0.005	0.022	0.014
MX-0011	Garnet	2	2	1	402*	452	0.099	0.048	0.027	0.008
MX-0011	Garnet	3	0	2	-	-	0.538	0.042	0.551	0.438
MX-0111	Garnet	2	1	1	3.3	0.43	0.0081	0.001	0.009	0.001
MX-0111	Garnet	1	1	1	2	0.41	0.0241	0.001	0.015	0.001
MX-0125	Garnet	1	1	2	97	28	0.011	0.006	0.02	0.004
MX-0125	Garnet	3	1	2	0.6	0.3	0.107	0.129	0.068	0.075
MX-0125	Garnet	2	1	0	0.1	0.1	-	-	-	-
MX-0154	Garnet	2	0	3	<dl	<dl	0.006	0.01	<dl	<dl
MX-0154	Garnet	2	2	3	8.7	4.7	0.07	0.059	0.039	0.029
1140	Ilmenite	1	0	2	-	-	0.014	0.001	0.059	0.014
1140	Ilmenite	2	0	2	-	-	0.025	0.032	0.096	0.072
1554	Monazite	1	0	5	-	-	631	861	736	622
1554	Monazite	2	0	3	-	-	176319	921.25	4186	117
DDM-20	Monazite	1	0	2	-	-	11393	4961	274	176
DDM-20	Monazite	3	0	4	-	-	16242	11877	340	300
DDM-20	Monazite	2	0	3	-	-	23341	27376	554	506
1140	Orthopyroxene	1	0	4	-	-	0.047	0.038	0.014	0.002
1140	Orthopyroxene	3	0	2	-	-	0.073	0.015	0.015	0.001
1140	Orthopyroxene	2	0	1	-	-	0.008	0	0.019	0
1140	Orthopyroxene	4	2	0	13.1	0.72	-	-	-	-
1140	Orthopyroxene	5	2	0	40.4	57	-	-	-	-
1214	Orthopyroxene	2	1	1	15.8	1.5	0.015	0.001	0.0114	0.0005
1214	Orthopyroxene	1	1	1	7.95	0.5	0.03	0.001	0.02	0.001
1525	Orthopyroxene	1	0	1	-	-	0.017	0.001	0.006	0.002
1525	Orthopyroxene	2	0	1	-	-	0.01	0.001	0.01	0.003
1638	Orthopyroxene	1	2	2	2.2	2.8	0.012	0.014	0.001	0.001
1638	Orthopyroxene	2	2	2	11.2	15	0.024	0.006	0.003	0.003
DDM-20	Orthopyroxene	1	1	1	680	130	0.012	0.001	0.001	0.0001
MX-0154	Orthopyroxene	1	1	2	1.8	-	0.09	0.027	0.027	0.006
1030	Plagioclase	1	8	3	3063	87.4	0.212	0.338	0.184	0.304
1030	Plagioclase	3	6	4	3184	76.8	0.27	0.264	0.207	0.231

Sample #	Mineral	Min #	n (K)	n (Th, U)	K	K ±	Th	Th ±	U	U ±
1030	Plagioclase	2	7	3	3115	62.6	0.481	0.19	0.378	0.196
1140	Plagioclase	2	10	4	2794	79	0.279	0.061	0.2	0.032
1140	Plagioclase	1	13	4	2787	127	0.286	0.013	0.215	0.016
1542	Plagioclase	1	4	3	2788	179	0.44	0.22	0.301	0.17
1542	Plagioclase	2	4	5	2540	309	0.553	0.17	0.323	0.03
1554	Plagioclase	2	7	2	2035	1054	0.361	0.026	0.222	0.025
1554	Plagioclase	3	7	2	1499	110	0.34	0.002	0.227	0.024
1554	Plagioclase	1	6	2	2395	1126	0.357	0.009	0.244	0.053
1612	Plagioclase	3	4	3	1616	89.4	0.621	0.493	0.421	0.339
1612	Plagioclase	4	4	3	1039	28	0.649	0.523	0.489	0.412
1612	Plagioclase	2	5	3	3217	1841	0.743	0.007	0.539	0.04
1612	Plagioclase	1	8	3	517	54.7	0.787	0.677	0.57	0.488
1214	Plagioclase	1	5	2	3337	141.3	0.709	0.017	0.516	0.036
1214	Plagioclase	3	6	1	3119	153.7	0.709	0.01	0.52	0.01
1214	Plagioclase	2	5	2	3271	265	0.772	0.058	0.557	0.033
1214	Plagioclase	6	5	0	3066	260.7	-	-	-	-
1214	Plagioclase	5	5	0	3143	73.5	-	-	-	-
1214	Plagioclase	4	3	0	3255	73.7	-	-	-	-
1525	Plagioclase	-	10	7	2580	186	0.555	0.017	0.392	0.01
1542	Plagioclase	3	4	0	2707	51	-	-	-	-
1638	Plagioclase	3	5	3	3636	95.4	0.507	0.005	0.349	0.004
1638	Plagioclase	2	6	3	3233	135	0.553	0.009	0.386	0.003
1638	Plagioclase	1	8	2	3228	144	0.557	0.01	0.391	0
1654	Plagioclase	3	5	5	727	49.5	0.703	0.297	0.457	0.234
1654	Plagioclase	1	5	3	488	46.1	0.971	0.007	0.737	0.128
1654	Plagioclase	2	4	6	557	27.3	0.962	0.05	0.746	0.09
1654	Plagioclase	4	7	3	466	34.1	1	0.012	0.914	0.022
DDM-20	Plagioclase	2	3	1	2413	301	0.287	0.008	0.172	0.003
DDM-20	Plagioclase	3	2	1	2724	43	0.373	0.007	0.192	0.01
DDM-20	Plagioclase	1	4	3	3015	74.2	0.363	0.066	0.239	0.057
DDM-303	Plagioclase	1	6	2	1909	474	0.334	0.007	0.154	0.128
DDM-303	Plagioclase	3	4	2	1591	195	0.282	0.091	0.165	0.105
DDM-303	Plagioclase	2	0	2	-	-	0.378	0.033	0.211	0.034
MX-0011	Plagioclase	3	10	2	2889	488	0.036	0.018	0.06	0.025
MX-0011	Plagioclase	1	12	2	2689	259	0.8	0.13	0.514	0.122
MX-0011	Plagioclase	2	10	2	2871	153	1.38	0.735	0.575	0.007
MX-0111	Plagioclase	1	8	2	2000	140	0.266	0.001	0.234	0.011

Sample #	Mineral	Min #	n (K)	n (Th, U)	K	K ±	Th	Th ±	U	U ±
MX-0111	Plagioclase	2	10	1	2349	190	0.27	0.021	0.242	0.019
MX-0125	Plagioclase	3	4	2	2302	140.7	0.546	0	0.425	0.009
MX-0125	Plagioclase	2	3	2	3823	2516	0.545	0.006	0.455	0.004
MX-0125	Plagioclase	1	4	2	2401	293.6	0.609	0.002	0.54	0.071
MX-0154	Plagioclase	1	10	7	1789	185	0.643	0.011	0.491	0.009
DDM-20	Quartz	1	0	2	-	-	0.088	0.001	0.048	0
1030	Rutile	2	0	1	-	-	<d.l.	-	1.52	0.02
1030	Rutile	1	0	2	-	-	0.004	0.005	1.67	0.018
1525	Rutile	1	0	1	-	-	0.121	0.01	0.135	0.01
1554	Rutile	3	0	1	-	-	<d.l.	<d.l.	4.535	<d.l.
1554	Rutile	1	0	2	-	-	<d.l.	0.276	8.432	1.529
1554	Rutile	2	0	2	-	-	0.01	0.013	24.565	0.247
1638	Rutile	1	0	1	-	-	0.008	0.001	2.68	0.02
1638	Rutile	2	0	1	-	-	0.0526	0.01	3.96	0.03
1542	Rutile	2	0	2	-	-	0.005	0.006	18.5	0.403
1542	Rutile	1	0	2	-	-	0.189	0.242	19.1	1.987
1542	Rutile	3	0	1	-	-	0.087	0.01	19.8	0.21
DDM-20	Rutile	2	0	1	-	-	0.004	0.006	1.4	0.014
DDM-20	Rutile	1	0	1	-	-	<d.l.	-	24.03	0.14
DDM-303	Rutile	2	0	1	-	-	1.64	0.076	31.6	0.069
DDM-303	Rutile	1	0	1	-	-	<d.l.	-	33.4	0.082
DDM-303	Rutile	3	0	1	-	-	0.34	0.053	34.6	0.085
DDM-303	Rutile	4	0	1	-	-	8.05	0.62	39.1	0.11
MX-0011	Rutile	2	0	1	-	-	0.083	0.005	0.701	0.024
MX-0011	Rutile	1	0	2	-	-	0.046	0.011	2.2	0.16
MX-0154	Rutile	1	0	1	-	-	0.326	0.028	0.746	0.025
1638	Scapolite	1	3	1	1495	93	1.12	0.01	0.786	0.02
MX-0011	Titanite	1	0	2	-	-	1.39	1.31	0.355	0.12
MX-0011	Titanite	2	0	2	-	-	13.3	13.2	14	3.28
MX-0154	Titanite	2	2	1	12.5	7.21	7.43	13.23	1.84	3.28
MX-0154	Titanite	1	2	2	18.3	16.5	8.54	0.389	2.57	0.049
1214	Zircon	1	0	2	-	-	156.5	55.9	188	59.4
1554	Zircon	2	0	1	-	-	197	1.4	222	1.5
1554	Zircon	3	0	1	-	-	91	27	239	7.5
1554	Zircon	1	0	1	-	-	198	1.9	217	2.4
DDM-20	Zircon	2	0	2	-	-	18.1	4.3	12.88	2.38
DDM-20	Zircon	1	0	1	-	-	51.24	0.95	59.5	0.99

Sample #	Mineral	Min #	n (K)	n (Th, U)	K	K ±	Th	Th ±	U	U ±
DDM-303	Zircon	2	0	1	-	-	62.1	5.6	53.7	2
DDM-303	Zircon	1	0	1	-	-	1.82	0.13	56.6	1.2
MX-0125	Zircon	1	0	1	-	-	264	2.5	401	2.4

Appendix C2: Individual Mineral Points

The following table is a compilation of the individual analyses which comprise the dataset presented in B1. LA-ICP-MS data is presented with a single value and the analytical 2 standard deviation. Single EMPA points are presented without uncertainty, multiple analyses are presented with standard deviation.

Sample #	*Mineral*	*Min #*	K	K ±	Th	Th ±	U	U ±
1525	Amphibole	2	-	-	0.0066	0.00035	0.0084	0.00034
1542	Amphibole	1	-	-	0.19	0.0058	0.01	0.0018
1525	Amphibole	2	-	-	0.015	0.0011	0.012	0.00056
1542	Amphibole	1	-	-	0.24	0.0059	0.014	0.00064
1525	Amphibole	1	-	-	0.024	0.00068	0.016	0.00035
1525	Amphibole	1	-	-	0.04	0.001	0.02	0.00067
MX-0125	Amphibole	2	-	-	0.63	0.023	0.041	0.0031
1214	Amphibole	2	-	-	0.55	0.031	0.043	0.00091
1214	Amphibole	2	-	-	0.6	0.031	0.048	0.00072
1214	Amphibole	1	-	-	1.4	0.011	0.057	0.0007
MX-0125	Amphibole	1	-	-	0.68	0.032	0.059	0.0011
MX-0125	Amphibole	1	-	-	0.57	0.026	0.067	0.0033
1214	Amphibole	1	-	-	1.6	0.0078	0.095	0.00099
1214	Amphibole	1	19607	434	-	-	-	-
1214	Amphibole	2	19271	531	-	-	-	-
1525	Amphibole	1	18000	95	-	-	-	-
1525	Amphibole	2	17000	95	-	-	-	-
1542	Amphibole	1	19350	337	-	-	-	-
MX-0125	Amphibole	1	83335	-	-	-	-	-
MX-0125	Amphibole	1	83666	-	-	-	-	-
MX-0125	Amphibole	1	84484	-	-	-	-	-
MX-0125	Amphibole	1	84382	-	-	-	-	-
MX-0125	Amphibole	2	83806	-	-	-	-	-
MX-0125	Amphibole	2	84145	-	-	-	-	-
MX-0125	Amphibole	2	83912	-	-	-	-	-

Sample #	*Mineral*	*Min #*	*K*	*K+/-*	*Th*	*Th+/-*	*U*	*U+/-*
MX-0125	Amphibole	2	84391	-	-	-	-	-
1654	Apatite	1	-	-	<d.l.	0.0011	<d.l.	0.0000045
1214	Apatite	1	-	-	0.065	0.0028	0.0092	0.00047
DDM-20	Apatite	2	-	-	0.0061	0.0031	0.079	0.014
DDM-20	Apatite	1	-	-	0.0042	0.0028	0.1	0.0087
1525	Apatite	2	-	-	4	0.11	0.11	0.01
1525	Apatite	2	-	-	4.1	0.092	0.12	0.0085
1214	Apatite	1	-	-	1.3	0.35	0.16	0.046
MX-0111	Apatite	1	-	-	0.071	0.014	0.25	0.006
1638	Apatite	2	-	-	13	0.34	0.25	0.025
1638	Apatite	2	-	-	13	0.34	0.28	0.02
1542	Apatite	1	-	-	2.7	0.11	0.3	0.023
1542	Apatite	1	-	-	2.4	0.16	0.31	0.036
1030	Apatite	1	-	-	1.4	0.14	0.32	0.11
1030	Apatite	1	-	-	1.2	0.15	0.38	0.17
MX-0111	Apatite	2	-	-	0.05	0.01	0.39	0.015
MX-0111	Apatite	1	-	-	0.014	0.00056	0.42	0.0073
1542	Apatite	1	-	-	8.3	0.12	0.46	0.014
1214	Apatite	2	-	-	1.8	0.76	0.48	0.078
1542	Apatite	1	-	-	8.8	0.13	0.48	0.013
MX-0154	Apatite	3	-	-	0.84	0.46	0.5	0.32
1525	Apatite	1	-	-	0.21	0.027	0.62	0.029
1525	Apatite	1	-	-	0.19	0.015	0.65	0.065
1030	Apatite	2	-	-	9.4	1.1	0.79	0.31
1554	Apatite	2	-	-	0.014	0.015	0.79	0.041
DDM-303	Apatite	1	-	-	13	0.28	0.86	0.052
1030	Apatite	3	-	-	10	1.5	0.9	0.31
1214	Apatite	2	-	-	2	0.096	0.91	0.09
1542	Apatite	2	-	-	1.3	0.16	0.95	0.088
1030	Apatite	2	-	-	7.6	1.2	1	0.34
1554	Apatite	2	-	-	0.22	0.18	1.1	0.053
1612	Apatite	2	-	-	2	0.67	1.5	0.48
1542	Apatite	2	-	-	42	0.46	1.9	0.032
1542	Apatite	2	-	-	42	0.33	1.9	0.028
MX-0154	Apatite	1	-	-	2.2	0.17	2.8	0.24
MX-0154	Apatite	1	-	-	2.5	0.12	3.1	0.14

Sample #	*Mineral*	*Min #*	K	K ±	Th	Th ±	U	U ±
MX-0154	Apatite	2	-	-	4.4	0.31	3.5	0.28
1638	Apatite	1	-	-	18	4.3	3.7	0.51
1638	Apatite	1	-	-	23	2.2	4.1	0.35
MX-0011	Apatite	2	-	-	68	0.74	4.9	0.064
MX-0011	Apatite	2	-	-	68	0.96	4.9	0.089
MX-0125	Apatite	1	-	-	2	0.43	5.8	1.1
1542	Apatite	2	-	-	44	0.76	6	0.37
1214	Apatite	1	-	-	19	0.65	6.1	0.31
MX-0125	Apatite	1	-	-	2.3	0.31	6.8	1.6
1140	Apatite	2	-	-	3.2	0.069	7.5	0.085
1140	Apatite	2	-	-	3.4	0.31	8.3	0.27
1140	Apatite	4	-	-	18	0.34	8.6	0.15
MX-0011	Apatite	1	-	-	48	1	8.9	0.18
MX-0011	Apatite	1	-	-	55	0.72	9.3	0.13
1140	Apatite	3	-	-	24	0.22	9.6	0.14
1140	Apatite	1	-	-	5.1	0.071	11	0.12
1140	Apatite	1	-	-	5.1	0.17	12	0.23
1140	Apatite	1	-	-	6.9	1.4	12	0.18
MX-0011	Apatite	3	-	-	110	1.5	25	0.3
MX-0011	Apatite	3	-	-	120	1.7	27	0.36
MX-0125	Apatite	2	-	-	12	0.38	31	0.72
MX-0125	Apatite	2	-	-	9.8	0.54	32	0.71
1612	Apatite	1	-	-	6.8	1.4	46	16
1612	Apatite	1	-	-	3.9	0.14	88	1.2
1612	Apatite	3	-	-	48	0.87	95	0.77
1612	Apatite	2	-	-	34	0.77	100	1.9
MX-0125	Biotite	1	-	-	0.0036	0.00063	0.0034	0.00042
MX-0125	Biotite	1	-	-	0.008	0.0014	0.008	0.0019
MX-0125	Biotite	2	-	-	0.022	0.0019	0.023	0.002
MX-0154	Biotite	1	-	-	0.03	0.0043	0.024	0.0019
1542	Biotite	1	82926	1048	-	-	-	-
MX-0125	Biotite	1	83894	-	-	-	-	-

Sample #	*Mineral*	*Min #*	K	K ±	Th	Th ±	U	U ±
MX-0125	Biotite	1	84316	-	-	-	-	-
MX-0125	Biotite	1	85370	-	-	-	-	-
MX-0125	Biotite	1	84487	-	-	-	-	-
MX-0125	Biotite	2	83892	-	-	-	-	-
MX-0125	Biotite	2	83360	-	-	-	-	-
MX-0125	Biotite	2	84181	-	-	-	-	-
MX-0125	Biotite	2	85010	-	-	-	-	-
MX-0154	Biotite	1	80500	2500	-	-	-	-
1030	Clinopyroxene	2	-	-	0.073	0.0037	0.0024	0.00059
1654	Clinopyroxene	1	-	-	0.015	0.00081	0.0041	0.00034
1654	Clinopyroxene	2	-	-	0.019	0.00099	0.0043	0.00036
1654	Clinopyroxene	3	-	-	0.016	0.0012	0.0045	0.00034
1654	Clinopyroxene	3	-	-	0.018	0.0014	0.0051	0.00055
1654	Clinopyroxene	2	-	-	0.023	0.001	0.0053	0.00036
1654	Clinopyroxene	2	-	-	0.026	0.0014	0.0055	0.00042
1654	Clinopyroxene	3	-	-	0.03	0.0019	0.0058	0.00042
1654	Clinopyroxene	1	-	-	0.027	0.0013	0.0059	0.00044
1030	Clinopyroxene	2	-	-	0.092	0.0042	0.0077	0.00074
1030	Clinopyroxene	2	-	-	0.19	0.013	0.0078	0.0021
1638	Clinopyroxene	2	-	-	0.072	0.0049	0.011	0.0024
1542	Clinopyroxene	3	-	-	0.36	0.016	0.011	0.0012
1638	Clinopyroxene	1	-	-	0.23	0.012	0.013	0.00091
1638	Clinopyroxene	1	-	-	0.24	0.015	0.014	0.0021
MX-0154	Clinopyroxene	2	-	-	0.07	0.0043	0.014	0.0024
1030	Clinopyroxene	1	-	-	0.1	0.004	0.014	0.0011
MX-0154	Clinopyroxene	2	-	-	0.072	0.002	0.015	0.0048
1654	Clinopyroxene	1	-	-	0.045	0.027	0.017	0.01
1542	Clinopyroxene	1	-	-	0.35	0.015	0.019	0.0029
1030	Clinopyroxene	1	-	-	0.075	0.011	0.021	0.0031
1542	Clinopyroxene	1	-	-	0.32	0.011	0.029	0.0033
1542	Clinopyroxene	3	-	-	0.44	0.026	0.03	0.0034
MX-0111	Clinopyroxene	2	-	-	0.29	0.0079	0.031	0.00052
1214	Clinopyroxene	2	-	-	0.68	0.23	0.032	0.0026

Sample #	*Mineral*	*Min #*	K	K ±	Th	Th ±	U	U ±
MX-0111	Clinopyroxene	1	-	-	0.25	0.012	0.033	0.00078
1140	Clinopyroxene	2	-	-	0.32	0.025	0.041	0.013
MX-0011	Clinopyroxene	1	-	-	0.49	0.022	0.043	0.0032
MX-0111	Clinopyroxene	1	-	-	0.27	0.008	0.046	0.0029
1214	Clinopyroxene	1	-	-	0.39	0.031	0.05	0.015
1525	Clinopyroxene	2	-	-	0.21	0.013	0.051	0.024
MX-0011	Clinopyroxene	3	-	-	0.47	0.047	0.061	0.011
MX-0125	Clinopyroxene	1	-	-	0.26	0.04	0.07	0.014
MX-0111	Clinopyroxene	2	-	-	0.35	0.016	0.074	0.01
1214	Clinopyroxene	1	-	-	0.9	0.076	0.077	0.012
MX-0011	Clinopyroxene	3	-	-	0.39	0.047	0.079	0.011
MX-0125	Clinopyroxene	2	-	-	0.29	0.024	0.079	0.0067
1214	Clinopyroxene	2	-	-	0.41	0.033	0.081	0.011
MX-0011	Clinopyroxene	1	-	-	0.52	0.035	0.085	0.0083
1214	Clinopyroxene	2	-	-	1.2	0.087	0.092	0.0017
1612	Clinopyroxene	4	-	-	0.097	0.0029	0.095	0.0032
1612	Clinopyroxene	2	-	-	0.067	0.003	0.095	0.0039
1612	Clinopyroxene	4	-	-	0.12	0.0095	0.098	0.0077
MX-0011	Clinopyroxene	2	-	-	0.55	0.022	0.11	0.0058
1525	Clinopyroxene	1	-	-	0.31	0.014	0.12	0.031
MX-0011	Clinopyroxene	2	-	-	0.75	0.02	0.13	0.0046
1525	Clinopyroxene	2	-	-	0.21	0.013	0.13	0.023
1612	Clinopyroxene	1	-	-	0.14	0.006	0.13	0.004
1612	Clinopyroxene	1	-	-	0.091	0.003	0.15	0.0099
1612	Clinopyroxene	3	-	-	0.18	0.005	0.16	0.0065
1612	Clinopyroxene	2	-	-	0.18	0.0051	0.16	0.0042
1612	Clinopyroxene	3	-	-	0.22	0.012	0.17	0.013
1612	Clinopyroxene	3	-	-	0.14	0.021	0.19	0.03
1612	Clinopyroxene	2	-	-	0.26	0.0067	0.25	0.0059
1612	Clinopyroxene	1	-	-	0.43	0.016	1.6	0.075
1612	Clinopyroxene	1	120	16	-	-	-	-
1612	Clinopyroxene	1	77	11	-	-	-	-
1612	Clinopyroxene	2	340	13	-	-	-	-
1612	Clinopyroxene	2	120	79	-	-	-	-

Sample #	*Mineral*	*Min #*	K	K ±	Th	Th ±	U	U ±
1612	Clinopyroxene	2	71	14	-	-	-	-
1612	Clinopyroxene	3	140	7.6	-	-	-	-
1612	Clinopyroxene	3	20	5.1	-	-	-	-
1612	Clinopyroxene	4	65	10	-	-	-	-
1612	Clinopyroxene	4	29	17	-	-	-	-
1030	Clinopyroxene	1	72	14	-	-	-	-
1030	Clinopyroxene	1	20	3	-	-	-	-
1030	Clinopyroxene	2	91	4.7	-	-	-	-
1140	Clinopyroxene	1	19	0.65	-	-	-	-
1140	Clinopyroxene	1	15	0.55	-	-	-	-
1140	Clinopyroxene	1	4.7	0.25	-	-	-	-
1140	Clinopyroxene	2	28	0.96	-	-	-	-
1140	Clinopyroxene	2	<d.l.	0.21	-	-	-	-
1214	Clinopyroxene	1	11	0.71	-	-	-	-
1214	Clinopyroxene	1	2.2	0.17	-	-	-	-
1214	Clinopyroxene	2	21	1.8	-	-	-	-
1214	Clinopyroxene	2	2.7	0.19	-	-	-	-
1525	Clinopyroxene	1	29	1.9	-	-	-	-
1525	Clinopyroxene	1	24	0.42	-	-	-	-
1525	Clinopyroxene	1	23	1.4	-	-	-	-
1525	Clinopyroxene	2	32	3.6	-	-	-	-
1525	Clinopyroxene	2	17	0.48	-	-	-	-
1542	Clinopyroxene	1	480	33	-	-	-	-
1542	Clinopyroxene	1	12	0.66	-	-	-	-
1638	Clinopyroxene	1	130	36	-	-	-	-
1638	Clinopyroxene	1	5.6	1.6	-	-	-	-
1638	Clinopyroxene	2	7.3	1.2	-	-	-	-
1638	Clinopyroxene	3	5	1	-	-	-	-
MX-0011	Clinopyroxene	1	130	70	-	-	-	-
MX-0011	Clinopyroxene	1	6.9	2.3	-	-	-	-
MX-0011	Clinopyroxene	1	5.2	0.24	-	-	-	-
MX-0011	Clinopyroxene	2	7.4	0.35	-	-	-	-
MX-0011	Clinopyroxene	2	6.3	0.36	-	-	-	-
MX-0111	Clinopyroxene	1	120	7.8	-	-	-	-
MX-0111	Clinopyroxene	1	60	3.4	-	-	-	-

Sample #	*Mineral*	*Min #*	K	K ±	Th	Th ±	U	U ±
MX-0111	Clinopyroxene	2	32	5.3	-	-	-	-
MX-0125	Clinopyroxene	1	39	5	-	-	-	-
MX-0125	Clinopyroxene	2	1.6	0.32	-	-	-	-
MX-0154	Clinopyroxene	1	73	10	-	-	-	-
MX-0154	Clinopyroxene	1	29	4.3	-	-	-	-
MX-0154	Clinopyroxene	2	3.1	0.62	-	-	-	-
MX-0154	Garnet	1	-	-	<d.l.	0.000064	<d.l.	0.000044
MX-0154	Garnet	1	-	-	<d.l.	0.00011	<d.l.	0.000093
1654	Garnet	1	-	-	<d.l.	0.000071	<d.l.	0.000078
DDM-20	Garnet	2	-	-	<d.l.	0.00013	<d.l.	0.00009
1654	Garnet	1	-	-	<d.l.	0.00024	<d.l.	0.00015
1654	Garnet	2	-	-	0.0011	0.00035	<d.l.	0.00032
1654	Garnet	2	-	-	0.003	0.0012	<d.l.	0.00032
1030	Garnet	2	-	-	0.015	0.0024	<d.l.	0.00023
1654	Garnet	2	-	-	0.0028	0.00048	<d.l.	0.00014
MX-0154	Garnet	1	-	-	0.017	0.00081	<d.l.	0.00011
1654	Garnet	3	-	-	0.0028	0.00093	<d.l.	0.00025
DDM-20	Garnet	3	-	-	<d.l.	0.000058	<d.l.	0.00011
1030	Garnet	2	-	-	0.017	0.0019	<d.l.	0.00025
1654	Garnet	3	-	-	0.0022	0.0005	0.001	0.00021
1030	Garnet	1	-	-	<d.l.	0.00023	0.0013	0.00022
1030	Garnet	3	-	-	0.0013	0.00034	0.0013	0.00022
1638	Garnet	1	-	-	0.025	0.0021	0.0014	0.00028
DDM-20	Garnet	3	-	-	<d.l.	0.000086	0.0015	0.00017
1654	Garnet	3	-	-	0.0042	0.00053	0.0016	0.00026
1214	Garnet	2	-	-	0.01	0.00077	0.0017	0.00017
1638	Garnet	2	-	-	0.01	0.00069	0.002	0.00017
1030	Garnet	3	-	-	0.0015	0.00049	0.002	0.0004
1554	Garnet	3	-	-	0.0027	0.0021	0.0021	0.00066
1030	Garnet	3	-	-	0.0013	0.00029	0.0021	0.00028
1554	Garnet	2	-	-	0.0021	0.0013	0.0028	0.00058
1654	Garnet	1	-	-	0.0013	0.00027	0.003	0.0003
DDM-20	Garnet	1	-	-	0.0015	0.00017	0.0032	0.00031
DDM-303	Garnet	1	-	-	0.0028	0.00017	0.0035	0.00029

Sample #	*Mineral*	*Min #*	K	K ±	Th	Th ±	U	U ±
1030	Garnet	1	-	-	0.0022	0.00047	0.0037	0.00049
DDM-20	Garnet	1	-	-	0.0082	0.0011	0.0037	0.00082
1030	Garnet	1	-	-	0.0021	0.00063	0.0037	0.0007
1554	Garnet	1	-	-	0.003	0.0026	0.0046	0.00078
1654	Garnet	2	-	-	0.0063	0.00054	0.0047	0.00041
1554	Garnet	3	-	-	0.027	0.023	0.0047	0.004
1654	Garnet	1	-	-	0.0022	0.00052	0.0052	0.00045
DDM-20	Garnet	2	-	-	0.012	0.0086	0.0053	0.0009
1554	Garnet	1	-	-	0.0016	0.0006	0.007	0.0021
DDM-303	Garnet	1	-	-	<d.l.	0.000045	0.0074	0.00039
1554	Garnet	2	-	-	0.0027	0.0024	0.0076	0.001
1214	Garnet	1	-	-	0.019	0.0025	0.0085	0.0012
MX-0111	Garnet	2	-	-	0.0081	0.00079	0.0093	0.001
1554	Garnet	2	-	-	0.0065	0.0057	0.011	0.0028
MX-0011	Garnet	1	-	-	0.04	0.0023	0.012	0.0036
MX-0154	Garnet	2	-	-	0.01	0.0033	0.012	0.0027
1542	Garnet	2	-	-	0.083	0.0081	0.013	0.0025
1140	Garnet	2	-	-	0.011	0.0034	0.013	0.00088
1542	Garnet	2	-	-	0.085	0.015	0.015	0.0047
MX-0125	Garnet	3	-	-	0.015	0.0029	0.015	0.0019
1140	Garnet	1	-	-	0.017	0.0053	0.015	0.0014
1214	Garnet	2	-	-	0.036	0.0092	0.015	0.0041
1542	Garnet	1	-	-	0.056	0.006	0.015	0.0025
1030	Garnet	2	-	-	0.009	0.001	0.015	0.0016
MX-0111	Garnet	1	-	-	0.024	0.0013	0.015	0.00097
1214	Garnet	1	-	-	0.022	0.0035	0.016	0.0015
MX-0125	Garnet	1	-	-	0.015	0.0038	0.017	0.0027
MX-0125	Garnet	1	-	-	0.0066	0.00073	0.023	0.012
1140	Garnet	2	-	-	0.02	0.015	0.026	0.013
MX-0011	Garnet	2	-	-	0.099	0.048	0.027	0.0084
1638	Garnet	2	-	-	0.14	0.0084	0.029	0.0095
MX-0011	Garnet	1	-	-	0.047	0.015	0.031	0.0089
MX-0154	Garnet	2	-	-	0.072	0.01	0.036	0.0058
1140	Garnet	1	-	-	0.042	0.019	0.045	0.032

Sample #	*Mineral*	*Min #*	K	K ±	Th	Th ±	U	U ±
MX-0154	Garnet	2	-	-	0.13	0.029	0.069	0.018
1612	Garnet	3	-	-	0.0088	0.00099	0.074	0.002
1612	Garnet	3	-	-	0.0058	0.00063	0.083	0.0016
1612	Garnet	2	-	-	0.013	0.0018	0.094	0.0031
1612	Garnet	2	-	-	0.01	0.0015	0.094	0.0038
1554	Garnet	1	-	-	0.0041	0.0025	0.1	0.0069
1612	Garnet	4	-	-	0.013	0.0011	0.11	0.0025
MX-0125	Garnet	3	-	-	0.2	0.027	0.12	0.014
1612	Garnet	1	-	-	0.0098	0.00084	0.12	0.0043
1612	Garnet	4	-	-	0.016	0.0011	0.12	0.0023
1612	Garnet	2	-	-	0.033	0.0083	0.14	0.022
1612	Garnet	4	-	-	0.013	0.0012	0.14	0.0043
1612	Garnet	1	-	-	0.013	0.0012	0.16	0.0027
1612	Garnet	1	-	-	0.013	0.0011	0.16	0.0031
1612	Garnet	3	-	-	0.013	0.00089	0.16	0.0035
1542	Garnet	1	-	-	0.35	0.031	0.16	0.017
MX-0011	Garnet	3	-	-	0.51	0.046	0.24	0.022
MX-0011	Garnet	3	-	-	0.57	0.064	0.86	0.16
1612	Garnet	1	68	3	-	-	-	-
1612	Garnet	1	39	1.5	-	-	-	-
1612	Garnet	2	71	5.5	-	-	-	-
1612	Garnet	2	38	11	-	-	-	-
1612	Garnet	2	26	1.2	-	-	-	-
1612	Garnet	3	280	24	-	-	-	-
1612	Garnet	3	24	1.1	-	-	-	-
1612	Garnet	4	46	15	-	-	-	-
1612	Garnet	4	38	8	-	-	-	-
1030	Garnet	1	1.2	1	-	-	-	-
1030	Garnet	1	<d.l.	0.26	-	-	-	-
1030	Garnet	2	5.1	1.9	-	-	-	-
1030	Garnet	2	1.5	0.65	-	-	-	-
1140	Garnet	1	1.1	0.24	-	-	-	-
1140	Garnet	1	<d.l.	0.22	-	-	-	-
1140	Garnet	1	<d.l.	0.24	-	-	-	-
1214	Garnet	1	2.4	1.1	-	-	-	-
1214	Garnet	2	2.4	0.63	-	-	-	-
1542	Garnet	1	1.9	0.37	-	-	-	-

Sample #	*Mineral*	*Min #*	K	K ±	Th	Th ±	U	U ±
1542	Garnet	1	<d.l.	0.17	-	-	-	-
1638	Garnet	1	1.9	2.7	-	-	-	-
1638	Garnet	1	0.65	0.39	-	-	-	-
1638	Garnet	2	1.8	0.42	-	-	-	-
1638	Garnet	3	<d.l.	0.52	-	-	-	-
DDM-303	Garnet	1	7.8	3.3	-	-	-	-
DDM-303	Garnet	2	5	1.4	-	-	-	-
DDM-303	Garnet	2	1.3	0.35	-	-	-	-
DDM-303	Garnet	3	4.1	0.88	-	-	-	-
DDM-303	Garnet	3	3.9	0.75	-	-	-	-
MX-0011	Garnet	1	<d.l.	0.17	-	-	-	-
MX-0011	Garnet	1	<d.l.	0.2	-	-	-	-
MX-0011	Garnet	2	720	36	-	-	-	-
MX-0011	Garnet	2	82	8.6	-	-	-	-
MX-0111	Garnet	1	2	0.41	-	-	-	-
MX-0111	Garnet	2	3.3	0.43	-	-	-	-
MX-0125	Garnet	1	97	28	-	-	-	-
MX-0125	Garnet	2	<d.l.	0.098	-	-	-	-
MX-0125	Garnet	3	<d.l.	0.25	-	-	-	-
MX-0154	Garnet	1	<d.l.	0.32	-	-	-	-
MX-0154	Garnet	1	<d.l.	0.42	-	-	-	-
MX-0154	Garnet	2	12	2.6	-	-	-	-
MX-0154	Garnet	2	5.3	1.1	-	-	-	-
1140	Ilmenite	2	-	-	0.0027	0.0014	0.045	0.0023
1140	Ilmenite	1	-	-	0.014	0.0024	0.049	0.0039
1140	Ilmenite	1	-	-	0.013	0.0039	0.069	0.0042
1140	Ilmenite	2	-	-	0.048	0.0043	0.15	0.0081
DDM-20	Alkali Feldspar	1	-	-	0.089	0.0017	0.047	0.0013
1554	Alkali Feldspar	-	110000	-	-	-	-	-
1554	Alkali Feldspar	-	110000	-	-	-	-	-
1554	Alkali Feldspar	-	110000	-	-	-	-	-

Sample #	*Mineral*	*Min #*	K	K ±	Th	Th ±	U	U ±
1554	Alkali Feldspar	-	110000	-	-	-	-	-
1554	Alkali Feldspar	-	110000	-	-	-	-	-
1554	Alkali Feldspar	-	110000	-	-	-	-	-
1554	Alkali Feldspar	-	110000	-	-	-	-	-
1554	Alkali Feldspar	-	120000	-	-	-	-	-
1554	Alkali Feldspar	-	120000	-	-	-	-	-
1554	Alkali Feldspar	-	120000	-	-	-	-	-
DDM-303	Alkali Feldspar	-	110000	-	-	-	-	-
DDM-303	Alkali Feldspar	-	110000	-	-	-	-	-
DDM-303	Alkali Feldspar	-	110000	-	-	-	-	-
DDM-303	Alkali Feldspar	-	120000	-	-	-	-	-
DDM-303	Alkali Feldspar	-	120000	-	-	-	-	-
1554	Monazite	4	-	-	22698.5	-	<d.l.	-
DDM-20	Monazite	2	-	-	3707.23	-	<d.l.	-
DDM-20	Monazite	3	-	-	4969.54	-	<d.l.	-
DDM-20	Monazite	4	-	-	6217.44	-	<d.l.	-
DDM-20	Monazite	2	-	-	18000	-	260	-
DDM-20	Monazite	1	-	-		-	280	-
1554	Monazite	1	-	-	<d.l.	-	290	-
1554	Monazite	3	-	-		-	320	-
1554	Monazite	4	-	-	<d.l.	-	360	-
DDM-20	Monazite	3	-	-	11000	-	390	-
DDM-20	Monazite	1	-	-	10000	-	410	-
DDM-20	Monazite	1	-	-	29000	-	450	-
DDM-20	Monazite	3	-	-	12000	-	550	-
DDM-20	Monazite	2	-	-	15000	-	570	-
DDM-20	Monazite	1	-	-	55000	-	1100	-
1554	Monazite	1	-	-	1700	-	1100	-
DDM-20	Monazite	4	-	-	12000	-	1200	-
1554	Monazite	2	-	-	1500	-	1700	-
1554	Monazite	3	-	-	180000	-	4100	-
DDM-20	Monazite	1	-	-	180000	-	4200	-
1554	Monazite	2	-	-	180000	-	4300	-
1638	Orthopyroxene	1	-	-	0.0022	0.00068	<d.l.	0.00032
DDM-20	Orthopyroxene	1	-	-	0.012	0.00075	0.0012	0.00011
1638	Orthopyroxene	2	-	-	0.02	0.001	0.0013	0.00063

Sample #	*Mineral*	*Min #*	K	K ±	Th	Th ±	U	U ±
1638	Orthopyroxene	1	-	-	0.023	0.0018	0.0017	0.00067
1638	Orthopyroxene	2	-	-	0.028	0.0014	0.0052	0.0011
1525	Orthopyroxene	1	-	-	0.017	0.0011	0.0055	0.0022
1525	Orthopyroxene	2	-	-	0.0096	0.001	0.01	0.0026
1140	Orthopyroxene	1	-	-	0.01	0.0012	0.011	0.00077
1214	Orthopyroxene	2	-	-	0.015	0.0007	0.011	0.00046
1140	Orthopyroxene	1	-	-	0.075	0.0034	0.013	0.0012
1140	Orthopyroxene	3	-	-	0.084	0.013	0.014	0.0017
DDM-20	Orthopyroxene	2	-	-	0.025	0.00062	0.015	0.00031
1140	Orthopyroxene	1	-	-	0.084	0.013	0.015	0.0084
1140	Orthopyroxene	1	-	-	0.02	0.01	0.016	0.0031
1140	Orthopyroxene	3	-	-	0.063	0.0044	0.016	0.0012
1214	Orthopyroxene	1	-	-	0.026	0.0013	0.018	0.0012
1140	Orthopyroxene	2	-	-	0.0078	0.003	0.019	0.0039
MX-0154	Orthopyroxene	1	-	-	0.072	0.0028	0.023	0.0012
MX-0154	Orthopyroxene	1	-	-	0.11	0.0062	0.031	0.0045
1214	Orthopyroxene	1	8	0.5	-	-	-	-
1140	Orthopyroxene	4	6.9	0.33	-	-	-	-
1140	Orthopyroxene	4	19.4	1.1	-	-	-	-
1140	Orthopyroxene	5	0.25	0.12	-	-	-	-
1140	Orthopyroxene	5	80.6	2.2	-	-	-	-
1214	Orthopyroxene	2	16	1.5	-	-	-	-
1638	Orthopyroxene	1	4.1	0.76	-	-	-	-
1638	Orthopyroxene	1	<d.l.	0.27	-	-	-	-
1638	Orthopyroxene	2	0.39	0.23	-	-	-	-
1638	Orthopyroxene	2	22	3.2	-	-	-	-
DDM-20	Orthopyroxene*	1	680	130	-	-	-	-
MX-0154	Orthopyroxene	1	1.8	0.52	-	-	-	-
1030	Plagioclase	1	-	-	0.0025	0.00062	<d.l.	0.00037
1612	Plagioclase	1	-	-	0.0056	0.0046	0.0065	0.003
1542	Plagioclase	1	-	-	0.039	0.0041	0.0071	0.0011
1030	Plagioclase	1	-	-	0.032	0.016	0.016	0.0083
1030	Plagioclase	3	-	-	0.034	0.022	0.018	0.012
1612	Plagioclase	3	-	-	0.052	0.037	0.029	0.018
1612	Plagioclase	4	-	-	0.057	0.0068	0.032	0.003
MX-0011	Plagioclase	3	-	-	0.023	0.0015	0.043	0.0016
1030	Plagioclase	3	-	-	0.085	0.018	0.058	0.011

Sample #	*Mineral*	*Min #*	K	K ±	Th	Th ±	U	U ±
DDM-303	Plagioclase	1	-	-	0.33	0.036	0.064	0.0034
MX-0011	Plagioclase	3	-	-	0.048	0.0042	0.078	0.0032
1654	Plagioclase	3	-	-	0.22	0.0074	0.091	0.0017
DDM-303	Plagioclase	3	-	-	0.22	0.0074	0.091	0.0017
1542	Plagioclase	2	-	-	0.25	0.027	0.13	0.011
1030	Plagioclase	2	-	-	0.26	0.027	0.15	0.016
1140	Plagioclase	2	-	-	0.2	0.0069	0.15	0.006
DDM-20	Plagioclase	3	-	-	0.27	0.0078	0.15	0.0019
DDM-20	Plagioclase	2	-	-	0.29	0.0078	0.17	0.0025
DDM-20	Plagioclase	1	-	-	0.29	0.009	0.17	0.0035
DDM-303	Plagioclase	2	-	-	0.36	0.012	0.19	0.0071
DDM-20	Plagioclase	3	-	-	0.37	0.0072	0.19	0.01
1140	Plagioclase	1	-	-	0.27	0.012	0.2	0.0092
1554	Plagioclase	2	-	-	0.34	0.007	0.2	0.0054
1554	Plagioclase	1	-	-	0.35	0.0081	0.21	0.0061
1140	Plagioclase	1	-	-	0.3	0.012	0.21	0.01
1140	Plagioclase	2	-	-	0.34	0.0079	0.21	0.0059
1554	Plagioclase	3	-	-	0.34	0.0085	0.21	0.0055
1140	Plagioclase	2	-	-	0.28	0.01	0.22	0.0074
1140	Plagioclase	2	-	-	0.29	0.0078	0.22	0.0071
1140	Plagioclase	1	-	-	0.29	0.0072	0.22	0.0066
1030	Plagioclase	3	-	-	0.36	0.036	0.23	0.024
MX-0111	Plagioclase	1	-	-	0.27	0.016	0.23	0.0097
1140	Plagioclase	1	-	-	0.28	0.0093	0.23	0.0094
DDM-303	Plagioclase	2	-	-	0.4	0.017	0.24	0.0038
DDM-303	Plagioclase	3	-	-	0.35	0.0036	0.24	0.0027
1554	Plagioclase	2	-	-	0.38	0.0089	0.24	0.0059
MX-0111	Plagioclase	1	-	-	0.27	0.015	0.24	0.021
MX-0111	Plagioclase	2	-	-	0.27	0.021	0.24	0.019
DDM-303	Plagioclase	1	-	-	0.34	0.0027	0.24	0.0021
1554	Plagioclase	3	-	-	0.34	0.0079	0.24	0.0064
DDM-20	Plagioclase	1	-	-	0.39	0.0073	0.27	0.0085
DDM-20	Plagioclase	1	-	-	0.41	0.0068	0.28	0.0055
1554	Plagioclase	1	-	-	0.36	0.01	0.28	0.0094

Sample #	*Mineral*	*Min #*	K	K ±	Th	Th ±	U	U ±
1542	Plagioclase	2	-	-	0.57	0.067	0.34	0.03
1638	Plagioclase	0	-	-	0.51	0.0043	0.35	0.0036
1638	Plagioclase	0	-	-	0.51	0.0078	0.35	0.0044
1542	Plagioclase	2	-	-	0.53	0.0034	0.35	0.004
1638	Plagioclase	0	-	-	0.5	0.0069	0.35	0.0035
1542	Plagioclase	2	-	-	0.5	0.011	0.36	0.011
1654	Plagioclase	3	-	-	0.62	0.067	0.36	0.035
1542	Plagioclase	1	-	-	0.53	0.012	0.37	0.012
1525	Plagioclase	0	-	-	0.54	0.0052	0.38	0.0046
1638	Plagioclase	0	-	-	0.56	0.0075	0.38	0.0044
1525	Plagioclase	0	-	-	0.53	0.0066	0.38	0.0055
1638	Plagioclase	0	-	-	0.56	0.0093	0.39	0.007
1525	Plagioclase	0	-	-	0.57	0.0078	0.39	0.0042
1638	Plagioclase	0	-	-	0.54	0.0085	0.39	0.0059
1525	Plagioclase	0	-	-	0.54	0.0082	0.39	0.006
1638	Plagioclase	0	-	-	0.55	0.0063	0.39	0.0058
1638	Plagioclase	0	-	-	0.56	0.0063	0.39	0.0055
1525	Plagioclase	0	-	-	0.56	0.0053	0.4	0.0054
1542	Plagioclase	1	-	-	0.52	0.032	0.4	0.023
1525	Plagioclase	0	-	-	0.58	0.015	0.4	0.031
1525	Plagioclase	0	-	-	0.57	0.0087	0.4	0.0075
MX-0125	Plagioclase	0	-	-	0.55	0.0031	0.42	0.007
MX-0011	Plagioclase	1	-	-	0.71	0.077	0.43	0.021
1542	Plagioclase	2	-	-	0.93	0.35	0.43	0.066
MX-0125	Plagioclase	0	-	-	0.55	0.0065	0.43	0.0091
MX-0125	Plagioclase	0	-	-	0.55	0.011	0.45	0.016
MX-0125	Plagioclase	0	-	-	0.54	0.011	0.46	0.017
MX-0154	Plagioclase	0	-	-	0.66	0.027	0.48	0.016
MX-0154	Plagioclase	0	-	-	0.63	0.013	0.48	0.01
1030	Plagioclase	2	-	-	0.57	0.025	0.48	0.019
MX-0154	Plagioclase	0	-	-	0.63	0.0058	0.49	0.0054
MX-0154	Plagioclase	0	-	-	0.63	0.0078	0.49	0.006
MX-0125	Plagioclase	0	-	-	0.61	0.0073	0.49	0.015
1214	Plagioclase	1	-	-	0.7	0.015	0.49	0.014

Sample #	*Mineral*	*Min #*	K	K ±	Th	Th ±	U	U ±
MX-0154	Plagioclase	0	-	-	0.65	0.01	0.5	0.0066
1030	Plagioclase	2	-	-	0.61	0.011	0.5	0.02
MX-0154	Plagioclase	0	-	-	0.65	0.0069	0.5	0.01
MX-0154	Plagioclase	0	-	-	0.64	0.0073	0.5	0.008
1612	Plagioclase	2	-	-	0.75	0.026	0.51	0.025
1214	Plagioclase	3	-	-	0.71	0.0082	0.52	0.0099
1612	Plagioclase	2	-	-	0.74	0.025	0.52	0.016
1030	Plagioclase	3	-	-	0.6	0.015	0.53	0.026
1214	Plagioclase	2	-	-	0.73	0.011	0.53	0.0092
1030	Plagioclase	1	-	-	0.6	0.015	0.53	0.016
1214	Plagioclase	1	-	-	0.72	0.012	0.54	0.015
1654	Plagioclase	3	-	-	0.89	0.036	0.56	0.039
MX-0011	Plagioclase	2	-	-	0.86	0.2	0.57	0.13
MX-0011	Plagioclase	2	-	-	1.9	1.3	0.58	0.17
1214	Plagioclase	2	-	-	0.81	0.01	0.58	0.0099
1612	Plagioclase	2	-	-	0.74	0.017	0.59	0.024
MX-0125	Plagioclase	0	-	-	0.61	0.016	0.59	0.12
MX-0011	Plagioclase	1	-	-	0.89	0.23	0.6	0.19
1612	Plagioclase	4	-	-	0.84	0.064	0.6	0.054
1612	Plagioclase	3	-	-	0.91	0.02	0.61	0.026
1654	Plagioclase	3	-	-	0.87	0.016	0.62	0.011
1612	Plagioclase	3	-	-	0.9	0.012	0.63	0.011
1654	Plagioclase	2	-	-	0.92	0.015	0.63	0.01
1654	Plagioclase	2	-	-	0.9	0.028	0.64	0.014
1654	Plagioclase	3	-	-	0.92	0.019	0.65	0.023
1654	Plagioclase	1	-	-	0.97	0.021	0.66	0.01
1654	Plagioclase	1	-	-	0.97	0.025	0.67	0.016
1654	Plagioclase	2	-	-	0.98	0.015	0.77	0.019
1654	Plagioclase	2	-	-	0.97	0.013	0.78	0.015
1654	Plagioclase	2	-	-	1	0.018	0.83	0.015
1612	Plagioclase	4	-	-	1	0.021	0.83	0.02
1654	Plagioclase	2	-	-	0.97	0.016	0.83	0.02
1612	Plagioclase	1	-	-	1.2	0.029	0.85	0.024
1612	Plagioclase	1	-	-	1.2	0.029	0.85	0.025
1654	Plagioclase	1	-	-	0.98	0.016	0.88	0.025
1654	Plagioclase	4	-	-	1	0.015	0.89	0.024

Sample #	*Mineral*	*Min #*	K	K ±	Th	Th ±	U	U ±
1654	Plagioclase	4	-	-	0.99	0.023	0.93	0.018
1654	Plagioclase	4	-	-	1	0.017	0.93	0.023
1030	Plagioclase	1	3063	87.4	-	-	-	-
1030	Plagioclase	3	3184	76.8	-	-	-	-
1030	Plagioclase	2	3115	62.6	-	-	-	-
1140	Plagioclase	2	2794	79	-	-	-	-
1140	Plagioclase	1	2787	127	-	-	-	-
1542	Plagioclase	1	2788	179	-	-	-	-
1542	Plagioclase	2	2540	309	-	-	-	-
1554	Plagioclase	2	2035	1054	-	-	-	-
1554	Plagioclase	3	1499	110	-	-	-	-
1554	Plagioclase	1	2395	1126	-	-	-	-
1612	Plagioclase	3	1616	89.4	-	-	-	-
1612	Plagioclase	4	1039	28	-	-	-	-
1612	Plagioclase	2	3217	1841	-	-	-	-
1612	Plagioclase	1	517	54.7	-	-	-	-
1214	Plagioclase	1	3337	141.3	-	-	-	-
1214	Plagioclase	3	3119	153.7	-	-	-	-
1214	Plagioclase	2	3271	265	-	-	-	-
1214	Plagioclase	6	3066	260.7	-	-	-	-
1214	Plagioclase	5	3143	73.5	-	-	-	-
1214	Plagioclase	4	3255	73.7	-	-	-	-
1525	Plagioclase	-	2580	186	-	-	-	-
1542	Plagioclase	3	2707	51	-	-	-	-
1638	Plagioclase	3	3636	95.4	-	-	-	-
1638	Plagioclase	2	3233	135	-	-	-	-
1638	Plagioclase	1	3228	144	-	-	-	-
1654	Plagioclase	3	727	49.5	-	-	-	-
1654	Plagioclase	1	488	46.1	-	-	-	-
1654	Plagioclase	2	557	27.3	-	-	-	-
1654	Plagioclase	4	466	34.1	-	-	-	-
DDM-20	Plagioclase	2	2413	301	-	-	-	-
DDM-20	Plagioclase	3	2724	43	-	-	-	-
DDM-20	Plagioclase	1	3015	74.2	-	-	-	-
DDM-303	Plagioclase	1	1909	474	-	-	-	-
DDM-303	Plagioclase	3	1591	195	-	-	-	-
DDM-303	Plagioclase	2	-	-	-	-	-	-

Sample #	*Mineral*	*Min #*	K	K ±	Th	Th ±	U	U ±
MX-0011	Plagioclase	3	2889	488	-	-	-	-
MX-0011	Plagioclase	1	2689	259	-	-	-	-
MX-0011	Plagioclase	2	2871	153	-	-	-	-
MX-0111	Plagioclase	1	2000	140	-	-	-	-
MX-0111	Plagioclase	2	2349	190	-	-	-	-
MX-0125	Plagioclase	3	2302	140.7	-	-	-	-
MX-0125	Plagioclase	2	3823	2516	-	-	-	-
MX-0125	Plagioclase	1	2401	293.6	-	-	-	-
MX-0154	Plagioclase	1	1789	185	-	-	-	-
1030	Plagioclase	1	3063	87.4	-	-	-	-
1030	Plagioclase	3	3184	76.8	-	-	-	-
1030	Plagioclase	2	3115	62.6	-	-	-	-
1140	Plagioclase	2	2794	79	-	-	-	-
1140	Plagioclase	1	2787	127	-	-	-	-
1542	Plagioclase	1	2788	179	-	-	-	-
1542	Plagioclase	2	2540	309	-	-	-	-
1554	Plagioclase	2	2035	1054	-	-	-	-
1554	Plagioclase	3	1499	110	-	-	-	-
1554	Plagioclase	1	2395	1126	-	-	-	-
1612	Plagioclase	3	1616	89.4	-	-	-	-
1612	Plagioclase	4	1039	28	-	-	-	-
1612	Plagioclase	2	3217	1841	-	-	-	-
1612	Plagioclase	1	517	54.7	-	-	-	-
1214	Plagioclase	1	3337	141.3	-	-	-	-
1214	Plagioclase	3	3119	153.7	-	-	-	-
1214	Plagioclase	2	3271	265	-	-	-	-
1214	Plagioclase	6	3066	260.7	-	-	-	-
1214	Plagioclase	5	3143	73.5	-	-	-	-
1214	Plagioclase	4	3255	73.7	-	-	-	-
1525	Plagioclase	-	2580	186	-	-	-	-
1542	Plagioclase	3	2707	51	-	-	-	-
1638	Plagioclase	3	3636	95.4	-	-	-	-
1638	Plagioclase	2	3233	135	-	-	-	-
1638	Plagioclase	1	3228	144	-	-	-	-
1654	Plagioclase	3	727	49.5	-	-	-	-

Sample #	*Mineral*	*Min #*	K	K ±	Th	Th ±	U	U ±
1654	Plagioclase	1	488	46.1	-	-	-	-
1654	Plagioclase	2	557	27.3	-	-	-	-
1654	Plagioclase	4	466	34.1	-	-	-	-
DDM-20	Plagioclase	2	2413	301	-	-	-	-
DDM-20	Plagioclase	3	2724	43	-	-	-	-
DDM-20	Plagioclase	1	3015	74.2	-	-	-	-
DDM-303	Plagioclase	1	1909	474	-	-	-	-
DDM-303	Plagioclase	3	1591	195	-	-	-	-
DDM-303	Plagioclase	2	-	-	-	-	-	-
MX-0011	Plagioclase	3	2889	488	-	-	-	-
MX-0011	Plagioclase	1	2689	259	-	-	-	-
MX-0011	Plagioclase	2	2871	153	-	-	-	-
MX-0111	Plagioclase	1	2000	140	-	-	-	-
MX-0111	Plagioclase	2	2349	190	-	-	-	-
MX-0125	Plagioclase	3	2302	140.7	-	-	-	-
MX-0125	Plagioclase	2	3823	2516	-	-	-	-
1525	Rutile	1	-	-	0.12	0.014	0.14	0.013
MX-0011	Rutile	2	-	-	0.083	0.0045	0.7	0.024
MX-0154	Rutile	1	-	-	0.33	0.028	0.75	0.025
DDM-20	Rutile	2	-	-	0.0039	0.0055	1.4	0.014
1030	Rutile	2	-	-	<d.l.	0.000000009	1.5	0.017
1030	Rutile	1	-	-	<d.l.	0.00018	1.7	0.022
1030	Rutile	1	-	-	0.0069	0.0016	1.7	0.027
MX-0011	Rutile	1	-	-	0.038	0.0049	2.1	0.022
MX-0011	Rutile	1	-	-	0.054	0.003	2.3	0.029
1638	Rutile	1	-	-	0.008	0.0014	2.7	0.015
1638	Rutile	2	-	-	0.053	0.0062	4	0.03
1554	Rutile	3	-	-	<d.l.	0.00015	4.5	0.043
1554	Rutile	1	-	-	<d.l.	0.44	7.4	0.63
1554	Rutile	1	-	-	<d.l.	0.0000014	9.5	0.096
1542	Rutile	1	-	-	0.017	0.006	18	0.17
1542	Rutile	2	-	-	0.0088	0.0021	18	0.35

Sample #	*Mineral*	*Min #*	K	K ±	Th	Th ±	U	U ±
1542	Rutile	2	-	-	<d.l.	0.00026	19	0.13
1542	Rutile	3	-	-	0.087	0.014	20	0.21
1542	Rutile	1	-	-	0.36	0.041	21	0.31
DDM-20	Rutile	1	-	-	<d.l.	0.00012	24	0.14
1554	Rutile	2	-	-	0.001	0.0003	24	0.29
1554	Rutile	2	-	-	0.019	0.0027	25	0.32
DDM-303	Rutile	2	-	-	1.6	0.076	32	0.069
DDM-303	Rutile	1	-	-	0.0019	0.00088	33	0.082
DDM-303	Rutile	3	-	-	0.34	0.053	35	0.085
DDM-303	Rutile	4	-	-	8.1	0.62	39	0.11
1638	Scapolite	0	-	-	1.1	0.0082	0.79	0.019
1638	Scapolite	1	1500	926	-	-	-	-
MX-0011	Titanite	1	-	-	1.1	0.088	0.32	0.11
MX-0011	Titanite	1	-	-	1.7	0.13	0.39	0.11
MX-0154	Titanite	2	-	-	7.4	0.071	1.8	0.039
MX-0154	Titanite	1	-	-	9.5	0.083	2.5	0.021
MX-0154	Titanite	1	-	-	7.6	0.059	2.7	0.034
MX-0011	Titanite	2	-	-	4	0.1	12	0.23
MX-0011	Titanite	2	-	-	23	2.5	16	0.65
MX-0154	Titanite	1	6.6	1.5	-	-	-	-
MX-0154	Titanite	1	30	12	-	-	-	-
MX-0154	Titanite	2	7.4	1.5	-	-	-	-
MX-0154	Titanite	2	18	4	-	-	-	-
DDM-20	Zircon	2	-	-	15	0.52	11	0.1
DDM-20	Zircon	2	-	-	21	1.1	15	0.82
1140	Zircon	3	-	-	15	0.59	41	0.75
DDM-303	Zircon	2	-	-	62	5.6	54	2
DDM-303	Zircon	1	-	-	1.8	0.13	57	1.2
1214	Zircon	1	-	-	120	33	150	49
DDM-20	Zircon	1	-	-	51	0.95	60	0.99
1554	Zircon	1	-	-	200	1.9	220	2.4
1554	Zircon	2	-	-	200	1.4	220	1.5

Sample #	*Mineral*	*Min #*	K	K ±	Th	Th ±	U	U ±
1214	Zircon	1	-	-	200	63	230	100
1554	Zircon	3	-	-	91	27	240	7.5
1140	Zircon	1	-	-	50	4.4	360	45
MX-0125	Zircon	1	-	-	260	2.5	400	2.4